

ISSN 0377-9416



www.pmai.in

TRANSACTIONS OF POWDER METALLURGY ASSOCIATION OF INDIA

Vol. 45 No.2, December 2019

Chief Editor - P. Ramakrishnan

ISSN 0377-9416



www.pmai.in

**TRANSACTIONS OF
POWDER METALLURGY
ASSOCIATION OF INDIA**

Vol. 45 No.2, December 2019

Chief Editor - P. Ramakrishnan



Powder Metallurgy Association of India

Office Bearers

President

Shri N. Gopinath

Vice President

Shri Deepak Grover
Shri Narendra Dhokey
Shri Rajendra Sethiya

General Secretary

Dr. Deep Prakash

Hon. Treasurer

Dr. Murli Gopal Krishnamoorty

Joint Secretary

Shri Aniket Gore
Shri Rajat Varshney

Price Rs. 500/-



Chief Editor

Prof. Ramakrishnan P.

Editorial Advisory Board

Dr. Ashok S.

Mr. Chandrachud N.L.

Dr. Rama Mohan T. R.

Editorial Board

Dr. Appa Rao G.

Dr. Bhargava Parag

Dr. Dabhade Vikram

Dr. Deep Prakash

Dr. Dhokey N.B.

Dr. Kumar Y.V.S.

Dr. Malobika Karanjai

Dr. Murli Gopal K.

Dr. Panigrahi B.B.

Dr. Sastry I.S.R.

Dr. Tarasankar Mahata

Published by :

Powder Metallurgy Association of India (PMAI)

102, Anandi, 1st Floor,
M.B. Raut Road, Shivaji Park,
Dadar, Mumbai - 400028, India

Tel: +91 9820951180
+91 9821111677

E-mail: info@pmal.in

Neither the Powder Metallurgy Association of India nor the editor assumes responsibility of opinions expressed by the authors of the papers published in this transaction.

Editorial



Trans. PMAI. Vol. 45 (2) 2019 features selected papers from the 5th Intl. Conference on Powder Metallurgy in Asia & Exhibition 2019, along with 45th Annual Technical Meeting of PMAI held at Hotel JW Marriot Pune. The publication of this Vol. (2) 2019 is also interrupted by the COVID-19 pandemic.

The effect of planetary milling on WC-6wt%Co powder on the sintered grain size, microstructure and mechanical properties of hard metal is investigated in the first paper. Purity prediction model has been used to predict the final purity of the output powder with specific experimental conditions of time, oxygen blowing, temperature and depth of mill scale in the next article.

The effect of process variables on porosity and structure properties of premixed and prediffused sintered steels are discussed in the next paper. This is followed by an article on the design of new bonds with minimum cobalt for the development of diamond wire ropes processed by cold pressing and sintering. Aluminium matrix Carbon fiber reinforced composites have been prepared by different methods and their properties have been covered in the next article. This is followed by a paper dealing with the friction properties of sintered Al-Bronze containing dispersed sulphides.

Fabrication of porous Ti-6Al-4V hydroxyapatite through powder injection molding with space holders is dealt with in this paper. Next paper deals with the processing of complex porous irregular Ti-6Al-4V alloy via selective laser melting. The method can print the alloy very close to the initial model and the complicated porous and cell walls can be reproduced. Development of dense MoSi₂ coating of Niobium alloy C-103 for high temperature oxidation protection is discussed in the next article. Investigation of Tin addition on the forming behavior of Al7SiMg foams produced by powder route is covered in the paper. This is followed by a paper on the design, fabrication and application of inhouse on line deburring machine which has resulted in saving cost and increasing productivity.

Machinability of as-sintered steels manufactured from different commercial low-alloyed iron powder grades and machining additives have been evaluated. The influence of powder grades, machining additives, cutting parameters and tool materials in both drilling and turning are discussed in this paper. Next article is dealing with the reconstruction of the alveolar bone using bone augmentation with selective laser melting of Titanium mesh sheet. Concluding paper is on anisotropic hard ferrite magnet of c-type which is widely used in industrial motors because of its low cost, high safety and thermal stability. But there is a fatal effect on the performance if the magnet is demagnetized. The study of demagnetization effect of c-type anisotropic hard ferrite deals with the key factors to prevent from demagnetization using finite element analysis.

P. Ramakrishnan

**TRANSACTIONS OF
POWDER METALLURGY ASSOCIATION OF INDIA**

Vol. 45 No.2, December 2019

CONTENTS

1 Effect of Planetary Milling on WC Powder Characteristics and Sintered Properties of WC-Co Hardmetal	1-7
<i>Prabin A, Vaishali Jagannath, Ramesh S Rao, Vallish Karthik, Shivaram G</i>	
<hr/>	
2 Modelling of Oxidation Phenomenon of Mill Scale and Analysis of Influencing Parameters	8-17
<i>R. Sabban, C. Tadwalkar, P. C. Jikar, N. B. Dhokey</i>	
<hr/>	
3 Effect of Process Variables on Porosity and Structure Properties of PM Sintered Steels	18-22
<i>Sardey Rigved Pravin, Jing Yang, Jose Antonio Calero, Narendra Babanrao Dhokey</i>	
<hr/>	
4 Design of New Bonds with Minimum Cobalt for the Development of Diamond Wire Ropes	23-28
<i>Rajkumar Yembadi, Ravi Bollina, Ram Kollareddy, Bharat B. Panigrahi</i>	
<hr/>	
5 Manufacturing and Characterization of Aluminium Metal Matrix Composite	29-38
<i>Prof. Madhuri Deshpande, Prof. (Dr.) S.T. Vagge</i>	
<hr/>	
6 Friction Properties of Sintered Al Bronze Containing Dispersed Sulfides	39-50
<i>Tomohiro Sato, Akihiro Jingū, Ken-Ichi Saitoh, Masanori Takuma, Yoshimasa Takahashi</i>	
<hr/>	
7 Fabrication of a Porous Titanium / Hydroxyapatite Metal-Ceramic Composites via Powder Injection Molding with Space Holder Method	51-53
<i>Mohd Yusuf Zakaria, Abu Bakar Sulong, Norhamidi Muhamad, Muhammad Hussain Ismail and Mohd Ikram Ramli</i>	
<hr/>	
8 Production of Irregular Porous Ti-6Al-4V via SLM	54-58
<i>Ahmad Moloodi, Mona Abedinpour, Abolfazl Faramarzian, Ali Haerian</i>	
<hr/>	
9. Formation of Dense MoSi₂ Coating on Niobium Alloy C-103 for Oxidation Protection	59-61
<i>R.V. Krishnarao and G. Madhusudhan Reddy</i>	

10	Investigation on the Effect of Tin Addition on Foaming Behaviour of Al7SiMg Produced by Powder Route	62-69
	<i>Manas Hardikar, R.S.S Srivaishnav, Aniket Sakalley, and Sasikumar.S</i>	
<hr/>	<hr/>	<hr/>
11	Design, Fabrication and Application of In-House, On-Line Green-Deburring Machine	70-77
	<i>Jash Vora, Harish Chaudhari</i>	
<hr/>	<hr/>	<hr/>
12	Machinability of Low-alloyed PM Steels	78-79
	<i>Walter Xu, Ulf Engström, Marcus Persson</i>	
<hr/>	<hr/>	<hr/>
13	Reconstruction of the Alveolar Bone Using Bone Augmentation with Selective Laser Melting Titanium Mesh Sheet	80-83
	<i>Hiroyuki Nakano, Ayano Ogura and Takaaki Ueno</i>	
<hr/>	<hr/>	<hr/>
14	The Study of Demagnetization Effect on C-Type Anisotropic Hard Ferrite Magnet Simulation	84-87
	<i>Chih-Liang Chien, C.S. Liu, Kun-Keng Liu, Chi-Ping Lee and Chun-Chung Shao</i>	

EFFECT OF PLANETARY MILLING ON WC POWDER CHARACTERISTICS AND SINTERED PROPERTIES OF WC-Co HARDMETAL

Prabin A, Vaishali Jagannath, Ramesh S Rao, Vallish Karthik, Shivaram G, Sudarshana Shetty

Kennametal India Limited, Bangalore, India.

Abstract: Cemented Carbide tools are widely used for applications like metal cutting inserts, drills, end mills, wire drawing dies, forging dies, mining buttons etc. The primary reason for the usage of cemented carbides is their very high hardness, wear resistance, relatively good toughness and high resistance to corrosion. Powder metallurgy process has been adapted for processing tungsten carbide (WC) and cobalt (Co) metal matrix composites in an economically feasible route and in mass production. This includes powder production, compaction and liquid phase sintering [1]. The key factor that influences the properties of powder metallurgy products is the particle size of starting WC powder and it's grain size after sintering [2]. This study elucidates the effect of starting powder particle size on sintered grain size, microstructural characteristics and mechanical properties of WC-Co composites. This study presents the results of experimental investigations on mechanical and metallurgical properties of WC-6 weight % Co with different particle size of WC powder. For this study planetary ball milling was used for effective particle size reduction and the properties of both milled and unmilled powders were compared. In planetary ball milling high energy transfer takes place by the action of two centrifugal force acting on the carbide milling balls in opposite direction at the same time resulting in frictional and impact forces. This causes the transfer of high dynamic energy from impact and shear of balls and WC powder [3]. The milled and un-milled WC powders were graded by planetary ball mill and vacuum drying, compaction and sintering. The morphology, average particle size and it's distribution and phase of the powders were compared before and after milling of WC powders. Also, the sintered properties of these powders were compared, and correlation developed with the powder process condition.

Introduction

WC-Co based hardmetal or cemented tungsten carbides has been well known for its exceptional hardness, wear resistance, corrosion resistance and chemical stability at higher temperatures. Matrices of ductile metals, such as cobalt, greatly improve its toughness so that the brittle fracture can be avoided [3]. Cemented tungsten carbides are commercially one of the oldest and most successful powder metallurgy products. These hardmetals are fundamentally aggregates of tungsten carbide particles bonded with a binder either Cobalt or Nickel mainly via liquid-phase sintering [1]. The properties of this hardmetal depends on the composition of the

binder, characteristics of the starting powders and manufacturing process. Therefore, the size, shape and distribution of the particles, the homogeneity of microstructure and porosity affect the mechanical properties of the material [4,5]. The powder properties, such as particle size distribution, morphology and final stoichiometry depends upon the milling conditions [6,7]. This study aims to investigate the influence of planetary ball milling (PBM) on five different WC particle size and the sintered properties of these WC powders with 6 weight% Cobalt binder based hardmetal. This study is done in two phases with first phase to identify the effect of Planetary balling time on WC powder characteristics. In the second phase , the

EFFECT OF PLANETARY MILLING ON WC POWDER CHARACTERISTICS AND SINTERED PROPERTIES OF WC-Co HARDMETAL

planetary ball milled WC powder with 6 weight % cobalt binder is studies to corelate with the sintered properties.

Experimental Procedure

The experimental procedure to produce the WC-6 weight% Co hardmetal is based on conventional powder metallurgy techniques associated with the technique of milling.

The materials used were WC powders of 5 different particle sizes and Cobalt of 99.98% purity. The planetary milling (PBM) was used for the size reduction of five different sized WC powders and to study the effect of Planetary milling of WC powders.

Table-1 below shows the list of WC powders with average particle size selected for Phase-I study.

The above five WC powders were taken for the phase-I study to fix the planetary ball milling time. All other parameters like RPM, Milling Ball ratio, Milling Ball diameter and Milling Media was fixed. They are milled in planetary ball mill at 125 RPM , 1:5 powder to ball ratio, 6mm diameter tungsten carbide milling media and in Iso-Propyl Alcohol medium for 2,4,6 and 8 hours. The average particle size, particle size distribution, particle phase and oxygen pick-up were studied for these powders.

Table-1. WC powders particle size

Sl. No	Material	Grade	FSSS, Average Particle Size in μm	Particle size ISO classification
1	WC	A1	1.5	Fine
2	WC	A2	4.2	Coarse
3	WC	A3	6.6	Extra Coarse
4	WC	A4	10	Extra Coarse
5	WC	A5	2.0	Medium

In phase-II experiments, 6 hours of milling time was fixed with the same planetary ball milling conditions for the powders mentioned in Table-1. These WC powders were graded with 6 weight %Co and also, un-milled WC powders were also graded for comparative analysis to study the effect of initial planetary ball milling. The graded powder processing conditions are shown in Table-2.

Table-2. Grade details made of different WC powders

Experiment Number	WC type	Grade mixing Condition
1	A1 (6hrs milled in PBM)	Planetary Ball milled with 1:1 ball to powder ratio 9mm diameter carbide milling media for one hour with Iso-Propyl Alcohol at 60 RPM
2	A2 (6hrs milled in PBM)	
3	A3 (6hrs milled in PBM)	
4	A4 (6hrs milled in PBM)	
5	A5 (6hrs milled in PBM)	
6	A1 (Un-milled)	
7	A2 (Un-milled)	
8	A3 (Un-milled)	
9	A4 (Un-milled)	
10	A5 (Un-milled)	

The ten grades shown in Table-2 are vacuum dried, compacted and sinter hipped at 1480°C. These ten grades were compared for Magnetic Saturation, Coercive Force, Vickers Hardness and Microstructure.

Results and Discussion

Phase-I: Effect of Planetary Ball milling time on WC powder Characteristics.

The average particle size of five WC powders versus the milling time is shown in Figure-1.

EFFECT OF PLANETARY MILLING ON WC POWDER CHARACTERISTICS AND SINTERED PROPERTIES OF WC-Co HARDMETAL

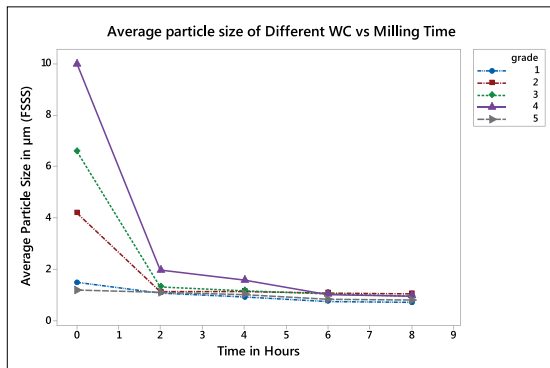


Figure-1: Average particle size vs Milling time

It is evident from Figure-1 that the WC with higher particle size reduces rapidly when compared to WC with lower particle size. For this fixed parameter of planetary ball mill, the reduction in particle size for all type of WC powders is negligible after 6 hours of milling. This indicates the effect of milling using planetary ball mill is saturated after 6 hours.

However, there is a significant increase in the oxygen pick-up with milling time and it is higher for the finer WC powders as illustrated in Figure-2. The oxygen pick-up is due to the surface activation of powders during planetary milling process. [11]

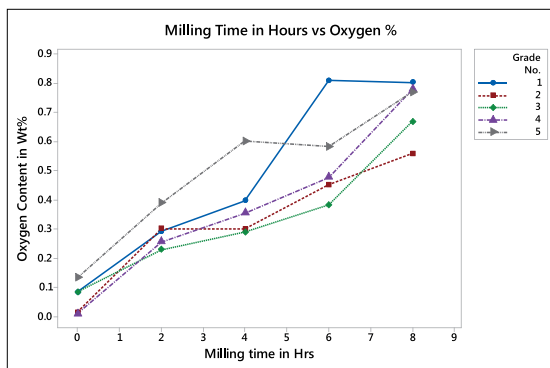


Figure-2: Planetary Milling time vs Oxygen content

The effect of milling time on the particle size distribution measured using Laser scattering technique is shown in the Table-3.

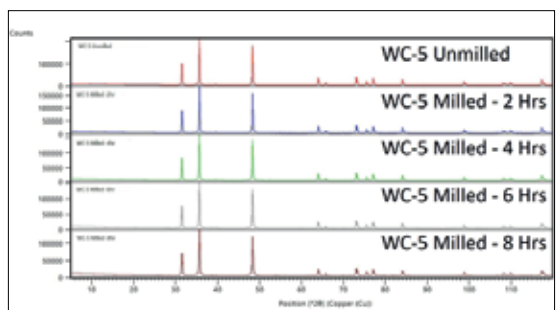
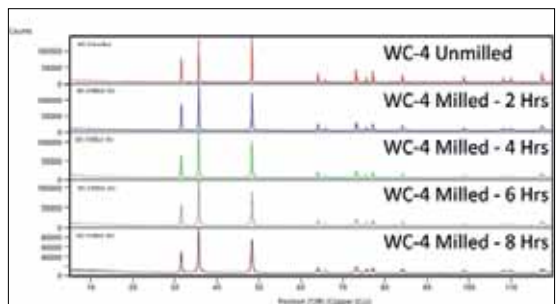
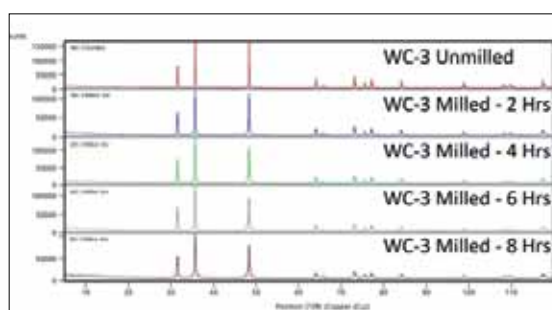
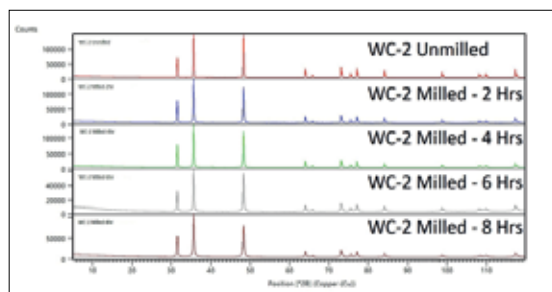
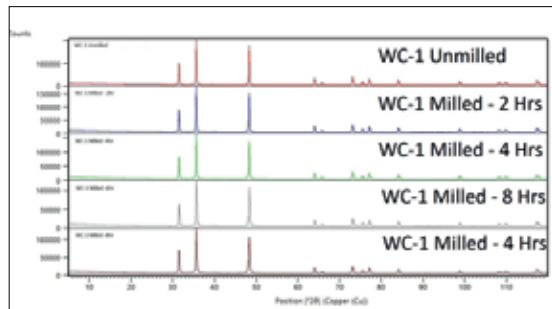
Table-3. Particle size distribution data for different WC with increasing milling time

Grade	Milling Time in Hours	D10 in μm	D50 in μm	D90 in μm	Span (D90-D10)/D50
A1	0	1.31	3.31	7.98	2.02
	2	0.61	1.70	3.94	1.96
	4	0.42	1.32	3.09	2.03
	6	0.44	1.15	2.54	1.83
	8	0.24	0.86	1.97	2.03
A2	0	3.06	6.75	13.18	1.50
	2	0.50	1.69	3.99	2.07
	4	0.54	1.79	4.10	2.00
	6	0.38	1.38	3.18	2.04
	8	0.31	1.23	2.91	2.11
A3	0	4.55	10.70	20.66	1.51
	2	0.71	2.19	5.21	2.05
	4	0.48	1.84	4.29	2.07
	6	0.36	1.42	3.37	2.12
	8	0.30	1.16	2.78	2.14
A4	0	7.15	13.68	23.71	1.21
	2	0.95	3.30	7.47	1.97
	4	0.58	2.18	5.17	2.11
	6	0.38	1.55	3.86	2.24
	8	0.31	1.26	3.17	2.27
A5	0	0.93	2.29	6.69	2.52
	2	0.54	1.50	3.42	1.92
	4	0.41	1.22	2.77	1.93
	6	0.30	1.04	2.41	2.04

There is a shift in the particle size distribution towards finer size with respect to planetary ball milling time and the difference in distribution is insignificant after 6 hours of milling. However, the Span value is within 2 ± 0.2 units after planetary milling irrespective of the initial particle size.

EFFECT OF PLANETARY MILLING ON WC POWDER CHARACTERISTICS AND SINTERED PROPERTIES OF WC-Co HARDMETAL

The X-Ray Diffractogram of WC Powders with different Planetary ball milling time is given in Figure-3.



X-Ray diffractogram analysis shows there is no significant difference in tungsten carbide hexagonal close packing [7] crystal structure after planetary ball milling and there are no secondary phases other than tungsten carbide present the powder samples.

Phase-II: Effect of Planetary Ball milled (6hrs) WC powders on Sintered properties of WC-Co hardmetal.

The sintered properties like Magnetic Saturation, Coercive force and Vickers hardness comparison of milled and un-milled WC powders are shown in Figure-4, Figure-5 and Figure-6 respectively.

EFFECT OF PLANETARY MILLING ON WC POWDER CHARACTERISTICS AND SINTERED PROPERTIES OF WC-Co HARDMETAL

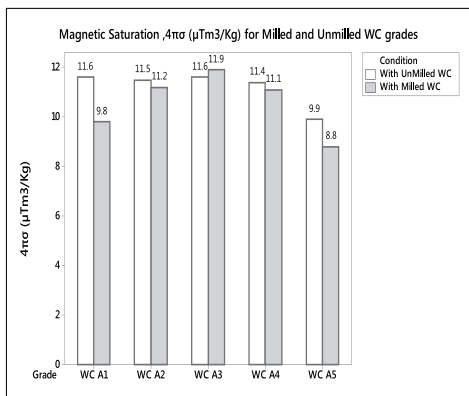


Figure-4. Magnetic Saturation of milled WC and un-milled WC powder grades

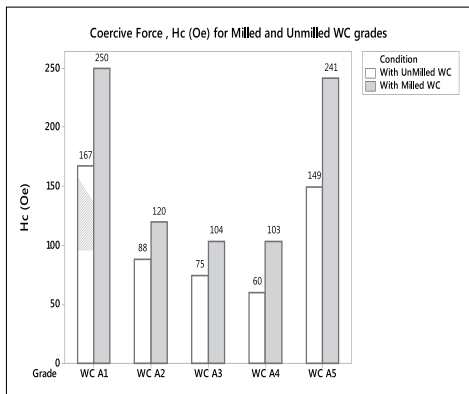


Figure-5. Coercive force comparison of milled WC and un-milled WC powder grades

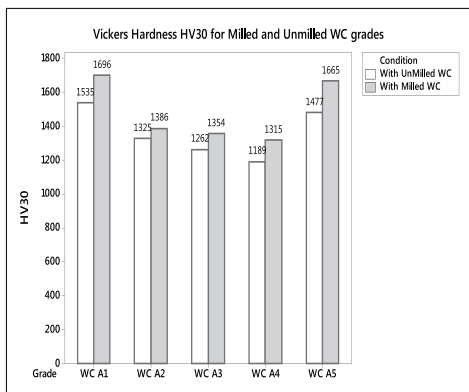


Figure-6. Hardness comparison of milled and un-milled WC powder grades

It's clearly observed from Figure-4 that, the planetary ball milled finer WC powder has lower Magnetic Saturation value due to oxygen pick-up resulting in carbon loss during sintering. As coercive force is inversely proportional to Magnetic saturation, the higher coercive force is observed for finer WC powders with lower Magnetic Saturation as in Figure-4 and Figure-5. The Vickers hardness follows the pattern of coercive force as shown in Figure-6.

Microstructure comparison of Milled and Unmilled WC powders in 1000X magnification are shown in Figure-7.

As shown in Figure-7a-d, there is a significant difference in the sintered microstructure of unmilled WC powder of fine and medium particle size. However, the Planetary milled WC powder unable to differentiate sintered microstructure for fine and medium WC powders. The planetary mill is effective in achieving the finer sintered microstructure even without any grain growth inhibitor unlike the experiment grade-1 which has Vanadium Carbide (VC) as grain growth inhibitors.

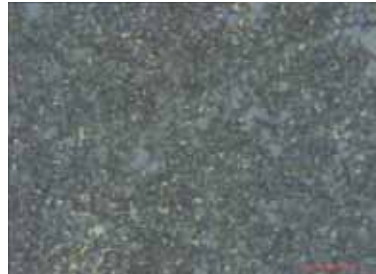
As shown in Figure-7e-j, there is a significant difference in the sintered microstructure of unmilled WC powder of Coarse and extra-coarse particle size.

It is unable to differentiate sintered microstructure of coarse and extra-coarse grain size after planetary ball milling. This is also illustrated as the average sintered tungsten carbide grain size in Table-5.

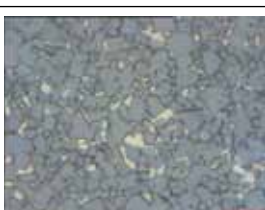
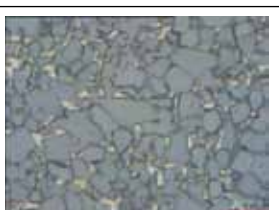
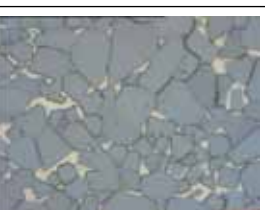
Table-5 Average grain size comparison of milled and un-milled sintered WC

Experiment no	With Milled WC		With Un-milled WC	
	Average sintered WC grain Size in μm	Experi-ment no	Average sintered WC grain Size in μm	Experi-ment no
1	1.50	6	1.75	
2	2.75	7	4.50	
3	3.00	8	6.50	
4	3.25	9	10.00	
5	2.00	10	2.35	

EFFECT OF PLANETARY MILLING ON WC POWDER CHARACTERISTICS AND SINTERED PROPERTIES OF WC-Co HARDMETAL

<i>Initial WC Particle size = Fine</i>	<i>Initial WC Particle size = Medium</i>
	
<i>Figure-7a. Microstructure of Expt.1 with milled WC</i>	<i>Figure-7b. Microstructure of Expt.6 with un-milled WC</i>

<i>Initial WC Particle size = Coarse</i>	<i>Initial WC Particle size = Extra-Coarse</i>	<i>Initial WC Particle size = Extra-Coarse</i>
		
<i>Figure-7e. Microstructure of Expt.2 with milled WC</i>	<i>Figure-7f. Microstructure of Expt.3 with milled WC</i>	<i>Figure-7g. Microstructure of Expt.4 with milled WC</i>

<i>Initial WC Particle size = Coarse</i>	<i>Initial WC Particle size = Extra-Coarse</i>	<i>Initial WC Particle size = Extra-Coarse</i>
		
<i>Figure-7h. Microstructure of Expt.7 with un-milled WC</i>	<i>Figure-7i. Microstructure of Expt.8 with un-milled WC</i>	<i>Figure-7j. Microstructure of Expt.9 with un-milled WC</i>

EFFECT OF PLANETARY MILLING ON WC POWDER CHARACTERISTICS AND SINTERED PROPERTIES OF WC-Co HARDMETAL

Conclusion

The following inferences were made from this study on.

The average particle size of the WC powders decreases with milling time and the reduction saturates after 6hrs. However, there is an increase in oxygen pick-up even for the powders milled in inert solvent. The oxygen pick-up is significant for finer WC powders resulting in lower magnetic saturation after sintering.

The reduction in particle size with planetary ball milling resulted in uniform and relatively finer microstructure after liquid-phase sintering. This is also validated by coercive force and hardness measurement.

Interestingly, there is no significant difference in sintered microstructure for planetary ball milled coarse and extra-coarse WC powders when compared to un-milled WC powders. Similar trend is observed for fine and medium particle sized WC powders.

From this study, we can also infer that there is no significant grain coarsening of planetary ball milled powders during sintering. Also, we could achieve fine grain microstructure without use of any grain growth inhibitors which has negative influence on the toughness of hardmetal grade.

Acknowledgments

The authors thank Mr. Nadir Hussain and Mr. Abhishek Kumar Post-graduate students from NITK Surathkal for their support for conducting the experiments.

References

1. G. S. Upadhyaya, *Powder Metallurgy Technology*, Cambridge International Science Publishing, ISBN 1 898326 40 1, First published August 2002.
2. Kaushal Kishore Singh and Sudipto Bhattacharjee, *Study On The Effect Of High Energy Ball Milling (A Nano Material Process) On The Microstructure And Mechanical Properties Of A (Al-Si-Fe-Cu) Alloy*, Thesis, Department of Metallurgical and Materials Engineering, National Institute of Technology, Rourkela, 2007.
3. F.L. Zhang, M. Zhu and C.Y. Wang, *Parameters optimization in the planetary ball milling of nanostructured tungsten carbide/cobalt powder*, *International Journal of Refractory Metals & Hard Materials* Vol. 26, 2008, pp. 329–333.
4. Erik Lassner and Wolf Dieter Schubert. *Tungsten properties, Chemistry, Technology of the Element alloys and chemical compounds* 1999 ISBN 0-306-45053-4 .
5. *Planetary Ball Mills PM100 catalogue*, Retsch solutions in milling and sieving, pp 18-19.
6. *Micro crystalline Tungsten Carbide*, Kennametal Inc, B-15-04518EN, 2015.
7. *Tungsten carbide powders*, Kennametal Inc, B-15-20150720TCP, 2015.
8. Siphilisiwe Ndlovu, "The Wear Properties of Tungsten Carbide-Cobalt Hardmetals from the Nano scale up to the Macroscopic Scale", P.hD. thesis, 2009.,
9. A.S. Kurlov, A., Leenaers, S. van den Berghe, M. Scibetta, AEL NICL and A.A. Rempel "Microstructure of nanocrystalline wc powders and WC-Co hard alloys", Institute of Solid State Chemistry, Ural Division of the RAS, 620990 Ekaterinburg, Russia, 2010, pp. 165-172.
10. Renee Joost, Jüri Pirso, Mart Viljus, Sergei Letunovič and Kristjan Juhani, "Recycling of WC-Co hardmetals by oxidation and carbothermal reduction in combination with reactive sintering", In Proc. Euro PM2004. Vienna, 2004, vol. 3, pp. 19-24.
11. Kaushal Kishore Singh, "Study on the effect of high energy ball milling (a nanomaterial process) on the microstructure and mechanical properties of an alloy", ADME, Vol.2. 2013, pp. 6-17.
12. E. Gaffet, G. Le Caér, "Mechanical Processing for Nano materials", ISBN: 1-58883-001-2, volume X, 2004, pp.1-39.
13. H.Q. Sun, Rudy Irwan, Han Huang, Gwidon W. Stachowiak, "Effect of microstructure on mechanical properties and wear characteristics of cemented Tungsten carbides", Advanced material Research, Vols. 76-78, 2009, pp. 609-612.
14. J.B. Cheng, S.Q. Pang, X.B. Wang, C.G. Lin "The effect of grain size and cobalt content on the wear of ultrafine cemented carbide tools", Advanced Materials Research, Vols. 875-877, 2014, pp. 1344-1351.

MODELLING OF OXIDATION PHENOMENON OF MILL SCALE AND ANALYSIS OF INFLUENCING PARAMETERS

R. Sabban, C. Tadwalkar, P. C. Jikar , N. B. Dhokey

Department of Metallurgy and Materials Science, College of Engineering, Pune, India

Abstract: Steel rolling mill waste product, can be converted into industrially attractive Fe_2O_3 powders. The purity of the Fe_2O_3 powder is a selection criterion for various applications such as soft and hard ferrite, surface temperature measurement, paint, ceramic color, cancer treatment and thermite welding. This process can be simulated with the help of mathematical modelling and using Buckingham Pi Theorem by considering the effect of different parameters like flow rate, density, viscosity and duration of oxygen blowing, initial composition of mill scale, length and depth of mill scale bed, geometrical parameters of furnace like length of diameter. In the present study, Purity Prediction Model (PPM) has been developed to predict the final purity of the output powder with specific set of conditions and the results of the same are verified with the help of experimentation in which temperature, time and the depth of mill scale bed was varied. It is concluded that 3D surface response and sensitivity analysis is use full in deciding influencing parameters that affect degree of oxidation.

Introduction

Mill scale product in steel mill is a combination of different oxides like Hematite (Fe_2O_3), Magnetite (Fe_3O_4), Wustite (FeO) etc. [6,19,21]. Conversion of this multi oxide mill scale into single highest oxide (Fe_2O_3) is the best suited route for turning out to be an industrially attractive process for soft and hard ferrites, surface temperature measurement, paint, ceramic colours, Cancer treatment, and thermite welding, tiles, nanotubes in gas sensor, Lithium ion battery resistor for carbon monoxide [2,6,7,12,14,20]. This can be economically carried out with increasing the kinetics of the reaction which in turn depends upon several experimental factors and nature of initial mill scale.^[14] The whole oxidation process can be mathematically modelled considering the effect of different parameters of oxygen and mill scale using Dimensionless Analysis Approach i.e. Buckingham Pi theorem [6,8,13,23]. Several previous studies have shown that temperature, density and viscosity of oxygen during oxygen blowing significantly affect the purity of final oxide in the powder [15]. The purification parameter 'P', which is the best indication of weight % of Fe_2O_3 in the output powder and it considers the effect of weight of initial mill scale experimented is

expressed on the basis of a mathematical model for predicting the output by assuming 13 input parameters. Subsequently, the supporting experimentation is also carried out. The affecting parameters on the degree of oxidation that are considered in the dimensionless analysis modelling are listed in Figure 1.

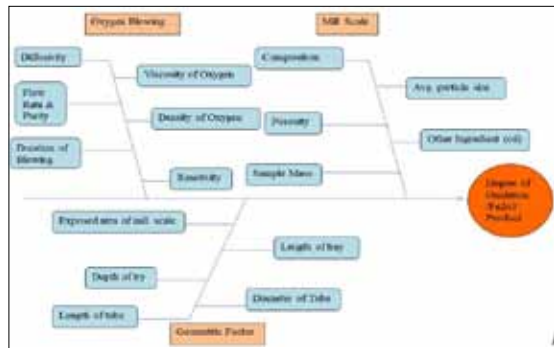


Figure 1. Ishikawa diagram indicating various parameters affecting the purity of Fe_2O_3

Experimental Procedure and Method

In the present study oxidation of milled mill scale is carried out in $MoSi_2$ furnace as shown in Fig.2. During oxidation, 3 parameters viz. temperature of furnace, time of oxygen blowing

MODELLING OF OXIDATION PHENOMENON OF MILL SCALE AND ANALYSIS OF INFLUENCING PARAMETERS

and depth of static mill scale powder bed were varied individually, as shown in Table 1 to study their effect by keeping other parameters constant. These constant parameters include flow rate of oxygen (500 ml/min), geometric factors like diameter of tube 5 cm, length of the tube 80 cm, length of the mill scale tray 10 cm, apparent density of powder particles as 1.578 g/cc and average particle size as 5.23 μm .

Table 1: Process conditions for oxidation of mill scale

Sr. No.	Variables	Temperature (°C)	Time(h)	Depth of powder bed (mm)
1.	Temperature	900, 1000, 1100	3	10
2.	Time	1100	1, 2, 3	10
3.	Depth of mill scale bed	1100	3	10, 12, 14, 16

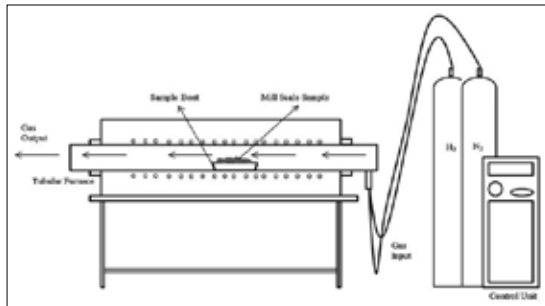


Fig 2. Schematic sketch of MoSi_2 Furnace setup for oxygen blowing of mill scale

Formulation of Dimensionless Purity Prediction Model (DPPM)

A dimensionless analysis approach based on Buckingham Pi theorem used here in which it is assumed that the Fe_2O_3 purity of final oxidised powder is affected by certain set of parameters listed in Table 2.

The relationship between the above mentioned parameters is expressed in Equation (1)

$$P = f(T, \rho, \eta, Q, L, D, d, t, l, \rho_p, C_p, S, W_m) \quad [1]$$

In the dimensionally homogeneous equation involving '13' variables, '4' primary or fundamental dimensions (M, L, t, T) can be

expressed in a single relationship among 13-4=9 independent dimensionless pi terms. The final form of the model is given by Equation (2) and detailed calculations of dimensions are given in Appendix A.

The corresponding Dimensionless Purity Prediction Model (DPPM) equation is

$$\text{Degree of Oxidation (P)} = \Phi.$$

Table 2. Abbreviations of symbols and their dimensional forms

Sr.No.	Physical Quantity	Symbol	Unit	Dimensions
1	Temperature of oxidation	T	K	$[\text{M}^0\text{L}^0\text{T}^0\theta^0]$
2	Density of Oxygen	ρ_g	Kg/m^3	$[\text{M}^0\text{L}^{-3}\text{T}^0\theta^0]$
3	Viscosity of oxygen	η	Kg/ms	$[\text{M}^1\text{L}^{-1}\text{T}^{-1}\theta^0]$
4	Flow rate of oxygen	Q	m^3/s	$[\text{M}^1\text{L}^0\text{T}^{-1}\theta^0]$
5	Length of the tube	L	m	$[\text{M}^0\text{L}^1\text{T}^0\theta^0]$
6	Diameter of the tube	D	m	$[\text{M}^0\text{L}^1\text{T}^0\theta^0]$
7	Depth of the bed of the tray	d	m	$[\text{M}^0\text{L}^1\text{T}^0\theta^0]$
8	Time of oxygen blowing	t	s	$[\text{M}^0\text{L}^0\text{T}^1\theta^0]$
9	Length of the bed	l	m	$[\text{M}^0\text{L}^1\text{T}^0\theta^0]$
10	Apparent density of mill scale	ρ_p	Kg/m^3	$[\text{M}^0\text{L}^{-3}\text{T}^0\theta^0]$
11	Specific heat of reaction	Cp	J/KgK	$[\text{M}^0\text{L}^3\text{T}^{-2}\theta^0]$
12	Specific surface area of powder	S	m^2/kg	$[\text{M}^{-1}\text{L}^2\text{T}^0\theta^0]$
13	Weight of mill scale	Wm	Kg	$[\text{M}^1\text{L}^0\text{T}^0\theta^0]$
14	Degree of oxidation	P	-	-

$$\frac{\eta, L, C_p, S, t, \rho_p, D, T, d}{Q^3, \rho^2, l^3} \boxed{A} \quad (2)$$

$$P = \Phi. (X)^A \quad (3)$$

Taking log of equation (3) on both sides,

$$\log P = \log \Phi + A (\log X)$$

This equation is analogous to the straight line equation,

$$y = c + mx$$

MODELLING OF OXIDATION PHENOMENON OF MILL SCALE AND ANALYSIS OF INFLUENCING PARAMETERS

1. Terminology

Dimensionless purity parameter (P) is the ratio of weight of Fe_2O_3 in the oxidised powder to the weight of initial mill scale taken. Process parameter (X), defined by Equation (4), consists of variables that affect the weight % Fe_2O_3 in the final powder during oxidation of mill scale powder. It is a combined interactive process parameter. The interaction amongst the variables mentioned in X is reflected in terms of exponent A and coefficient Φ which is the intercept on the Y-axis.

$$X = \frac{[\eta, L, C_p, S, t, \rho_p, D, T, d]}{Q^3, \rho^2, l^3} \quad (5)$$

In the Equation (2), Φ and A are the two constants which can be termed as characteristic constants. These constants can be obtained by conducting experiments and solving Equation (2) at constant values of parameters, using Appendix B.

Results and Discussion

1. Degree of oxidation

The chemical analysis results of weight % Fe_2O_3 after the oxidation of mill scale at constant depth of mill scale of 10 mm are listed in Table 3. These results were plotted and analysed to get the surface response which depicts the combined effect of 'T' and 't' on degree of oxidation.

As shown in Figure 3, at 1100°C and with 3 hours of oxygen blowing, the mill scale gets oxidised to 97.5 % Fe_2O_3 .

Table 3. Wet chemical analysis of Fe_2O_3 in the oxidised mill scale

Temperature (°C)	900	1000	1100
Time (hours)			
1	81.38	91.81	93.05
2	81.75	92.14	94.42
3	82.22	94.01	97.50

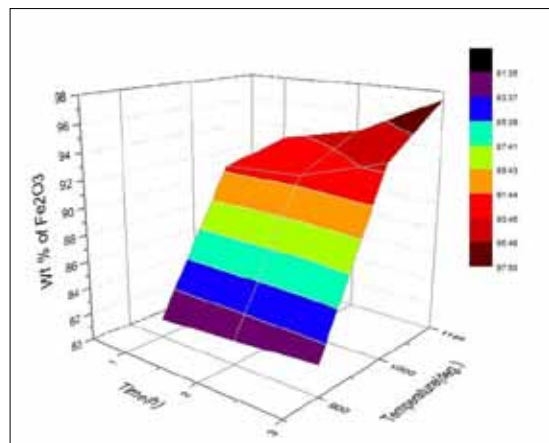


Fig 3. Experimental 3-D Surface map showing the dependence of wt % Fe_2O_3 , as a function of temperature and time.

2. Effect of Variation of Temperature

From equation 4, a graph was plotted as shown in Fig.4. It is showing good regression value and from that graph the values of exponent A and coefficient Φ come out to be $\Phi = 0.3722$ and $A = 0.1033$.

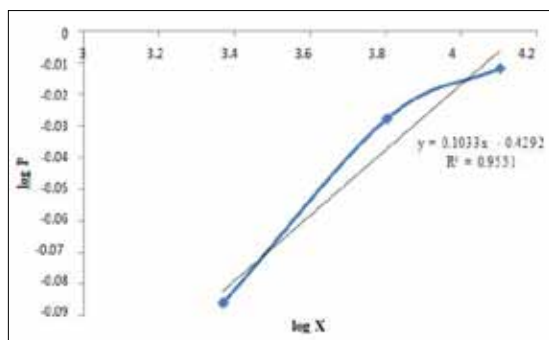


Fig .4 $\log P$ Vs $\log X$ graph ($\Phi = 0.37224$ and $A = 0.1033$)

Table 4. shows how temperature variation affects the value of X and the true % error in prediction of purity value with respect to experimental value. The predicted purity can be calculated from equation (6).

MODELLING OF OXIDATION PHENOMENON OF MILL SCALE AND ANALYSIS OF INFLUENCING PARAMETERS

Figure 5 represents the correlation between experimental and predicted value of purity of Fe_2O_3 graphically. It gives result in close agreement and validates the dimensionless purity prediction model (DPPM).

Table 4. Correlation between experimental and predicted purity value of Fe_2O_3 with varying temperature at fixed time of 3 h and constant mill scale bed of 10 mm.

Expt. No.	Temperature (°C)	log(X)	Predicted Purit y (PB)	Experimental purity (PA)	% True error (PA-PB/PA)*100
1	900	7.76	82.97822	81.75	-1.50240
2	1000	8.76	91.82085	94.01	2.32863
3	1100	9.44	98.83759	97.50	-1.371887

$$P=0.372246(X)^{0.10333} \quad (6)$$

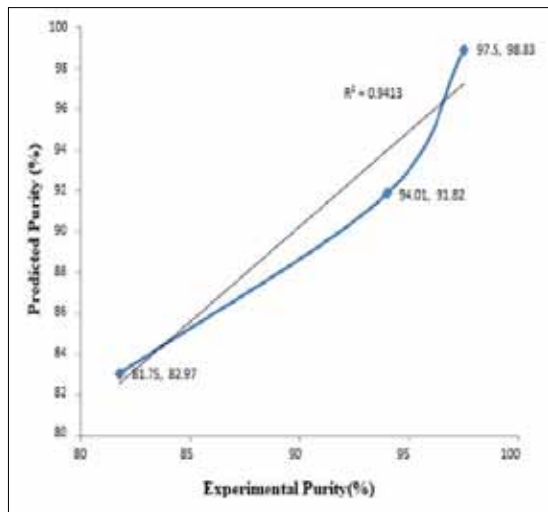


Fig 5. The graph of Experimental vs predicted purity of Fe_2O_3 showing correlation of $R^2 = 0.9413$

3. Effect of Variation of Time

As shown in Figure 6, the graph is plotted as per equation (4) between $\log P$ and $\log X$. It is showing good regression value and from that graph, the values of exponent A and coefficient Φ are found to be $\Phi = 0.6626$ and $A=0.0402$

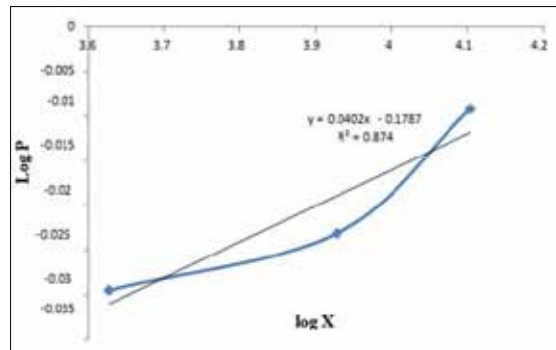


Fig 6. Log P vs log X graph ($\Phi = 0.6627$ and $A=0.0402$)

Table 5 shows how time variation affects the value of X and the true % error in prediction of purity value with respect to experimental value.

Table 5. Correlation between experimental and predicted purity value of Fe_2O_3 with varying time (constant temperature of 1100°C and constant mill scale depth of 10 mm)

Expt. No.	Time h	Log(X)	Predicted Purity (P _B)	Experimental Purity (P _A)	%True error (P _A -P _B /P _A)*100
1	1	8.3508	92.7123	93.05	0.3628
2	2	9.0440	95.3323	94.42	-0.9564
3	3	9.4495	96.8990	97.50	0.6163

Figure 7. represents the correlation between experimental and predicted value of purity of Fe_2O_3 graphically. It gives results in close agreement and validates the dimensionless purity prediction model (DPPM).

$$P=0.66267(X)^{0.0402}$$

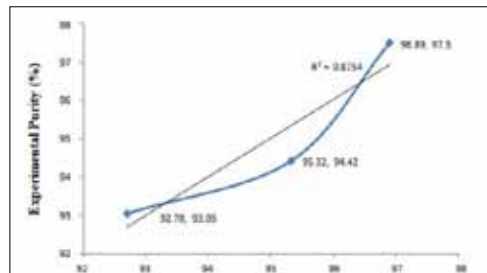


Fig 7. Experimental vs predicted purity of Fe_2O_3 showing correlation of $R^2= 0.8742$

MODELLING OF OXIDATION PHENOMENON OF MILL SCALE AND ANALYSIS OF INFLUENCING PARAMETERS

4. Effect of Variation of depth of mill scale bed

As shown in Figure 8, the graph is plotted as per equation (4) between $\log P$ and $\log X$. It shows good regression value and derived exponents A and coefficient Φ are -0.0907 and 2.2651 respectively.

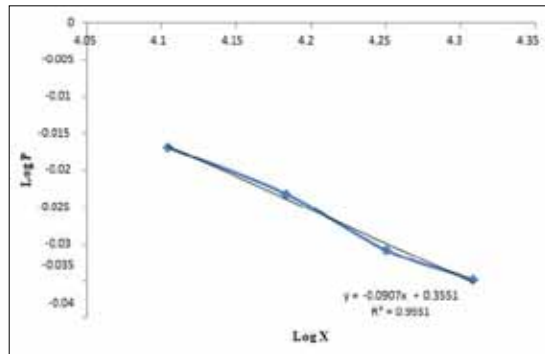


Fig 8. log P vs log X graph ($\Phi = 2.2651$ and $A = -0.0907$)

Table 6 shows how depth of mill scale bed variation affects the value of X and the true % error in prediction of purity value with respect to experimental value.

Table 6 Experimental and predicted purity of Fe_2O_3 with varying depth of mill scale (Constant temperature of $1100^{\circ}C$, Constant time 3 h)

Expt. No.	Time (h)	Log(X)	Predicted Purity (PB)	Experimental Purity (PA)	%True error (PA-PB/PA)*100
1	10	9.4495	96.1231	96.13	0.6833
2	12	9.6318	94.5466	94.73	0.1935
3	14	9.7859	93.2339	93.09	-0.1546
4	16	9.9195	92.1116	92.23	0.1283

Figure 9 represents the correlation between experimental and predicted value of purity of Fe_2O_3 graphically. It gives results in close agreement and validates the dimensionless purity prediction model (DPPM).

$$P=2.2651(X)^{-0.0907}$$

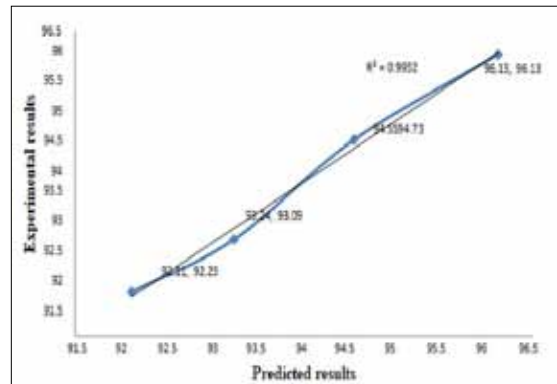


Fig 9. The graph of Experimental vs predicted purity of Fe_2O_3 showing good correlation of $R^2= 0.98975$

Sensitivity Analysis

It is interesting to analyse the influence of operating parameters i.e. Temperature(T), time(t) and depth of mill scale bed(d) on purity of Fe_2O_3 . Mathematically this can be obtained by taking derivative of eq.(1) with respect to T, t and d. and substituting the optimum conditions values of T = $1100^{\circ}C$, t = 3 h, d = 10 mm .Those equations are

$$\frac{dP}{dT} = \phi x A x(X)^{A-1} = 7.432 \times 10^{-5} \quad (2)$$

$$\frac{dP}{dT} = \phi x A x(X)^{A-1} = 3.6052 \times 10^{-6} \quad (3)$$

$$\frac{dP}{dT} = \phi x A x(X)^{A-1} \frac{dP}{dd} = 8.7191 \quad (4)$$

It is observed that that the purity of Fe_2O_3 is strongly sensitive to depth of the mill scale bed(d), moderately on temperature(T) and less sensitive to time of oxygen blowing(t) Table 7.

MODELLING OF OXIDATION PHENOMENON OF MILL SCALE AND ANALYSIS OF INFLUENCING PARAMETERS

Table 7 Sensitivity analysis of the models predicted for Temperature of oxygen blowing (T), time of Oxygen blowing (t) and depth of mill scale bed (d)

Significant Parameter	Equation	Φ	A	Derivative	Remark
T	$P = 0.37224 [X]^{0.103}$	0.3724	0.1033	$\frac{dP}{dT} = -5$	Moderately Sensitive
t	$P = 0.6626 [X]^{0.0402}$	0.6626	0.0402	$\frac{dP}{dt} = 3.6052 \times 10^{-6}$	Less Sensitive
d	$P = 2.2651 [X]^{-0.0987}$	2.2651	-0.0907	$\frac{dP}{dd} = 8.7191$	Highly Sensitive

Conclusions

The Dimensionless Purity Prediction Model (DPPM) has been obtained using Buckingham Pi theorem. The characteristic constants derived from this model can be used to predict purity of Fe_2O_3 relationship with selected parameters that are employed such as Temperature, time, depth of mill scale bed.

The following conclusions can be drawn:

1. DPPM model is put forward between purity of Fe_2O_3 in oxidised powder and thirteen parameters. It gives rise to characteristic constants i.e. pre-exponent and exponent for the given set of conditions employed.
2. The correlation between the experimental and predicted value of purity of Fe_2O_3 is in close agreement with R^2 value ranging from 0.87 to 0.98
3. From the analysis of model, it is found that the predicted purity follows direct relationship with temperature and time and inverse relation with depth of mill scale bed if varied independently.
4. 3-D surface plot comprising of effect of temperature and time is analysed and it is in close agreement with predicted results.
5. Sensitivity analysis depicts that degree of oxidation is strongly sensitive to depth of the mill scale bed, moderately on temperature and less sensitive to time of oxygen blowing.

Appendix A

A.1. Derivation of dimensionless purity prediction model (DPSM)

Total no. of variables n = 13

Total no. fundamental dimensions m=4.(M , L , t, T)

Pi term required to be find out=n - m = 13-4=9

Calculations for Π terms

Finding out the expression of purity of Fe_2O_3

$$f(\Pi_1, \Pi_2, \Pi_3, \Pi_4, \Pi_5, \Pi_6, \Pi_7, \Pi_8, \Pi_9, \Pi_{10}, \Pi_{11}, \Pi_{12}, \Pi_{13}) = 0$$

1) Π_1 term calculations :- (Non-Repeating variable :- Viscosity of oxygen gas η)

Here 1] length of mill scale bed(l),2] Density of oxygen gas (ρ), 3] Flow rate of Oxygen gas(Q) and 4] temperature of the system(T) are 4 repeating variables.

$$\Pi_1 = l^a, \rho^b, Q^d, \eta$$

$$[M^0 L^0 T^0 \theta^0] = [M^0 L^1 T^0 \theta^0]^a [M^1 L^{-3} T^0 \theta^0]^b [M^0 L^3 T^{-1} \theta^0]^c [M^0 L^0 T^{-1} \theta^1]^d [M^1 L^{-1} T^{-1} \theta^0]$$

For M,b+1=0 b=-1,

For L,a-3b+3c-1=0 a+3c+2=0.....(1)

For T,-c-1=0 c=-1 putting in eq(1)

a=1

For $\theta, d=0$

$$\Pi_1 = \frac{l\eta}{\rho Q}$$

2) Π_2 term calculations :- (Non-Repeating variable :- Length of the tube L)

$$\Pi_2 = l^a, \rho^b, Q^d, T^d, L$$

$$[M^0 L^0 T^0 \theta^0] = [M^0 L^1 T^0 \theta^0]^a [M^1 L^{-3} T^0 \theta^0]^b [M^0 L^3 T^{-1} \theta^0]^c [M^0 L^0 T^0 \theta^1]^d [M^0 L^1 T^0 \theta^0]$$

For M,b=0

For L,a-3b+3c+1=0 a+3c =-1.....(2)

MODELLING OF OXIDATION PHENOMENON OF MILL SCALE AND ANALYSIS OF INFLUENCING PARAMETERS

For T,c=0 putting in eq(2)

$$a=-1$$

For θ,d=0

$$\Pi_2 = \frac{L}{1}$$

3) Π_3 term calculations :- (Non-Repeating variable :-depth of the mill scale bed d)

$$\Pi_3 = l^a, \rho^b, Q^c, T^d, d$$

$$[M^0 L^0 T^0 \theta^0] = [M^0 L^1 T^0 \theta^0]^a [M^1 L^{-3} T^0 \theta^0]^b [M^0 L^3 T^{-1} \theta^0]^c [M^0 L^0 T^0 \theta^1]^d [M^0 L^1 T^0 \theta^0]$$

For M,b=0

For L,a+3c-3b+2=0

$$a+3c-3b+2=0 \dots \dots \dots (3)$$

For T,c=0 putting in eq(3)

$$a=-1$$

For θ,d=0

$$\Pi_3 = \frac{d}{1}$$

4) Π_4 term calculations :- (Non-Repeating variable :-Specific heat of the reaction C_p)

$$\Pi_4 = l^a, \rho^b, Q^c, T^d, C_p$$

$$[M^0 L^0 T^0 \theta^0] = [M^0 L^1 T^0 \theta^0]^a [M^1 L^{-3} T^0 \theta^0]^b [M^0 L^3 T^{-1} \theta^0]^c [M^0 L^0 T^0 \theta^1]^d [M^0 L^2 T^{-2} \theta^{-1}]$$

For M,b=0

For L,a+3c-3b+2=0

$$a+3c-3b+2=0 \dots \dots \dots (4)$$

For T,-c-2=0

$$C=-2$$

Substituting in eq.(4)

For θ,d=1

$$\Pi_4 = \frac{l^a C_p T}{Q^2}$$

5) Π_5 term calculations :- (Non-Repeating variable :- Specific surface area of powder S)

$$\Pi_5 = l^a, \rho^b, Q^c, T^d, S$$

$$[M^0 L^0 T^0 \theta^0] = [M^0 L^1 T^0 \theta^0]^a [M^1 L^{-3} T^0 \theta^0]^b [M^0 L^3 T^{-1} \theta^0]^c [M^0 L^0 T^0 \theta^1]^d [M^1 L^2 T^0 \theta^0]$$

For M,b-1=0

For L,a+3c-3b+2=0

$$a+3c-3b+2=0 \dots \dots \dots (5)$$

For T,c=0

$$a=1$$

Substituting in eq.(5)

$$a=1$$

For θ, d=0

$$\Pi_5 = 1 \rho S$$

6) Π_6 term calculations :- (Non-Repeating variable :-time of oxygen blowing t)

$$\Pi_6 = l^a, \rho^b, Q^c, T^d, t$$

$$[M^0 L^0 T^0 \theta^0] = [M^0 L^1 T^0 \theta^0]^a [M^1 L^{-3} T^0 \theta^0]^b [M^0 L^3 T^{-1} \theta^0]^c [M^0 L^0 T^0 \theta^1]^d [M^0 L^2 T^1 \theta^0]$$

For M,b=0

For L,a+3c-3b=0

$$a+3c-3b=0 \dots \dots \dots (6)$$

For T,-c+1=0

$$C=1$$

Substituting in eq.(6)

$$a=-3$$

For θ,d=0

$$\Pi_6 = \frac{Q t}{l^3}$$

7) Π_7 term calculations :- (Non-Repeating variable :-Apparent density of particle ρ_p)

$$\Pi_7 = l^a, \rho^b, Q^c, T^d, \rho_p$$

$$[M^0 L^0 T^0 \theta^0] = [M^0 L^1 T^0 \theta^0]^a [M^1 L^{-3} T^0 \theta^0]^b [M^0 L^3 T^{-1} \theta^0]^c [M^0 L^0 T^0 \theta^1]^d [M^1 L^{-3} T^0 \theta^0]$$

For M,b+1=0 b=-1

For L,a+3c-3b=0

$$a+3c-3b=0 \dots \dots \dots (7)$$

For T,c=0

MODELLING OF OXIDATION PHENOMENON OF MILL SCALE AND ANALYSIS OF INFLUENCING PARAMETERS

Substituting in eq.(7)

$$a=0$$

For $\theta, d=0$

$$\Pi_7 = \frac{\rho_p}{\rho}$$

8) Π_8 term calculations :- (Non-Repeating variable :-Diameter of the tube D)

$$\Pi_8 = l^a, \rho^b, Q^c, T^d, D$$

$$[M^0 L^0 T^0 \theta^0] = [M^0 L^1 T^0 \theta^0]^a [M^1 L^{-3} T^0 \theta^0]^b [M^0 L^{-1} \theta^0]^c [M^0 L^0 T^0 \theta^1]^d [M^0 L^1 T^0 \theta^0]$$

For $M, b=0$

For $L, a+3c-3b+1=0$

$$a+3c=0 \dots \dots \dots (8)$$

For $T, c=0$

Substituting in eq.(8)

$$a=-1$$

For $\theta, d=0$

$$\Pi_8 = \frac{D}{l}$$

9) Π_9 term calculations :- (Non-Repeating variable :-Weight of mill scale W_m)

$$\Pi_9 = l^a, \rho^b, Q^c, T^d, W_m$$

$$[M^0 L^0 T^0 \theta^0] = [M^0 L^1 T^0 \theta^0]^a [M^1 L^{-3} T^0 \theta^0]^b [M^0 L^3 T^{-1} \theta^0]^c [M^0 L^0 T^0 \theta^1]^d [M^1 L^0 T^0 \theta^0]$$

For $M, b+1=0$ $b=-1$

For $L, a+3c-3b=0$

$$a+3c=-3 \dots \dots \dots (9)$$

For $T, c=0$

Substituting in eq.(9)

$$a=-3$$

For $\theta, d=0$

$$\Pi_9 = \frac{W_m}{l^3 \rho}$$

$$f(\Pi_1, \Pi_2, \Pi_3, \Pi_4, \Pi_5, \Pi_6, \Pi_7, \Pi_8, \Pi_9, \Pi_{10}, \Pi_{11}, \Pi_{12}, \Pi_{13}) = 0$$

$$f\left(\frac{l \eta}{\rho Q}, \frac{L}{l}, \frac{d}{l}, \frac{l^4 C_p T}{Q^2}, l \rho S, \frac{Q t}{l^3}, \frac{\rho_p}{\rho}, \frac{D}{l}, \frac{W_m}{l^3 \rho}\right) = 0$$

Weight of Fe_2O_3 in the oxidized product -

$$f(\Pi_1, \Pi_2, \Pi_3, \Pi_4, \Pi_5, \Pi_6, \Pi_7, \Pi_8, \Pi_9, \Pi_{10}, \Pi_{11}, \Pi_{12}, \Pi_{13})$$

$$\begin{aligned} \frac{\text{Weight of } Fe_2O_3 \text{ in the oxidized product}}{\text{Weight of initial mill scale powder}} &= \left[\frac{\eta \times L \times S \times t \times \rho_p \times D \times T}{Q^2 \times \rho^2 \times l^2} \right]^A \\ \downarrow \\ \text{Purity parameter}(P) \text{ or degree of oxidation} &= \left[\frac{\eta \times L \times S \times t \times \rho_p \times D \times T}{Q^2 \times \rho^2 \times l^2} \right]^A \end{aligned}$$

$$P = \Phi \cdot (X)^A$$

Appendix B

The values of C_p of the reaction of oxidation, viscosity of oxygen gas, density of oxygen is dependent on operating temperature and the values can be found out in thermodynamic data book.^[9] In following table B1 the constant values that are used are listed out.

Table B1. Experimental constant values used during the mathematical modeling.

Sr.No.	Description of parameters	Symbol	Value
1	Flow rate of Oxygen	Q	$8.33 \times 10^{-6} m^3/s$
2	Length of the tube	L	0.8 m
3	Diameter of the tube	D	0.05 m
4	Length of mill scale bed	l	0.1 m
5	Apparent density of mill scale	ρ_p	$1578 kg/m^3$
6	Specific surface area of powder	S	$0.15 m^2/kg$
7	Viscosity of oxygen at 1100°C	η	$5.74 \times 10^{-5} Pa \cdot s$
8	Viscosity of oxygen at 1000°C	η	$5.49 \times 10^{-5} Pa \cdot s$
9	Viscosity of oxygen at 900°C	η	$5.23 \times 10^{-5} Pa \cdot s$
10	Density of oxygen at 1100°C	ρ	$0.284 gm/cc$
11	Density of oxygen at 1000°C	ρ	$0.3064 gm/cc$
12	Density of oxygen at 900°C	ρ	$0.3325 gm/cc$

MODELLING OF OXIDATION PHENOMENON OF MILL SCALE AND ANALYSIS OF INFLUENCING PARAMETERS

References

1. F.Bondioli, A.M. Ferrari, C. Leonelli, T. Manfredini, *Syntheses of Fe₂O₃/silica red inorganic inclusion pigments for ceramic applications*, Mater. Res. Bull. 33 (1998) pp.723–729.
2. J. MERIKHI, C. FELDMANN Philips Research Laboratories, "Homogeneous coatings of nanosized Fe₂O₃ particles on Y₂O₃:Eu," JOURNAL OF MATERIALS SCIENCE 35 (2000) pp. 3959 – 3961.
3. J.W. Park, J.C. Ahn, H. Song, K. Park, H. Shin, J.S. Ahn, Reduction characteristics of oily hot rolling mill sludge by direct reduced iron method, Resour. Conserv. Recycl. 34 (2002) pp.129–140.
4. L. Çamci, S. Aydin, C. Arslan, Reduction of iron oxides in solid wastes generated by steelworks, Turkish J. Eng. Environ. Sci. 26 (2002) pp. 37–44.
5. H.-Y. Lin, Y.-W. Chen, C. Li, The mechanism of reduction of iron oxide by hydrogen, Thermochim. Acta. 400 (2003) pp. 61–67.
6. R.M. Cornell, U.Schwertmann "The iron oxide: Structure, properties, reactions, occurrence and uses" WILEY -VCH verlag GmbH,2003
7. B.J. Chen, L. Xu, W. Li, a -Fe 2 O 3 " Nanotubes in Gas Sensor and Lithium-Ion Battery Applications", (2005) pp.582–586.
8. Matsuzaki, S., Shinotake, A., Naito, M., Nishimura, T., Kunitomo, K., & Sugiyama, T.. "Development of Mathematical Model of Blast Furnace" Volume (94), (2006) pp.87–95.
9. M.A. Legodi, D. de Waal, "The preparation of magnetite, goethite, hematite and maghemite of pigment quality from mill scale iron waste", Dye. Pigment. 74 (2006) pp.161–168.
10. A. Pineau, N. Kanari, I. Gaballah, "Kinetics of reduction of iron oxides by H₂. Part I: Low temperature reduction of hematite", Thermochim. Acta. 447 (2006) pp. 89–100.
11. D. Wagner, O. Devisme, F. Patisson, D. Abitzer, P. De Saurupt, N. Cedex, "A Laboratory Study of the Reduction of Iron Oxides By Hydrogen", Sohn Int. Symp. 2 (2006) pp.111–120.
12. R Nowosielski, R Babilas, G Dercz, L Pajk, J Wrona "Structure and properties of barium ferrite powders prepared by milling and annealing" Archives of Materials Science and Engineering.(2007) Vol736,pp.736.
13. Donskoi, E., Manuel, J. R., Clout, J. M. F., & Zhang, Y.. "Mathematical Modeling and Optimisation of Iron Ore Sinter Properties" Isr. JORHAL CHEMESTERY, Volume 47(2), (2008) pp.373–379.
14. Vandna Luthraa,1, Keith F.E. Pratt a, "Fabrication and characterization of Fe1.90Ti0.10O3 gas sensitive resistors for carbon monoxide" Sensors and Actuators B: Chemical Volume 135, Issue 2, 15 January 2009.
15. Wayne A. Brown McGill university "Developing the best correlation for estimating the transfer of oxygen from air to water" Montreal, Canada, H3A 2B2.
16. Lee, J., & Kim, T. "Application of Microwave Heating to Recover Metallic Elements from Industrial Waste." (2010).
17. Zieliński, J., Zglinicka, I., Znak, L., & Kaszkur, Z.. "Reduction of Fe₂O₃with hydrogen" Applied Catalysis A: General" 381(1–2), (2010) pp.191–196.
18. Akimenko, V. B., Gulyaev, I. a., Sekachev, M. a., & Kalashnikova, O. Y.. "Reduced iron powder: Manufacturing problems and prospects." Steel in Translation, 41(7), (2011) pp. 622–626.
19. N. M. Gaballah et al., A. F. Zikry1 "Production of Iron from Mill Scale Industrial Waste via Hydrogen" Open Journal of Inorganic Non-Metallic Materials, 3, (2013). pp.23–28,
20. Zviad Kovziridze*, Paata Khorava, Nunu Mitskevich "Controlled Local Hyperthermia and Magnetic Hyperthermia of Surface (Skin) Cancer Diseases" Journal of Cancer Therapy, 2013, 4, pp. 1262-1271
21. El-Hussiny, N. A., Abdul-Wahab, H. H., Ali, M. M., Omar, A.-L. A.-M., Shalabi, M. E.-M. H., & Moharm, M. R."Effect of Grinding Time of Mill Scale on the Physicochemical Properties of Produced Briquettes and Its Reduction via Hydrogen". OALib, Volume 1(7), (2014), pp.1–10.

MODELLING OF OXIDATION PHENOMENON OF MILL SCALE AND ANALYSIS OF INFLUENCING PARAMETERS

22. Joshi, C., & Dhokey, N. B.. "Study of Kinetics of Mill Scale Reduction: For PM Applications." *Transactions of the Indian Institute of Metals*, Volume 68(1), (2014) pp. 31–35.
23. N.B. Dhokey, M.G. Walunj, U.C. Chaudhari "Influence of water pressure and apex angle on prediction of particle size for atomization of copper powder" *Advanced Powder Technology* 25 (2014) pp.795–800.
24. David R. Gaskell "Introduction to the Thermodynamics of Materials" CRC Press book August 18, (2017) ISBN 9781498757003 pp694.
25. R. Sabban, P. Tarate, N. B. Dhokey "Dependence of degree of oxidation of mill scale on depth of static bed and its modeling with Ansys Fluent" *Transaction of PMAI*, Vol.42(2)December (2016),pp. 7-12.

EFFECT OF PROCESS VARIABLES ON POROSITY AND STRUCTURE PROPERTIES OF PM SINTERED STEELS

Sardey Rigved Pravin¹, Jing Yang^{2*}, Jose Antonio Calero², Narendra Babanrao Dhokey¹

¹Department of Metallurgy & Materials Science, College of Engineering, Pune, India

²AMES-Sintered Metallic Components, Barcelona, Spain

Abstract: In PM sintered materials, porosity generally exist and deteriorate the mechanical properties. Different process routes can lead to distinct pore features, even in materials which contain the same base powder. In this study, the effect of the process variables on the porosity and structure properties of PM sintered steels has been assessed. A comparison between a pre-diffused alloy (Distaloy AE) and a pre-mixed alloy (Mix AE) with identical chemical composition has been carried out to emphasize the influence of the powder preparation method on the pores characteristics and mechanical properties. In each alloy category, two compacting densities and two sintering temperatures are included. Pore characteristics using the parameters of dimension, profile irregularity and elongation were analyzed statistically with image analysis. A correlation of the pore characteristics and the mechanical strength has been discussed.

Introduction

Sintered steels normally exhibit worse mechanical properties than their corresponding fully dense material with the same composition and microstructure, because of the existence of the porosity. Pores reduce the resisting section and cause local stress concentrations, so that they act as sites for crack nucleation and favorable path for crack propagation. The effect of porosity on the mechanical properties depends on the following factors: the volumetric fraction of the pores, their interconnection, size, morphology and distribution^[1-3]. In this study, the effect of the process variables on the porosity and structure properties of PM sintered steels has been assessed. Emphasis of the process variables was put on the base powder preparation methods. Other variables include compaction densities and sintering temperature.

Porosity is characterized in terms of the fraction amount and its morphological parameters which contains size, pore profile irregularity and elongation. Transverse rupture strength was evaluated as representative of mechanical

properties, for trying to correlate the porosity fraction and its morphology to the mechanical properties.

Material systems and image analysis process

The sintered steel of composition Fe-4Ni-1.5Cu-0.5Mo-0.5C (wt.%) was selected as the base material. The powder mixtures were obtained through 2 methods. One way is directly available from the commercial Distaloy AE, added with the 0.5% C into the mix. The other one is by mixing the Fe-Mo alloy with Ni and Cu powder. This pre-mixed powder is designated as Mix AE. 0.6 wt.% Acrawax C was added as a lubricant into the both powders. For each mix, 10 green bars for subsequent transverse rupture strength (TRS) were compacted at two different densities: 6.8 g/cm³ and 7.1 g/cm³. Then 5 were sintered at 1120°C, in 95% N₂/5% H₂ atmosphere, and the rest were sintered at 1290°C, in 85% N₂/15% H₂ atmosphere. Therefore, by combining the different base powder preparation routes, green densities and sintering temperatures, 8 different conditions were produced, as listed in Table 1 together with their nomenclature.

EFFECT OF PROCESS VARIABLES ON POROSITY AND STRUCTURE PROPERTIES OF PM SINTERED STEELS

Table 1 Nomenclature for all the material systems resulted from 8 different conditions

Mixtures	Sintering conditions	Green density	Code
Distaloy AE + 0.5% C	1120°C	6,8 g/cc. 7,1 g/cc.	DL6 DL7
	1290 °C	6,8 g/cc. 7,1 g/cc.	DH6 DH7
	1120°C	6,8 g/cc. 7,1 g/cc.	AL6 AL7
	1290 °C	6,8 g/cc. 7,1 g/cc.	AH6 AH7

Note: "D" and "A" represent for "Distaloy" and "Mix" respectively. The identification codes of 'H' for high temperature and 'L' for low temperature were used. "6" and "7" refer to the two different densities.

Sintered densities were determined by measuring the dimensions and weight, and consequently the porosities were calculated. To explore the porosity characteristic - structure relationship, mechanical properties were evaluated by measuring the transverse rupture strength (TRS) using the universal testing machine.

Image analysis was applied to the usual metallographic characterization to analyze pores characteristic with software Olympus Stream. Unetched metallographic specimens were prepared and observed under an optical microscope. For each material category, 10 different image fields under 200 X were recorded and processed. The pores below the area of $20\mu\text{m}^2$ were disregarded on the accounts of potential discrepancies due to resolution constraints. Finally, a total of 3000-4000 pores were analyzed.

The data of the following parameters was collected for each of the pores to describe its dimensional and morphological characteristics [2]: (1) Area of the metallographic cross-section of the pores; (2) $f_{\text{rough}} = 4\text{LA}/P^2$, where A and P are the area and the perimeter, respectively, of the metallographic cross-section of the pore. This factor is the measure of the pore profile irregularity or how jagged the boundary of the pores is. The smoother the pore boundary, the closer this value is to 1. (3) $f_{\text{elong}} = D_{\min}/D_{\max}$,

where D_{\min} and D_{\max} are the minimum and maximum Feret diameters. This factor represents the elongation of the pore or its elliptical nature. The value ranges between 0 and 1 with 1 being a circle.

Hence, small values of f_{rough} and f_{elong} indicate highly irregular perimeter and elongated geometry. Frequency distribution was plotted to visualize the data and determine the median value (the value at a cumulative frequency of 50 %) which is considered the mean value representing a given set of values.

Results and discussions

Fig.1 illustrates the density and porosity of the investigated materials. Logically, in each category of DL, DH, AL and AH series, higher density corresponds to lower porosity.

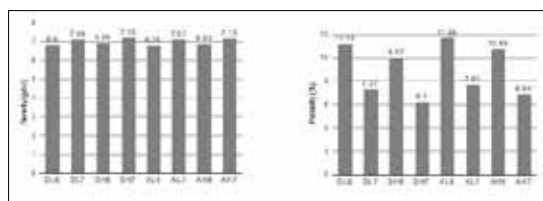


Fig.1 Density (left) and porosity (right) of the 8 material systems

For the category of the same mixture and same green density (D6, D7, A6 and A7), sintering at higher temperature yields higher sintered density and lower porosity. For example, porosity of DH6 as 9.97 is considerably lower than 11.14 of DL6. This is also expected as higher temperature improves the material diffusion and thus densifies the part.

By comparing the D and A series at the same green density and sintering temperature, the A series show higher porosity than those of the D ones, especially at the higher sintering temperatures. This should be relevant to the different mixing nature of the original powders: since in Mix AE, Cu and Ni are separated physically rather

EFFECT OF PROCESS VARIABLES ON POROSITY AND STRUCTURE PROPERTIES OF PM SINTERED STEELS

than partially diffused in Distaloy, the diffusion among different materials in the pre-mixed alloy is slower.

Fig.2 shows the mean values of the morphological parameters of the total pore population for all the 8 material systems. Pore size decrease with higher compacting density. The density seems to have a positive effect on f_{rough} . And f_{elong} is not affected by density.

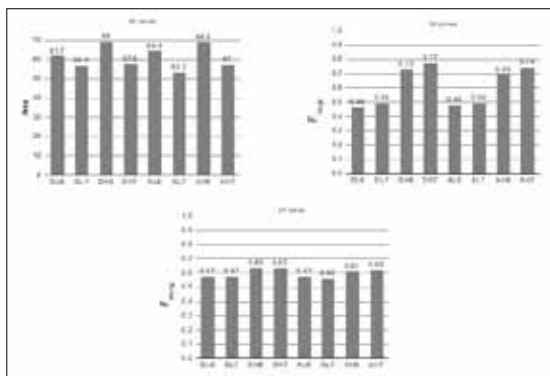


Fig.2 Median values of area, f_{rough} and f_{elong} of the pores for the total pore population

When sintered at higher temperature, pores grow bigger. Also both f_{rough} and f_{elong} increase indicating pores get smoother and rounder, as a result of better diffusion.

The base powder effect on the pore size is not clear, as AL6 shows bigger pores than DL6, but pore size of AL7 is smaller than that of AL6. Furthermore, at higher temperature series, no difference of pore size exist between the D and A materials. Regarding the f_{rough} and f_{elong} difference can hardly be observed between the two alloys.

From the above results, it can be inferred here that among the pore morphological parameters, pore size, f_{rough} are more sensitive than the f_{elong} under the influence of process variables.

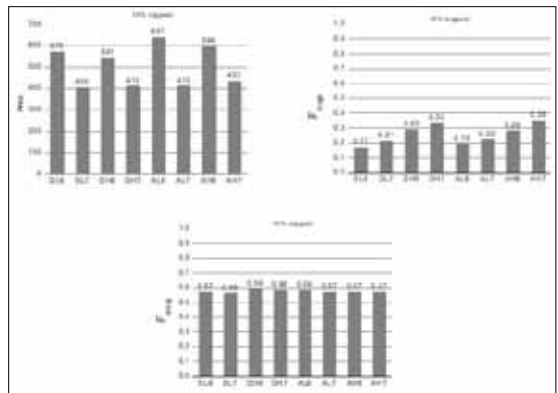


Fig.3 Median values of area, f_{rough} and f_{elong} of the biggest 10% pores

For comparison purpose, mean values of the same parameters referred to the fraction of the 10 % largest pores are plotted (Fig.3), as they are of great interest from a mechanical point of view [4]. It confirms the effect of density and sintering temperature on pore morphology, as illustrated by the global pore population.

However, not like the total pore population, size of the top 10% pores only increase with sintering temperature on the density 7 series, while on the density 6 series, the largest pore size decrease when sintered at higher temperature. Considering that for both the two densities 6 and 7, pore size for the total pore population increase, it is assumed that for the lower density material, the growth of pores only take place on the smaller pores with sintering temperature increased, compensating the shrink of the largest pores.

The base powder shows more evident effect on the pore size for the largest pores than for the overall pore results, indicating that for the A series, pore size distribution is more heterogeneous than the D series.

The above results about influence of process variables on porosity, pores morphology have been summarized in table 2.

EFFECT OF PROCESS VARIABLES ON POROSITY AND STRUCTURE PROPERTIES OF PM SINTERED STEELS

Table 2 Influence of process variables on porosity, pores morphology and TRS values

All Pores	Porosity	Morphology			TRS
		Size	f_{rough}	f_{elong}	
Green Density \uparrow	\downarrow	\downarrow	\uparrow	\sim	\uparrow
T \uparrow	\downarrow	\uparrow (*biggest pores \downarrow for density 6 series)	\uparrow	\uparrow	\uparrow
D to A	\uparrow	*(*biggest pores \uparrow)	\sim	\sim	\downarrow

Note: The dashed arrow indicates that the trend is slightly observed. The tilde means no difference exists. The cross points out that the effect is not clear and the asterisk marks the upside-down behavior observed for the top 10% biggest pores.

For both the D and A materials, strength increase with the higher density and temperature as expected (Fig.4). The less amount of porosity found on higher density and temperature is attributed to the results. The data of pore geometry on the specimens of higher density is also consistent with the findings here, as pores are smaller and smoother. However, sintering temperature has a synergic effect on the pore geometry, as the overall pores grow bigger but get smoother when sintered at higher temperature. Nevertheless, to combine pore morphological parameters with correlation to strength here is uncertain, since these materials have different porosities which play dominant role on the TRS.

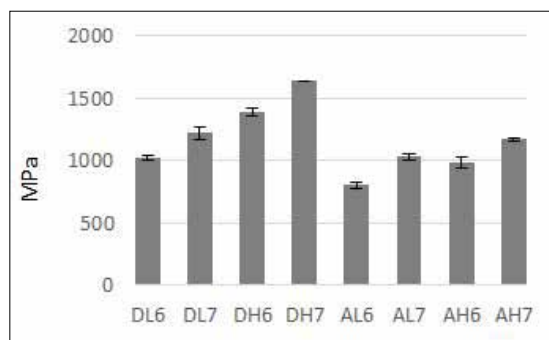


Fig.4 TRS values for all the material systems studied

Considering the base powders effect, TRS values of A series is notably lower than that of D series, particularly if they are compared at the higher sintering temperature serie. Again, this result is directly relevant to their porosities resulted from the difference in diffusion nature of the two materials.

Interestingly, it is noted here that for each density series, the difference in porosity leads to certain proportion to their difference in TRS. As list in Table 3, at the density 6 series, the difference in TRS and porosity ratio is around 4, and at the density series 7, the ratio becomes 3.

Table 3 The difference in porosity and TRS values as well as their ratios between the D and A series

Density Serie	Δ Porosity	Δ TRS	Δ TRS/ Δ Porosity
6	Δ DL6-AL6	4.6	21
	Δ DH6-AH6	7.2	4.17
7	Δ DL7-AL7	5	3.00
	Δ DH7-AH7	10	2.90

4. Conclusion

- (1) Concerning pores fraction, sintering at higher temperature yields higher sintered density and lower porosity. The pre-mixed A series show higher porosity than those of the pre-diffused D ones, especially at the higher sintering temperatures.
- (2) With higher compacting density, pore size decrease, its profile get slightly smoother without affecting its elongation factor. When sintering temperature increases, pores grow bigger globally, except that for the lower density 6 series, the top 10% pore size decrease. Also pores get smoother and rounder, as a result of better diffusion. Powder mixing effect on the pore morphology is not clear globally. However, the top 10% pore size is clearly bigger in the pre-mixed A series than that in the pre-diffused D series.
- (3) For both the pre-diffused D and pre-mixed A materials, strength increase with the density and temperature as expected. Considering

EFFECT OF PROCESS VARIABLES ON POROSITY AND STRUCTURE PROPERTIES OF PM SINTERED STEELS

the base powders effect, TRS values of A series is notably lower than that of D series. This result is directly relevant to their porosities resulted from the difference in diffusion nature of the two materials.

References

1. Piotrowski A, Biallas G. *Powder Metall* 1998; 41(2): 109.
2. Marcu T, Signorini M, Molinari A, Straffelini. 2003; 50:1-10.
3. Stoyanova V, Xu C, Blanco L, Molinari A, Danninger H, Torralba J.M, Yu Y, Linquist B. *Proceedings Euro PM2004*, Vienna, 17-21 Ocotober 2004. Shrewsbury (UK): EPMA; 2004. Vol.3. p.46.
4. Beiss P, Dalgic M. 2001; 67: 37-42.

DESIGN OF NEW BONDS WITH MINIMUM COBALT FOR THE DEVELOPMENT OF DIAMOND WIRE ROPES

Rajkumar Yembadi^{*1}, Ravi Bollina¹, Ram Kollareddy¹, Bharat B. Panigrahi²

¹RDT Diamond Tools Pvt. Ltd., Banjara hills, Hyderabad, Telangana, India

² Department of Materials Science and Metallurgical Engineering,
Indian Institute of Technology Hyderabad, Kandi, Telangana, India

Abstract: The present work reports the development of new metallic binders to use in the diamond cutting tools (DCT'S) for the stone cutting application. Two different grades of alloy powders were developed using specially designed prealloy powders and evaluates their performance during infiel cutting operations. The basic concept of making DCT'S varies from industry to industry on an impecical basis without proper evaluation of the individual powders/alloys. Cobalt (Co) is volatile in pricing and causes unforeseen problems in wire production. Hence the goal is to have minimal cobalt in the diamond wire saws. In this work, a rigorous attempt has been made to replace the Co-base alloys with fine prealloy powders with less dependence of Co, which is economical globally.

Most of the present DCT'S are fabricated by hot pressing (HP) or hot isostatic pressing (HIP), which are may not be suitable for industry level production. Whereas conventional cold pressing/sintering processes increase the production rate in cost a effective manner. But this route needs close control of processing parameters to avoid the diamond graphitisation/ loss of bond strength, which could deteriorate the cutting performance.

RDT (Reliance Diamond tools) has designed two different grades of metallic binders, which consist Fe and Cu as two major alloying elements with the minimum content of Co; and studied the effect of reinforcement (Tungsten carbide (WC), Phosphorous (P)) on the final properties of the tool. The thermal behaviour of the powders was studied using differential scanning calorimeter (DSC) to optimize the composition of the binder and processing parameters. Powders obtained from the different sources were mixed and compacted using steel dies with 60 bar pressure. The green compacts were assembled with steel shims and sintered using continuous belt furnace in a controlled hydrogen atmosphere at various temperatures from 850-1000°C. Sintered products were analysed for hardness, density, and microstructure. It has been found that the new metallic binders look attractive since they combine good sinterability and adequate values of hardness and wear resistance. The unique feature of this study is that the trail bonds sintered were assembled as full wires of 50m and cutting carried out in various granite mines in south India on industrial scale. The microstructural studies revealed that the interaction between metal powders and diamond is extremely good throughout the wire cutting, which improved the service life and the cutting speed of the wire saw compared to existing ones.

Introduction

Diamond wires are cutting tools for stones (marble, granite, etc.) and concrete. They are composed of a stainless steel cable on which diamond sintered beads, containing synthetic diamond particles are assembled with a regular space between them [1,2]. A sintered bead is a composite material contains super-abrasive

grains (diamond) hold in a metallic matrix. The main functions of the metal matrix are to hold the diamond grains tightly (the diamond crystal has to protrude from the matrix during the whole cutting action) to prevent the premature detachment of the diamonds from the matrix, and should wear at a rate compatible to that of the diamond [2-5]. Selection of a suitable matrix

DESIGN OF NEW BONDS WITH MINIMUM COBALT FOR THE DEVELOPMENT OF DIAMOND WIRE ROPES

material when manufacturing diamond tool is a key engineering consideration. Cobalt (Co) base alloys have been regarded as the best matrix materials with a good combination of high temperature hardness, toughness, and self-sharpening abrasion. However Co is volatile in pricing and causes unforeseen problems in wire production. Thus, other alternative economical metals are required to be used in diamond cutting tools (DCT'S). The search for novel metallic binders to be used for the fabrication of diamond cutting tools has produced an intensification of research activities in this field, thus widening the choice of metal powders for this purpose. The industry's evolving technological sophistication has led to the development of several low-cobalt and cobalt-free powders which consist of a combination of at least two elements, which are co-precipitated to yield pre-alloyed agglomerates of submicron-sized particles.

Most of the present DCT'S are fabricated by hot pressing (HP) or hot isostatic pressing (HIP), which are may not be adaptable for industry level production [7]. On the other hand, the conventional cold pressing/sintering increases the production rate in a cost effective manner. But this route needs a close control of processing parameters to avoid the diamond graphitization/loss of bond strength, which could deteriorate the cutting performance [7, 8].

Therefore in this work, a study to process and characterize the Fe-Cu alloys with reduced cobalt is shown. Two different matrixes were produced using different prealloy powders with variable cobalt content. Analysis of diamond bead wear is of paramount importance because it is what comes closest to the reality of the application. There are some studies about the determination of cutting performance of diamond bead in literature, but hardly few studies are related with the variation of cutting performance of the bead on its lifetime. So this work also focussed on real-time analysis of the diamond

wire and the cutting process at various kind of granite quarries in order to increase operating capabilities.

Experiment

The characteristics of the prealloyed powders and individual powders are summarised respectively in Table 1. Two different matrixes (R1, R2) were prepared as per calculated weight ratios using two different prealloyed powders with minimum and variable cobalt (as mentioned in table 1). For all the trials additions of 10wt% Tungsten carbide (WC) and 1.5 -2% Phosphorous (P) were added to the pre-alloy mix.

Table 1: Characteristics of the powders used in matrix formation

Powder	Composition	FSSS (μm)	Apparent density (g/cc)
Prealloy powder (R1)	Fe – bal. Cu – 25-30% Co – 7-9% Sn & Ni – 5%	15-18	3.25
Prealloy powder (R2)	Fe – bal. Cu – 21-25% Co – 10-13% Sn & Ni – 8%	15-18	2.90
Tungsten carbide (WC)	10%	3-5	4.0
Phosphorous (P)	1.5%	3-5	

Matrix powders (R1 and R2) along with WC and P were mixed thoroughly in a 3D-turbula mixer for 2h as per the calculated chemical composition followed by wet mixing in a planetary mixer [by adding different grades of diamond powders]. Then the powder mixes were pressed at 350MPa pressure to produce green compacts of diameter 12.7mm and 3.5gr in weight. The green beads immediately put on top of the copper coated steel shims and arranged on graphite plates for sintering in a continuous furnace. All the samples were sintered at 3 different temperatures of 850°C, 900°C and 950°C under the hydrogen atmosphere. After densification, all the specimens were subjected to density measurements and hardness tests. The water displacement technique and Rockwell

DESIGN OF NEW BONDS WITH MINIMUM COBALT FOR THE DEVELOPMENT OF DIAMOND WIRE ROPES

B method were used, respectively. The reported results are average of at least 5 measurements. The microstructure of the sintered beads was carried out using a scanning electron microscope (SEM-carlzeiss). The thermal behaviour of the powders was studied using differential scanning calorimeter (DSC, Netzsch 404 F3) up to 1100°C at a heating rate of 10°C/min under Ar atmosphere. Real-time wear behaviour of the diamond bead was examined at various granite mines using 60Hp motor wire saw machines.

Results And Discussion

Figure 1 show the DSC pattern of the two matrixes (R1 & R2) prepared from respective prealloy powders. The DSC profile of R1 has three endothermic peaks at various temperatures of 790°C, 810°C, and 990°C. Whereas the DSC profile of R2 has the only endothermic peak at 990°C, which represents the melting of bronze. The other two low intense endothermic peaks at 790°C and 810°C are resulted due to the active diffusion of Cobalt (Co) and Tin (Sn) into Fe and Cu respectively [9], which forms the solid solution of Fe and Cu (as reported in Fig. 2). Since the diffusion of atoms activated at around 800°C, the temperature region of 850-900°C is suitable for sintering of R1 and 900-950°C for R2.

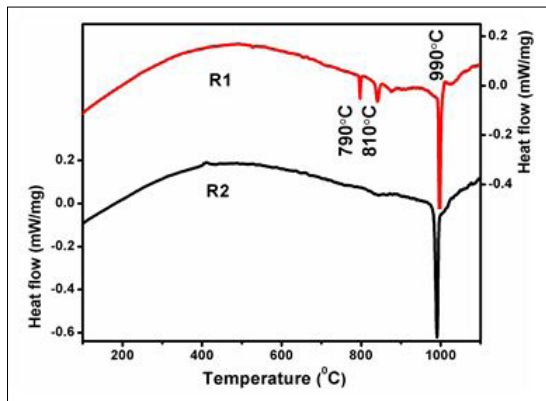


Fig. 1: DSC pattern of R1 and R2 powder mixtures.

Figure 2 shows the XRD pattern of the diamond bead sintered at 950°C. The XRD spectrum for both the binders remains the same. The X-ray profile of the sample indicates the presence of Fe, Fe-Co solid solution and copper-based solid solution (Cu-Sn). The high intensity of the WC peaks in the XRD profile indicates that there is no any reactivity of WC with Co. Due to the low content of P and Sn, their presence could not be identified in XRD pattern.

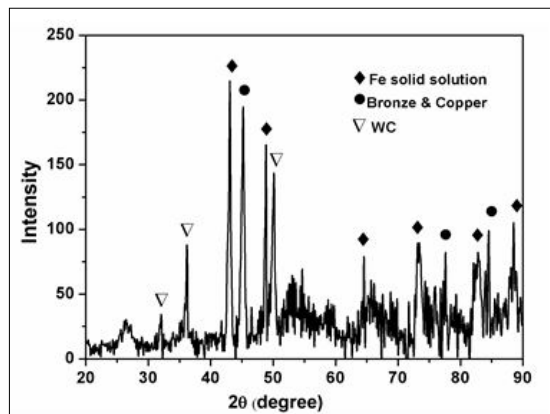


Fig. 2: XRD pattern of the bead sintered at 950°C

Figure 3 (a & b) show the SEM images of the blank matrix of R1 and R2 sintered at 900°C and 950°C. From the microscopic images, it is clear that the dimple nature is dominant with very low porosity in both the bonds. The dimple nature is more prominent in R1 than R2, because of early shrinkage and more content of Tin in R1. The broken surface of the R2 has large no.of voids than R1, due to evaporation of Sn at 950°C, which takes away the surrounding copper causes the formation of voids. Fig 3(c & d) show the fracture surface of R1 and R2 beads indicates the strong bonding of diamond with the metal matrix. There was no sign of diamond graphitization or pullout in the matrix, even after heating at 950°C.

DESIGN OF NEW BONDS WITH MINIMUM COBALT FOR THE DEVELOPMENT OF DIAMOND WIRE ROPES

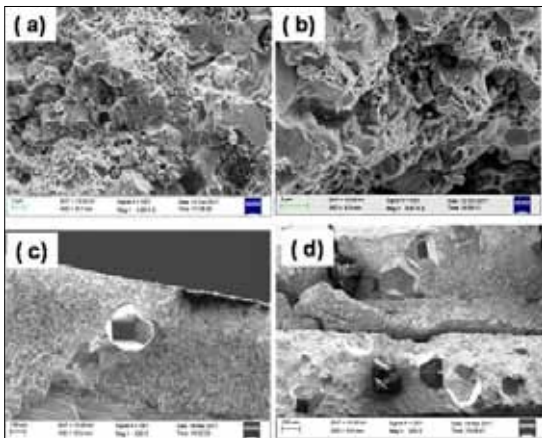


Fig. 3: (a, b) Fracture surface of the blank matrix R1 and R2 sintered at 900°C and 950°C respectively, (c, d) Fracture surface of the sintered beads made up of R1 and R2 matrixes, respectively

Mechanical properties of the bonds sintered at different temperatures are listed in Table 2. The hardness and the density of the bonds increase with an increase in sintering temperature. At 850°C, the hardness and density of R1 and R2 are very low because of slow atomic diffusion and migration of atoms. As the temperature increased up to 900°C, R1 attains the maximum density and hardness, which decreased in further increment of temperatures. Whereas the R2 bond mechanical properties improved from 900°C to 950°C effectively.

Table 2: Mechanical properties of the bonds at various temperatures

Bond	Density (g/cc)			Hardness (HRB)		
	800°C	900°C	950°C	800°C	900°C	950°C
R1	6.95 (85% of T.D)	7.816 (95% of T.D)	8.146 (98% of T.D)	68-74	98-100	94-96
R2	6.99 (86% of T.D)	7.647 (94% of T.D)	7.947 (98% of T.D)	67-69	92-94	96-100

Analysis of cutting report

There are several parameters affecting on diamond wire cutting operation, such as wear of the bead, structure of the bead, machine vibration, hoop rotation and hardness of the stone to be cut [10]. If the Control of wear rate of the bead is optimal, it decreases the cost of diamond wire cutting method. Similarly, the cutting speed is one more important parameter to address the cutting performance of the diamond wire. Both the diamond wires made up of R1 and R2 matrixes (each wire of 50 meters) were tested in soft granite (black galaxy) until the bead completely lost its cutting ability. The 60HP motor wire sawing machines were used and cutting was performed using similar parameters for both the wires. At the start of initial cutting, the wires were twisted as hoop diameter for proper rotation of the bead to ensure the uniform cutting throughout the wire.

Generally, the cutting performance of the diamond wire evaluates in terms of cutting rate/ wear rate and cutting life. So the data obtained from the granite mines were arranged in a chart for both R1 and R2 wires and analyzed the tool life and cutting rate as a function of bead diameter. During the initial stage of cutting, the cutting rate was slow with minimum wear rate, which was expected. Because initially, the diamond faces from the matrix has to be opened to speed up the cutting. It was noticed that for the next 4 to 5 cuttings (middle stage) the cutting rate of both wires was increased and almost constant with uniform wear throughout the bead length. This is due to the diamonds on the bead surface were completely exposed and the height of the protrusion is sufficient, which is necessary for good performance. At the final stage of the cuttings (6-10 cuts) the wear rate and cutting speeds were high due to the lack of holding from the matrix and low height of protrusion from diamond, which causes premature diamond pullout/breaking. The relation between the

DESIGN OF NEW BONDS WITH MINIMUM COBALT FOR THE DEVELOPMENT OF DIAMOND WIRE ROPES

decrease in bead diameter and cutting rate of the bead obtained from the cutting process has been given in Fig. 4 for R1 and R2 respectively. The highest rate of cutting was seen on the bead diameter in the range of 10.5mm to 9.5mm. Both the bonds show almost similar average cutting rate, but during initial stages, the cutting rate of R2 was lower than the R1 because of the high hardness of the matrix.

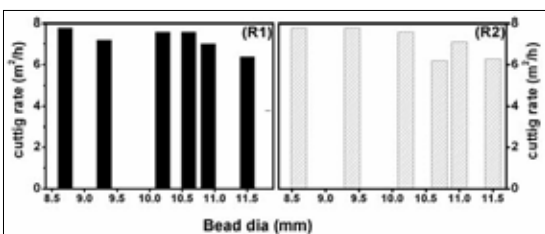


Fig. 4: Relationship between bead diameter and cutting rate of the diamond bead (a) for diamond wire R1, (b) for the diamond wire R2.

The cutting life of the wires made up of R1 and R2 bonds was calculated till the end of cutting and the results compared with the cutting life of cobalt-rich diamond wires. It was noticed that the cutting life of R2 (1118Sqm) was slightly higher (3%) than R1 (1084Sqm) (shown in Fig. 5). Moreover, the cutting performance of these wires is very much comparable with the cobalt-rich bonds, which are expensive for the stone processing. Overall the two newly designed bonds made up of fine prealloy powders with minimum cobalt looks attractive and comparable with cobalt-rich and other expensive bonds in terms of cutting life and cutting rate. The comparison of cutting rate and life of R1 and R2 ropes has been given in Fig. 5. Even though there is a difference in cobalt content of R1 and R2 bonds, it does not affect the cutting performance in case of soft granite (black galaxy). It may not be similar in hard granites, needs to be studied furtherly.

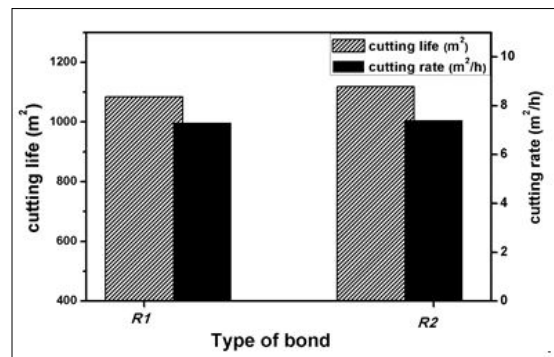


Fig. 5: Analysis of the cutting report from the diamond wires made up of R1 and R2 bonds.

4. Conclusion

1. The metal bonds designed using prealloy powders with minimum cobalt looks attractive in terms of bonding and cutting performance. The cutting performance of the present bonds is almost similar to the cobalt-rich bonds, fraction of the cost of cobalt rich bonds which are economical for the stone processing.
2. The sintering parameters were optimized successfully and achieved maximum density and hardness well below the 1000°C through pressureless sintering (free sintering).
3. Real-time analysis of the diamond bead cutting was carried out and correlated the wear rate as a function of bead diameter. The cutting performance of both the bonds (R1 and R2) prepared in the present work exhibited in similar fashion for soft granite (black galaxy).

Acknowledgment

RDT Diamond Tools and Midwest Granite Pvt. Ltd. are gratefully acknowledged for their financial support and co-operation in diamond wire production and evolution of its cutting performance. Mr. Vijender Reddy from RDT

DESIGN OF NEW BONDS WITH MINIMUM COBALT FOR THE DEVELOPMENT OF DIAMOND WIRE ROPES

Diamond tools also highly acknowledged for his continuous support in wire production. The authors wish to thank IIT Hyderabad for their support in providing DSC and SEM facilities.

References

1. Marcello Filgueiraa, Guerold Bobrovitchia, Daltro Garcia Pinattib. A New Route to Process Diamond Wires, *Material Research*, 6 (3), (2003) 327-333.
2. J. Konstanty. *Powder Metallurgy of Diamond Tools*, 1st Edition, Elsevier, (2005).
3. M. del Villar, P. Muro, J.M. Sánchez, I. Iturriza & F. Castro. Consolidation of diamond tools using Cu-Co-Fe based alloys as metallic binders, *Powder Metallurgy*, 44:1, (2001) 82-90.
4. Oliveira Luciano & Filgueira Marcello. Diamond beads obtained by powder metallurgy: Technology nationalization, *Matéria (Rio de Janeiro)*, 13, (2008) 23-32.
5. Romanski A. Factors affecting diamond retention in powder metallurgy diamond tools, *J. Archives of Metallurgy and Materials*, 55 (4), (2010) 1073-1081.
6. Bertjan K, Anja S. Cobalite and nickel free bond powder for diamond tools: Cobalite CNF, [J]. *Industrial Diamond Review*, 1, (2004) 26-32.
7. ASM HANDBOOK, *Alloy Phase Diagrams*, 3rd ed. 3, (1979) 168.
8. K. Emre Oksuz, Yusuf Sahin, Ebru Sahin Yildirim, Yunus Kayir. The Effect of B4C Additions on Mechanical Properties of Fe-Cu-Co Matrix Composites for Diamond Tools, *Advanced Materials Research*, 685, (2013) 30-34.
9. G. Weber, and Weiss, C. Diamix - A Family of Bonds Based on Diabase - V21, *Industrial Diamond Review*, 2, (2005) 28-32.
10. Xie, D., Wan, L., Song, D. et al. *J. Wuhan Univ. Technol.-Mat. Sci. Edit.* 31, (2016) 805.
11. J. Konstanty, A. Romanski, H. Frydrych. Effect of mechanical properties of the matrix on its diamond retention capacity and wear characteristics during sawing hard stone by means of diamond impregnated tools, in *Proceedings of 2000 Powder Metallurgy World Congress*, Kyoto, November 12-16, (2000) 1629-1632.
12. S. Spriano, Q. Chen, L. Settineri, S. Bugliosi, Low content and free cobalt matrixes for diamond tools, *Wear*, 259(7-12), (2005) 1190-1196.
13. He Dai, Limin Wang, Jingguo Zhang, Yibo Liu, Yuefa Wang, Lei Wang & Xinliang Wan. Iron based partially pre-alloyed powders as matrix materials for diamond tools, *Powder Metallurgy*, 58:2, (2015) 83-86.

MANUFACTURING AND CHARACTERIZATION OF ALUMINIUM METAL MATRIX COMPOSITE

Prof. Madhuri Deshpande¹, Prof. (Dr.) S.T. Vagge²

¹ Department of Production engineering, Vishwakarma Institute of Technology, Pune, India

² Department of Metallurgy and Materials Science, Govt. College of Engineering, Pune. India

Abstract: Carbon fiber reinforced Aluminium metal matrix composites are potential materials for aerospace and electronic industries. Various manufacturing methods that would give uniform distribution of carbon fibers are adopted to manufacture this composite. In the present work, different manufacturing methods of composite manufacturing like Stir casting, Cold Iso-Static Pressing and Hot Pressing were tried with AA 7075 as matrix and Nickel coated and uncoated milled carbon fibers as reinforcing material. Powder Metallurgy route appeared to be the best amongst the methods that have been tried and was used for composite manufacturing subsequently. Uncoated and Nickel coated carbon fibers were mixed with AA 7075 powder in different volume contents, after thorough mixing, the mixture was pressed by single action and double action vacuum assisted hot press. Effect of single action and double action on densification was studied. Effect of contents of uncoated carbon fibers and coated carbon fibers on hardness was also studied. Optical and Scanning electron microscopic examination was carried out.

Vacuum Hot pressed composites exhibited uniform distribution of carbon fibers and also good bonding between fibers and matrix. Results of X-ray diffraction (XRD) revealed that Al_4C_3 formation was absent. In case of uncoated carbon fibers, as the amount of carbon fiber content increased, hardness decreased. However, with Nickel coated carbon fibers hardness increased as amount of coated fibers increased. Composites with graphite flakes also exhibited good bonding with the matrix and uniform distribution. Higher densification was observed in double action pressing. Density shows drop as carbon fiber content increases.

Introduction

Demand for advanced, tailor made materials is increasing day- by- day to meet upcoming newer and newer requirements of engineering components as well as to replace existing materials for better performance. This quest significantly contributed to the development of newer materials. Metal matrix composite (MMC) materials are one such class of materials with variety of matrices and reinforcement materials. In modern electronics, due to miniaturization, density of microelectronic chips and faster speed leads to increase in power level that causes large amount of heat generation. This heat needs to be dissipated for reliable working and longer performance of electronic components. Thus thermal management has become very crucial in modern microelectronics. Monolithic materials

like Copper and Aluminium though having higher thermal conductivity (TC) are not suitable due to high Co-efficient of Thermal expansion (CTE). Metals like Molybdenum and Tungsten have low CTE but also have low TC. Diamond though possesses required combination i.e. high TC and low CTE but due to high cost it's use is limited [1]. Combinations such as Cu-Mo, Cu-W are also not suitable due to their high density [2]. Aluminium does not have thermal conductivity as that of Copper but due to it's light weight, it is attractive for such application. Properties of Aluminium are further improved by reinforcing it with conducting material. It is a very dominant matrix for Metal matrix composites for electronic as well as structural applications. Various alloys of Aluminium such as Al-Si, Al-Si-Mg, Al-Cu, Al-Zn-Mg have been

MANUFACTURING AND CHARACTERIZATION OF ALUMINIUM METAL MATRIX COMPOSITE

extensively used as matrices by researchers. AA 7075, a popular aerospace material is used in this study as matrix material to enhance its thermal properties. Carbon materials in various forms such as fibers, flake, nano tubes, sheet are used as reinforcement. Carbon fiber can be used in milled, chopped or in continuous form due to its high specific strength, specific modulus, light weight, low coefficient of thermal expansion, high thermal and electrical conductivity [3]. Polyacrylonitrile (PAN) based carbon fibers improve mechanical properties [2-5] while Pitch base fibers improve thermal properties [6,7]. Depending upon requirement, suitable type of carbon fibers are used as reinforcement. In the present work, milled Pitch based carbon fibers are used as reinforcement.

Various Liquid and Solid state methods are used for making Aluminium metal matrix composite (AMC). Many researchers have adopted Liquid Metallurgy route like Stir casting [3], Liquid infiltration [8] and Squeeze casting [9] to process AMC due to its ease and simplicity of processing. [2,3,10,11].

Among Solid state methods, Powder Metallurgy is most widely used by the researchers [7,8,10,11] for the manufacturing of fiber/particulate reinforced composites. Recently Friction Stir processing is tried for composite manufacturing [12].

In the current research, attempts are made to make composites of AA 7075 using different volume contents of Pitch based milled carbon fibers, by different methods and identify the best method. Nickel coated carbon fibers as well as graphite flakes were also used as reinforcements. Composites thus produced were characterized for various properties.

Experimental

A. Raw materials

Aluminium alloy (AA 7075) powder having spherical shape with average particle size of 35 μm which is purchased from AMPAL INC (Table 1 shows chemical composition of AA

7075) and the reinforcement material used was pitch based milled uncoated carbon fibers (10 μm diameter and 200 μm length) purchased from MITSUBISHI PLASTICS, INC. PAN based carbon fibers, purchased from Nikunj Exim, Mumbai were also used (Aspect ratio ~625). To improve wettability, Pitch based fibers, after pretreatment, were subjected to electro less nickel coating as described in our earlier work [13]. Wrought AA 7075 was purchased from Bharat Aerospace Metals, Mumbai. Fig. 1 a shows the surface morphology of the uncoated carbon fiber and b shows AA 7075 powder.

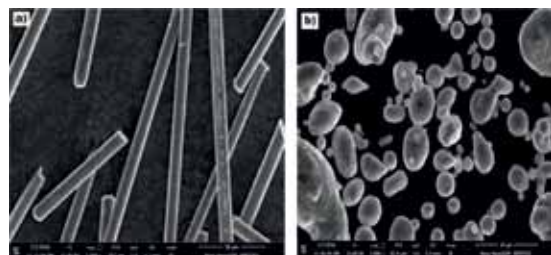


Fig. 1 a SEM images of as received Pitch based carbon fiber; b. SEM image of as received AA 7075 alloy powder

Table 1 Chemical composition of AA 7075 powder

Element	Cu	Mg	Zn	Si	Fe	Ti	Mn	Cr	Al
Wt%	1.2-2	2.1-2.9	5.1-6.1	0.4	0.5	0.2	0.3	0.2-0.3	Rest

Fig. 2 a shows uniformly Ni coated carbon fiber and b shows the EDS analysis of the Ni coated carbon fiber. Graphite flakes (3610) were supplied by ABSURY CARBON had diameter 180 μm and 8 μm thickness. Fig. 3 a and b shows morphology of flakes.

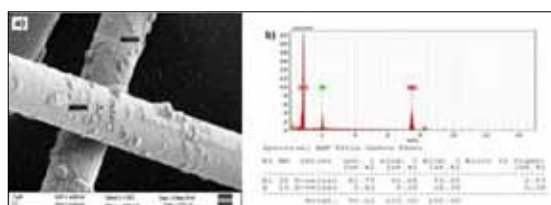


Fig. 2 a. SEM image of nickel coated fiber; b. EDS Analysis of electro less nickel plated Carbon fiber

MANUFACTURING AND CHARACTERIZATION OF ALUMINIUM METAL MATRIX COMPOSITE

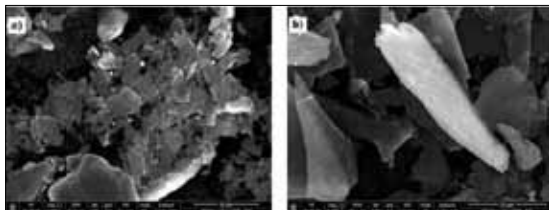


Fig. 3 a and b Morphology of Graphite flakes

B. Fabrication of composite

Aluminium alloy (7075) matrix composites with pitch based uncoated carbon fiber and Ni coated carbon fiber reinforcement were prepared by Stir casting, Cold Iso static pressing and Vacuum Hot pressing. Composites with graphite flakes were prepared by Vacuum Hot pressing.

1. Stir Casting

Metallic die was preheated to temp around 300° C. To the melt of AA 7075, carbon fibers were added and then poured into the preheated die. The mixture was manually stirred and then poured into the mold. It was observed that some carbon fibers were stuck at the bottom of mold and others were partially embedded in the bottom of the casting. Majority of the fibers were floated at the top surface of the casting. Fibers could be easily pulled out from the matrix even by hand. Fig. 4 represents the process schematically. Fig. 5 a shows die used and Fig. 5 b shows the casting that is obtained thereafter.

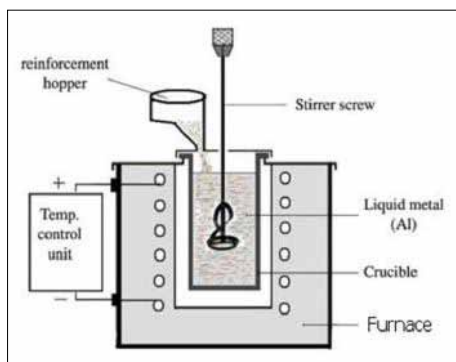


Fig. 4 Schematic of Stir Casting



Fig. 5 a. Die for casting b. Casting

For better distribution of carbon fibers, composite was cast after magnetic stirring (200-1000 rpm.). The mixture was magnetically stirred for 20 mins. Even with this, fibers remained in lumps, only distribution of lumps increased. Fig. 6 a shows SEM image of the composite showing distribution of fibers and Fig. 6 b shows fractured casting.

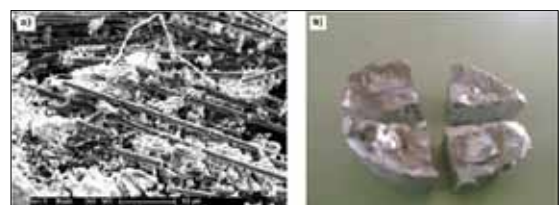


Fig. 6 a. Composite with electromagnetic stirring
b. Casting

Liquid Metallurgy route is easier and simpler method of composite manufacturing but carbon fibers exhibit high reactivity with Al and it's alloys, which is the main problem encountered in this technique. Given below are the problems encountered in this technique:

- 1) Poor wettability between carbon fibers and matrix material i.e. Aluminium.
- 2) Formation of interfacial reactions (Al_4C_3) which is detrimental to mechanical as well as thermal properties.
- 3) Volume of reinforcement is limited in the matrix.
- 4) Surface modification of the reinforcement material is essential to avoid the interfacial reactions.
- 5) Non uniform distribution of fibers.

MANUFACTURING AND CHARACTERIZATION OF ALUMINIUM METAL MATRIX COMPOSITE

Apart from these problems, the fibers which were used had very high aspect ratio (~62) which also contributed to poor distribution of fibers.

Most common method of wettability improvement is Nickel coating to carbon fibers, which is used in this work. Fig. 7 a shows laboratory set up developed for Electro-less Nickel coating of carbon fibers and Fig. 7 b shows SEM image of Nickel coated carbon fibers. Fig. 8 shows EDS Analysis of electro less nickel plated Carbon fiber thus obtained from which it is observed that small amount of Phosphorous is also present in the coating along with Nickel.

Composite manufacturing with coated fibers was tried by the same method as described above. Even by using coated fibers, fiber distribution did not improve. So, Solid state method was tried.

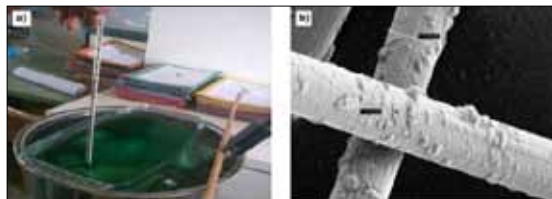


Fig. 7 a. Bath for Nickel Plating b. SEM image of nickel coated carbon fiber

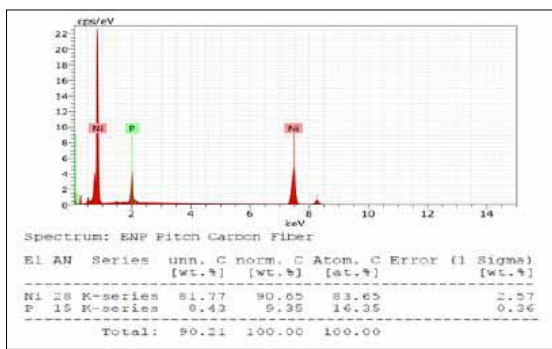


Fig. 8 EDS Analysis of electro less nickel plated Carbon fiber

Composite manufacturing was tried by Cold Iso Static Pressing (CIP) as under-

For this trial, powder mixtures of Carbon fiber and AA 7075 varying from 10 to 50 Vol% including pure AA 7075 were prepared by blending it in camphor (2 wt %). The mixture was then filled in rubber bags of dimensions dia. 90 mm*20 mm. (Fig. 9 a). After filling, the bags were sealed and put in the water chamber. Those bags were pressed iso-statically at 200 bar pressure for one hour. Then rubber bags containing green compacts were removed. (Fig. 9 b)

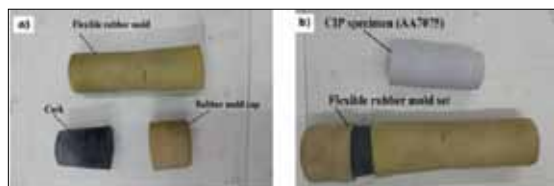


Fig. 9 a. Rubber mold used for Cold Isostatic Pressing
b. CIP specimen

Only pure AA 7075 powder could be compacted by CIP but with carbon fibers CIP was not possible due to fragile nature of compact even at 200 bar pressure. This is due to the absence of cold welding between the powder particles which would yield sufficient green strength. Cold welding was not possible due to the presence of carbon fibers in the mixture and AA 7075 powder is pre-alloyed.

Finally, composite manufacturing was tried by Vacuum Hot Pressing.

Fabrication of the composites by Vacuum Hot pressing was carried out in two major steps.

1. Mixing- To obtain homogeneous powder mixtures containing 5 to 50 volume % of uncoated carbon fibers and AA 7075 powder, laboratory mixer was used. Mixtures were also formed by using Nickel coated carbon fibers up to 30 Vol% and graphite flakes. The mixer was rotated at standard rpm of 20, while the total mixing time was set to 45±5 minutes.

2. Compaction- The hot pressing of the composites was carried using single action and double action press. The homogenous mixture of

MANUFACTURING AND CHARACTERIZATION OF ALUMINIUM METAL MATRIX COMPOSITE

AA 7075 powder and carbon fibers was filled in the high density graphite die and consolidated by hot pressing. At the bottom and top surface of the powder mixture, circular graphite sheet of 0.5 mm thick was placed in order to prevent the adhesion between punch and hot pressed specimen. Fig. 8 a shows tool assembly used.

After that the die-punch-powder assembly was placed into the vacuum chamber, a thermocouple was then attached to the assembly to read out the temperature of the system as well as of graphite die (Fig. 10 a shows Graphite press tool used). Once the required temperature, vacuum and pressure were reached (listed in Table 2), pressing of powder mixture was started, which was maintained during the remainder of the process. After completion of hot pressing, the whole assembly was cooled down to room temperature. Then specimen was removed from the die and the graphite sheets were removed from the hot pressed specimen. The entire hot pressing process for each composition took around 3 hours. Fig. 10 b and c show composites obtained with carbon fibers and graphite flakes as reinforcement respectively.

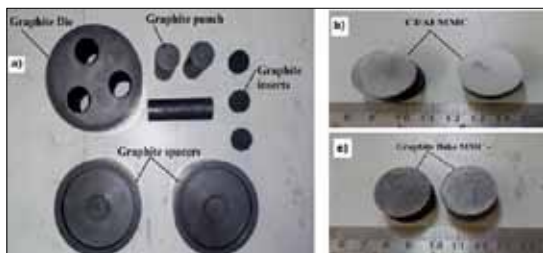


Fig. 10 a. Graphite Press Tool used for hot compaction; b. hot pressed specimens carbon fiber composite with graphite flake as reinforcement.

Table 2. Hot Pressing Parameters

Parameters	Single action press	Double action press
Pressure	35 MPa	50 MPa
Temperature	560 ± 20° C	580 ± 10° C
Vacuum	0.25 bar	1.8 × 10 ⁻³ bar
Pressing Time	30 min	90 min
Heating rate	14° C/min	8° C/min
Cooling rate	10° C/min	12° C/min

C. Results and discussion

Microstructures

After hot pressing, specimens were cut into two pieces along the longitudinal and perpendicular direction of hot pressing, ground and polished for metallographic studies. Microstructures were examined using optical microscope and Zeiss scanning electron microscope (SEM) equipped with EDS facility. Optical micrographs of longitudinal section of composites with 5 to 30 vol.% (Fig. 11 a-e) and 40, 50 vol.% carbon fibers (Fig. 11 g, h) respectively, reveal dark dots representing cross section of carbon fibers. In all the composites distribution of carbon fibers seems to be uniform. Pores are not visible indicating fully densified composite.

Fig. 12 shows SEM images of longitudinal section of composites, containing 10 to 30 (a-f), 40 (g) and 50 vol.% (h) of carbon fibers.

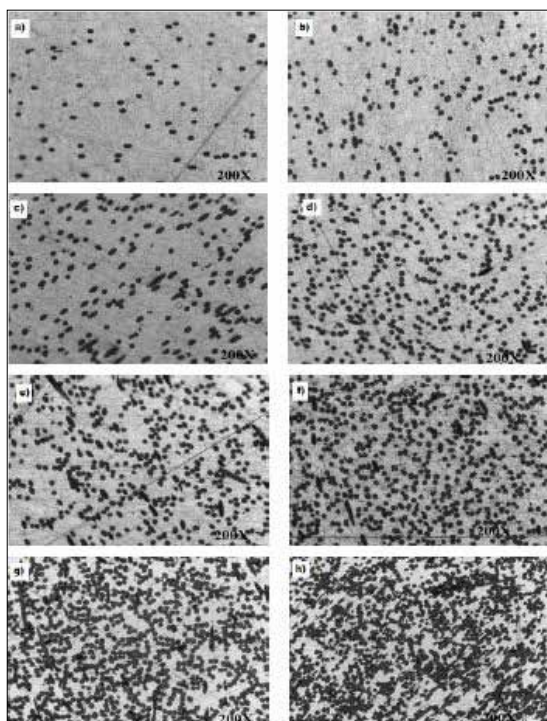


Fig. 12 SEM micrographs of (longitudinal section) 5-30 Vol% CF (a to e), 40 and 50 Vol% CF MMC (g and h)

MANUFACTURING AND CHARACTERIZATION OF ALUMINIUM METAL MATRIX COMPOSITE

In these images also carbon fibers are seen as black dots, but in composites having higher carbon fiber content, significant amount of fibers is seen which are not aligned in the direction perpendicular to pressing. In all the composites, no significant distortion of carbon fibers is seen.

Carbon fibers are seen perpendicular to the pressing direction in perpendicular section due to the strains and stresses imposed by pressing conditions and geometry (Fig. 13). It can be expected that carbon fiber orientation leads to anisotropic properties of these composites.

The fractured cross-section of the consolidated Al/CF composite was investigated with SEM for the 15 vol.% carbon fiber reinforcement. Fig. 14 presents images of the fractured cross-sections of 15 vol.% CF composite; fracture surface appeared as pure brittle. Although some fiber pullout and fiber damage is observed, the carbon fiber/Aluminium shows good bonding between them.

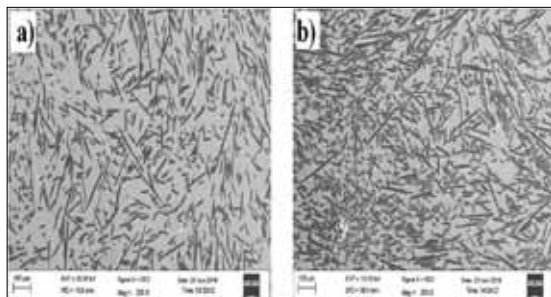


Fig. 13 SEM images of 30 (a) and 40 (b) Vol% CF composite (perpendicular section)

All SEM images reveal that the distribution of carbon fibers in the Al matrix to be uniform even with higher volume fraction of carbon fibers. However, there is no significant distortion in carbon fiber after hot pressing. Also the size and shape of these fibers is almost identical as it is in as processed condition.

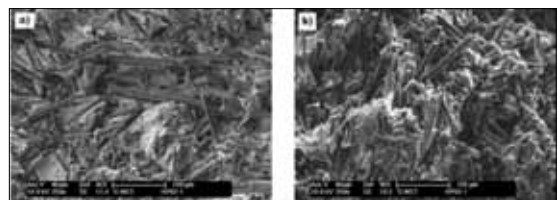


Fig. 14 Fractographic SEM images of 15 Vol% CF composite a and b.

Fig. 15 (a and b) represents SEM images of perpendicular section of graphite flake composite containing 30 vol. % of graphite flakes. Almost all the flakes orient perpendicular to the pressing direction as evidenced from Fig. 15 (a). Graphite flakes also show good bonding with AA 7075 matrix. (Fig. 15 b)

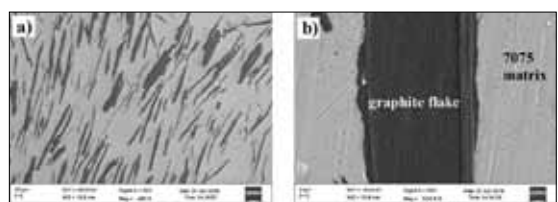


Fig. 15 a and b SEM images of perpendicular section of graphite flake reinforced (30 vol%) MMC

Nickel coated carbon fiber reinforced (15 vol. %) composite's SEM images are given in Fig. 16 (a, b). In both these images, most of the carbon fibers are seen to be oriented in one direction. Bright Nickel coating surrounds the fibers, which is fairly uniform. Fibers are seen to be properly bonded with the matrix. Nickel coating though improves wettability of carbon fibers, but in the current work, we could not make composite by Stir casting using Nickel coated fibers.

Al_4C_3 formation is likely to occur at the interface of carbon fiber and aluminium matrix. This phase is detrimental to properties of composite particularly thermal conductivity. Possibility of its formation increases as amount of carbon fiber content increases. To verify whether Al_4C_3 has formed or not, Specimen of 30 and 40 Vol% CF were analyzed by Transmission Electron

MANUFACTURING AND CHARACTERIZATION OF ALUMINIUM METAL MATRIX COMPOSITE

Microscope(TEM) and XRD. Thin section specimen of 30 and 40 vol% CF was analyzed with the help of TEM (Philips, CM 200) using Energy Dispersive X-Ray Spectroscopy (EDX) at 200 kV. Fig. 15 a shows TEM micrographs of 30 vol.% CF MMC having intimate contact between CF and Al matrix. Al_4C_3 formation is not observed.

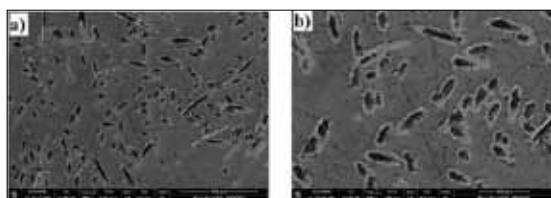


Fig. 16 a and b SEM images of transverse section of Ni coated carbon fiber reinforced MMC.

Fig. 17 a shows TEM image of 40 vol % CF MMC. The interface of carbon fiber and matrix is seen without any presence of Al_4C_3 . Fig. 17 b also shows TEM image of 40 vol % CF MMC in which rod like precipitates about 1 μm long and up to 100 nm thick were observed. These precipitates were analyzed by means of EDX (Fig. 18). From EDX analysis, it was revealed that bigger rods were composed of magnesium, zinc, aluminium and copper.

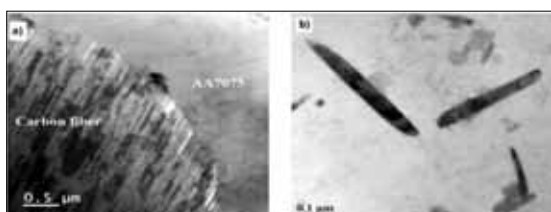


Fig. 17 a and b TEM analysis of 30 and 40 Vol% CF composites, bright phase shows matrix.

XRD analysis was carried out to know the possible reaction products in the composite. Intensity peaks in the XRD plot (Fig. 19) indicate presence of Aluminium, Carbon and small traces of Al_2O_3 . Due to the low volume fraction of the Al_2O_3 , the peaks of alumina are very small compared to Al and Carbon peaks in the composite.

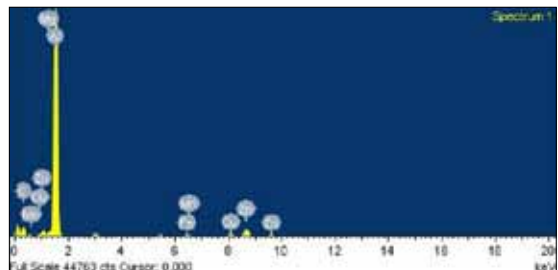


Fig. 18 EDX analysis of thin foil area of matrix rich in precipitates of 40Vol% CF composite

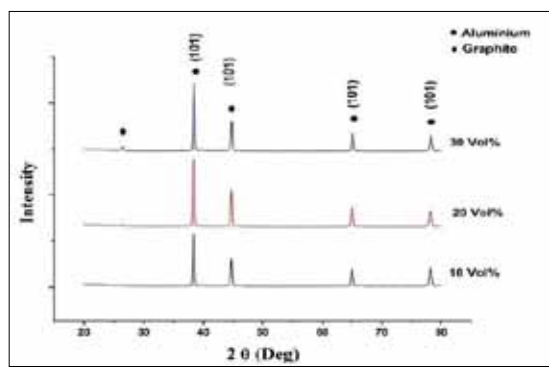


Fig. 19 XRD analysis of 10, 20 and 30 Vol% CF composites

From the XRD and TEM analysis it is confirmed that the interfacial reaction product (Al_4C_3) was not formed.

Major advantages of solid state method are absence of wettability problem, no reaction of carbon fibers with matrix and hence elimination of reaction product, Al_4C_3 which is harmful for thermal properties, no limitation on volume of fiber content and no need for surface modification of carbon fibers.

Densification

The densities of the composites were determined using Archimedes principle. Theoretical density of the composites was calculated using rule of mixtures (ROM). Table 3 shows density results. It follows from the results that as carbon fiber content increased, density dropped due to lighter

MANUFACTURING AND CHARACTERIZATION OF ALUMINIUM METAL MATRIX COMPOSITE

fibers. It is seen that densities obtained from ROM are higher than actual. It is due to inherent porosity of Powder Metallurgy part. Densities are higher in Double action pressing. Fig. 20 shows graphical representation of effect of double and single action pressing on densification. Table 4 shows results of Nickel coated carbon fibers on densities of composites. Due to heavier Nickel coating, these composites exhibit higher density values. In these composites, contrary to uncoated fibers, as amount increased, densities increase.

Table 3. Densities of AA 7075/CF Composites

Content of carbon fibres, Vol%	Density by Rule Of Mixture (ROM) g/cc	Density after Hot pressing (single action) g/cc	Density after Hot pressing (double action) g/cc
0 (Pure 7075)	2.81	2.72	2.76
5	2.78	2.68	2.72
10	2.75	2.64	2.68
15	2.72	2.6	2.64
20	2.69	2.55	2.61
25	2.66	2.51	2.56
30	2.63	2.47	2.52
35	2.60	2.43	2.49
40	2.57	2.37	2.44
45	2.54	2.33	2.40
50	2.51	2.29	2.37

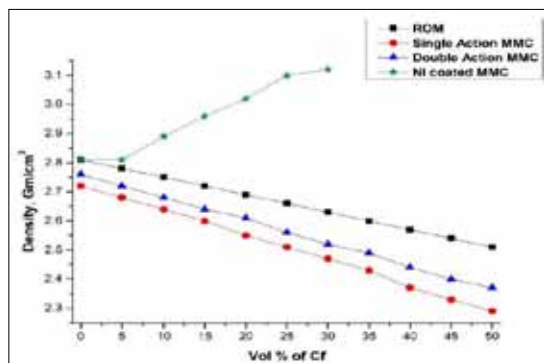


Fig. 20 Effect of densification of Al/CF composite by single action and double action pressing

Effect of Nickel coating on densification is given in Table 4. Higher densities are obtained in composites that containing Nickel coated fibers. This is attributed to higher density of Nickel.

Table 4. Densities of AA 7075/Ni coated Carbon fiber composites

Sr. No.	Vol% of Ni coated CF	Density by ROM, gm/cc	Density after Hot pressing, gm/cc
1	5	2.92	2.81
2	10	3.02	2.89
3	15	3.13	2.96
4	20	3.24	3.02
5	25	3.35	3.10
6	30	3.45	3.11

Hardness

The mechanical property of composites was evaluated by hardness test. For Brinell hardness measurements, the samples were polished and made flat and smooth. A minimum of 6 readings were taken on each specimen. Brinell hardness of the composites was measured using 31.25 kg load and 2.5 mm diameter ball indenter. Table 5 shows Hardness results. As uncoated fiber content increased, hardness decreased in single and double action pressing due to drop in metallic matrix content. But composites with Nickel coated carbon fibers showed higher hardness than that with uncoated CF. Hardness increases as amount of Nickel coated fibers increased up to 20 vol.%, after that drop is observed. This increase in hardness is due to the formation of hard Al_3Ni precipitates during processing of composites. Al_3Ni precipitates lead to strengthening of composite [4,14]. Drop in hardness in composites with higher contents of Nickel coated fiber, may be due to possible porosity due to higher fiber contents. However, in the current study this investigation was not done.

Fig. 21 represents variation in hardness with coated and uncoated carbon fibers as obtained by double and single action pressing.

MANUFACTURING AND CHARACTERIZATION OF ALUMINIUM METAL MATRIX COMPOSITE

Table 5. Hardness of CF/AA 7075 Composites

Vol. % of carbon fibers	Hardness (uncoated fibers) BHN	Hardness, (Nickel coated fibers) BHN
0 (Pure 7075)	101	101
5	102	116
10	97	124
15	80	130
20	73	139
25	68	134
30	63	127
40	58	-
50	46	-

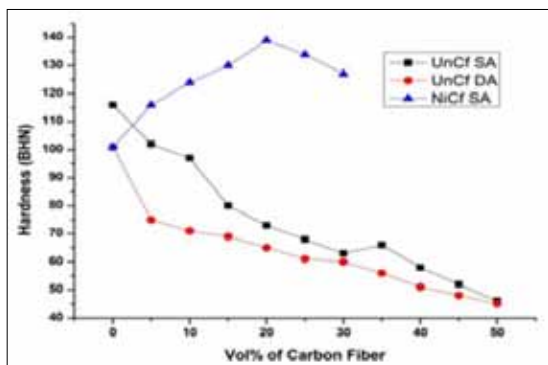


Fig. 21 Effect of vol.% of uncoated and Ni coated carbon fibers, single and double action pressing on hardness of composites.

Authors had studied thermal properties of these composites and the results were published in previous work [15].

Conclusions

1. Metal matrix composite in which milled Carbon fibers are used as reinforcement, could not be produced by simpler Liquid Metallurgy route as even with rigorous stirring, uniform distribution of carbon fibers was difficult to achieve. This is mainly due to poor wettability of carbon fibers.
2. Coating of carbon fibers is necessary to improve wettability, for better bonding with matrix, to avoid formation of brittle Aluminium carbide phase at the interface of Aluminium and carbon fiber and for uniform distribution of carbon fibers.

3. Even with Nickel coated carbon fibers, uniform distribution of carbon fibers could not be obtained.
4. Aluminium powder could be compacted by Cold-Iso static pressing but when carbon fibers were added, pressing was not possible due to fragile nature of composite.
5. Among the various methods of composite manufacturing which were tried, *Powder Metallurgy* is the best method which yielded uniform distribution of carbon fibers as well as flakes and good bonding with the matrix.
6. Powder Metallurgy being a Solid state method, Al_4C_3 did not form at the interface of carbon fiber and matrix.
7. Double action compaction showed higher densification.
8. Composites show decrease in densification and hardness as carbon fiber content increased. Nickel coated carbon fibers increased densification.
9. Composites with Nickel coated carbon fibers exhibited higher hardness.
10. Hardness of composites containing Nickel coated fibers increased as volume content of fibers increased up to 20.

Acknowledgement

Authors gratefully acknowledge the financial support of this work given by ISRO-UoP Space Technology cell and Bhabha Atomic Research Center, Vashi complex, for providing their double action hot pressing facility.

References

1. D.D.L Chung, "Materials for thermal conduction", *Applied thermal engineering*, 21 (2001), 1593-1605.
2. J. Korab, Sebo P, Stefanik P, Kavecky S, Korb, "Thermal conductivity of continuous carbon fiber reinforced Copper matrix composite", ICCE12 - 12th International Conference on Composite Materials, At Paris, France, July 1999.

MANUFACTURING AND CHARACTERIZATION OF ALUMINIUM METAL MATRIX COMPOSITE

3. B. Bhav Singh, M. Balasubramanian, "Processing and properties of copper-coated carbon fiber reinforced aluminium alloy composites", *Journal of Materials Processing technology*, 209 (2009), 2104-2110.
4. Junjia Zang, Shichao Liu, Yingxin Zhang, Yong Dong, Yiping Lu, Tingju Li, "Fabrication and bending properties of carbon fibers reinforced Al-alloys matrix composites", *Journal of Materials Processing technology*, 231 (2016), 366-373.
5. Qiurong Yang, Jinxu Liu, Shukui Li, Fuchi Wang, Tengteng Wu, "Fabrication and mechanical properties of cu-coated woven carbon fibers reinforced aluminium alloy composite", *Materials and Design*, 57 (2014), 442-448.
6. Moonhee Lee, Yongbum Choi, Kenjiro Sugio, Kazuhiro Matsugi, Gen Sasaki, "Effect of Aluminium Carbide on unidirectional Cf-Al Composites fabricated by low pressure infiltration process", *Composites Sciences and Technology*, 97 (2014) 1-5.
7. Jean Frank Silvain, Amelie Veillere, Yongfeng Lu, "Copper-Carbon and Aluminum-Carbon Composites Fabricated by Powder Metallurgy Processes", *Journal of Physics: Conference Series*, 525 (2014).
8. H. Chen, A. T. Alpas, "Wear of Aluminium matrix composite reinforced with nickel coated carbon fibers", *Wear*, 192 (1996), 186-198.
9. T. Shalu, E. Abhilash, A. Joseph, "Development and characterization of liquid carbon fiber reinforced aluminium matrix composite", *Journal of Materials Processing Technology*, 209 (2009) 4809-4813.
10. E. Simancik, G. Jangg, H. Degischer "Short carbon fibers-aluminium matrix composite material prepared by extrusion of powder mixtures", *Journal de Physique IV*, 03-C 7, (1993) 1775-1780.
11. M. Sanchez, J. Rams, a. Urena, "Fabrication of Aluminium composites reinforced with carbon fibers by centrifugal infiltration process", *Composites Part A*, 41 (2010) 1605-1611.
12. Xiong Cao, Qingyu Shi, Dameng Liu, Zhili Feng, Qu Liu, Gaoqiang Chen, "Fabrication of in situ carbon fiber/aluminum composites via friction stir processing, Evaluation of microstructural, mechanical and tribological behaviors", *Composites Part B: Engineering Volume*, 139 (2018) 97-105.
13. Madhuri Deshpande, R.A. Waikar, R. Gondil, S.V.S. Narayan Murty, "Effect of Coating Parameters on Coating Rate of Carbon Fibers by Electro less Nickel Plating", *Materials Science Forum*, Vols. 830-831, (2015), 635-638.
14. Hsiao Yeh Chu, Jen Fin Lin, "Experimental analysis of the tribological behavior of electro less nickel-coated graphite particles in aluminium matrix composites under reciprocating motion", *Wear*, 239 (2000) 126-142.
15. Madhuri Deshpande, Ramesh Gondil, S. V. S. Narayan Murty, R. K. Kalal, "Studies on 7075 Aluminium Alloy MMCs with Milled Carbon Fibers as Reinforcements", *Transactions of the Indian Institute of Metals*, Volume 71, Issue 4, (2018) 993-1002.

FRICITION PROPERTIES OF SINTERED Al BRONZE CONTAINING DISPERSED SULFIDES

Tomohiro SATO^{1*}, Akihiro JINGU², Ken-ichi SAITO¹, Masanori TAKUMA¹, Yoshimasa TAKAHASHI¹

¹ Kansai University Department of Mechanical Engineering, Japan

² Kansai University Graduate School of Science and Engineering (currently NTN corporation), Osaka, Japan

1. Introduction

The Al-bronze has the highest strength and high corrosion resistance in the copper alloy, in particular, sintered at hydrogen atmosphere [1]. It was thought that these qualities can adapt to bearing for fuel pumps, in which Cu-Ni alloy is typically used. However, Ni is expensive and corrosion resistance of Cu-Ni alloy is insufficient when used with gasoline of inferior quality. On the other hand, corrosion resistance of Al bronze is available. However, the friction properties of Al-bronze are inferior. By the way the vacuum sintering is suitable for basic materials research. So friction properties were evaluated for sulfide Al bronze in this research.

2. Procedure

The chemical composition of each specimen is shown in Table 1. Al Bronze was mixed copper powders and aluminum powders with copper nickel alloy powders. In the binary system of mixed powders of Cu-Al, the eutectic melt is eutectic at around eutectic temperature of 548°C. It appears and expands due to heat based on γ_2 (Cu_9Al_4) formation. This expansion remained in the sintering history and the strength decreased. In order to prevent this expansion, it is possible to add Ni powders [2]. Al Bronze 2 contained copper powder and Aluminum powder that did not contain nickel or sulfur. Sulfide Al Bronze adds sulfides to Al Bronze. The number(index) 63 and 25 written next to Sulfide Al Bronze mean the particle size (μm) of sulfides, and 1 and 5 mean the content (mass%). By the way, the particle size of sulfide dispersed in Sulfide Al Bronze 1, 5 is the one having a size of 45 μm or less was used.

Table 1 Characteristic of the specimen

Material	mass%
Al Bronze	Cu - 8.5 Al - 4 Ni (< 0.004 S)
Sulfide Al Bronze 63	Cu - 8.5 Al - 4 Ni - 1 Cu ₅ FeS ₄
Sulfide Al Bronze 25	Cu - 8.5 Al - 4 Ni - 1 Cu ₅ FeS ₄
Al Bronze2	Cu - 8.5 Al - 0.01 CaF ₂
Sulfide Al Bronze 1	Cu - 8.5 Al - 4 Ni - 1 Cu ₅ FeS ₄ - 0.01 CaF ₂
Sulfide Al Bronze 5	Cu - 8.5 Al - 4 Ni - 5 Cu ₅ FeS ₄ - 0.01 CaF ₂

Calcium fluoride (CaF₂) was contained in small amounts for removal of alumina^[3]. Calcium fluoride was also known as a cubic crystal lubricant ^[4]. These powders were molded at 250 MPa, then, each green bodies was vacuum sintered at 920 ° C. Friction properties were also evaluated by using 3 pin on disk apparatus shown in Fig.1.

Table 2 shows the conditions of the friction test. With the load kept constant at 54 N, the test and the load changed from 46.7 N to 53.9 N after 300 sec. Then load at 61.2 N from 200sec after test started for 1000 m and 122.3 N. After that, load at

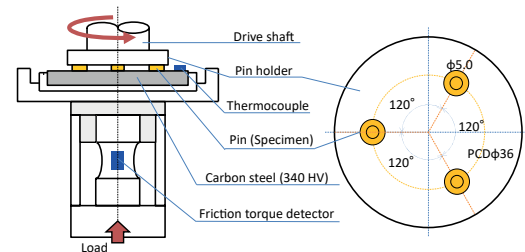


Figure 1: 3 pin on disk apparatus

FRICITION PROPERTIES OF SINTERED Al BRONZE CONTAINING DISPERSED SULFIDES

86.3 N from 780 sec after test started. The friction speed was set at 1.0 m / s, and the friction distance was set at 1000, 1800 m.

The friction environment was dry at room temperature and was under lubricat condition (PAO: Poly- α -olefin).

Table 2 Friction condition

Load	46.7 ~ 122.3 N (step) 54 N (constant)
Rotational speed	1.0 m/s
Sliding distance	1000 ~ 1800 m
Environment	R.T., Dry or Oil (PAO)

3. Results and discussion

3.1 Effect of sulfide size on friction characteristics

SEM/EDS images of specimen surfaces of Al Bronze, Sulfide Al Bronze 63, and Sulfide Al Bronze 25 are shown in Fig.2. Aluminum and oxygen were densely detected at grain boundaries from EDS element mapping image of Al Bronze. It could be alumina (Al_2O_3) which is a compound of aluminum and oxygen. Sulfide Al Bronze 63 and Sulfide Al Bronze 25 did not show the EDS element mapping image of oxygen in this paper, however, oxygen was detected in the area where the aluminum concentration was detected deeply. Sulfide Al Bronze 63 also contains sulfide that the particle size of the sulfide is 63 μm or less. The particle size was larger than that of the copper alloy. It could be also observed that aluminum is distributed densely partially on the sulfide particles. During sintering, aluminum might be formed as a liquid phase and slightly dissolves the sulfide. After that aluminum and aluminum sulfide which is a compound of sulfur were precipitated. In Sulfide Al Bronze 25, sulfides could be confirmed in such a way as to be along the gaps between the grain boundaries. SEM/EDS image of the sulfide is shown in Fig.3.

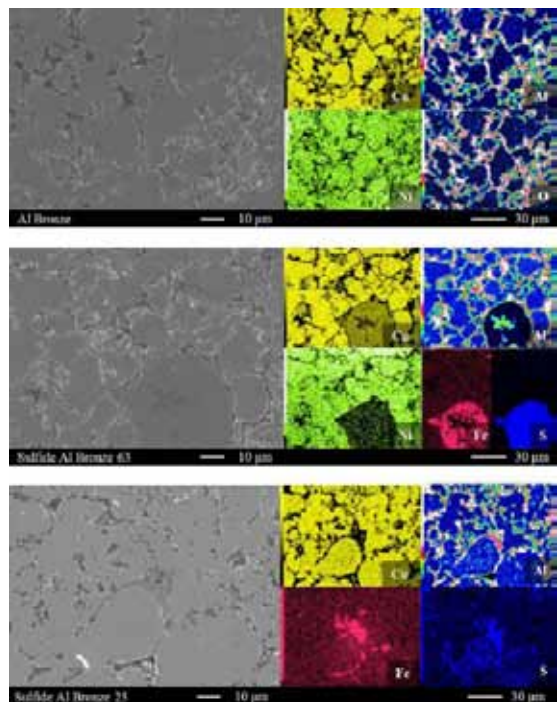


Fig.2 SEM and EDS analysis image of Al Bronze surface

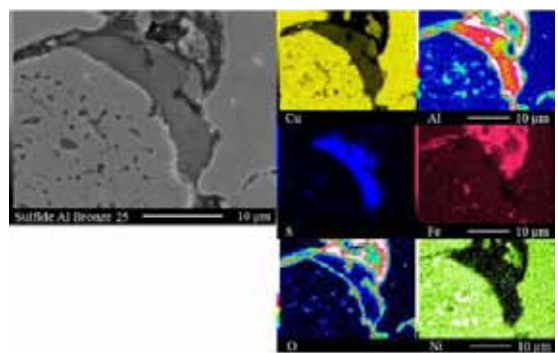


Fig.3 SEM and EDS analysis image of Sulfide

From the images of them, it was possible that the main component is aluminum sulfide, there seemed to be a partial bornite (Cu_5FeS_4) left. As a result, the sulfide is slightly dissolved to make the compound with aluminum during sintering.

FRICITION PROPERTIES OF SINTERED AI BRONZE CONTAINING DISPERSED SULFIDES

Fig. 4 shows the radial crushing strength (RCS) and surface hardness. The plot shows the average value of each RCS and surface hardness. The error bar attached to the plot showed the maximum value and the minimum value. Also, the number shown next to the plot showed the open porosity. Al Bronze has an open porosity of 20.2 % and RCS of about 167 N/mm², Sulfide Al Bronze 63 has an open porosity of 20.7 % and RCS is around 141 N/mm², Sulfide Al Bronze 25 has an open porosity of 16.9 % and RCS of 171 N/mm². From these results, the strength of the aluminum bronze sintered material was insufficient. The annular strength of the bronze sintered material bearing is 190 N/mm² and it did not even satisfy the strength of the bronze sintered material.

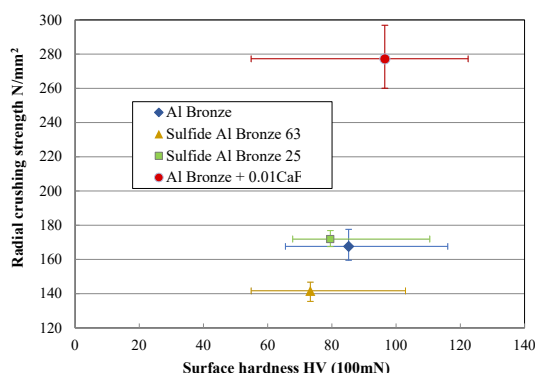


Fig.4 Relationship of the surface hardness and radial crushing strength

The reason is that alumina (Al_2O_3) precipitated at the grain boundary is considered. In Sulfide Al Bronze 63, larger sulfide particle than surrounding particles existed in grain boundaries. As a result, this misfit size and hardness causes break at the interface between the copper alloy matrix and the sulfide.

That is why RCS decreased. On the other hand, Sulfide Al Bronze 25 indicated higher RCS values than that of Al Bronze. This is because the open porosity of Al Bronze 25 was smaller than that of Al Bronze and Sulfide Al Bronze 63.

It is conceivable that the fine sulfide is liable to be cleaved and the formability had been improved. It means that the green body of Al Bronze 25 was denser than the others and RCS was excellent. The highest RCS of specimen showed in Al Bronze + 0.01 CaF₂ which was added to Al Bronze in an amount of 0.01 mass% calcium fluoride that was very chemically stable. However, it reacts with Al_2O_3 at high temperatures [5]. The mechanism of reaction was that the liquid phase of CaF₂ had wetted the grain surface of aluminum bronze. At that time, vaporized F was generated over a system. Then, this vaporized F and Al₂O₃ covered grain surface were reacting and formed AlOF. As a result, brittle Al₂O₃ had disappeared and RCS was improved. In this way, the influence of calcium fluoride could be confirmed.

Fig.5 showed SEM/EDS on the surface of Al Bronze. Particles larger than the surroundings can be confirmed slightly on the upper left from the center. Since EDS element mapping image, nickel is detected and fine sulfur also existed on the particle. It seems that this particle was from copper nickel raw powders. This was because the nickel was not dispersed sufficiently in the specimen and the matrix did not become homogeneous. That made RCS decreased. Fig.6 showed the SEM/EDS of the fractured surface after RCS test of Sulfide Al Bronze 63.

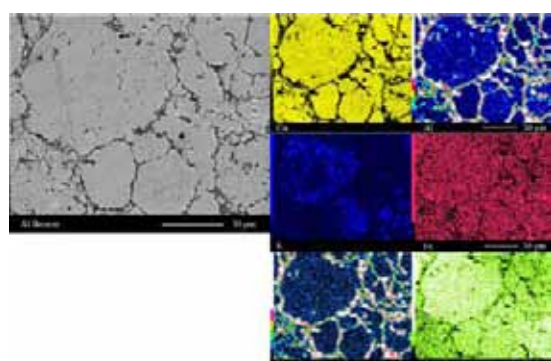


Fig.5 SEM and EDS analysis image of Al Bronze surface

FRICTION PROPERTIES OF SINTERED Al BRONZE CONTAINING DISPERSED SULFIDES

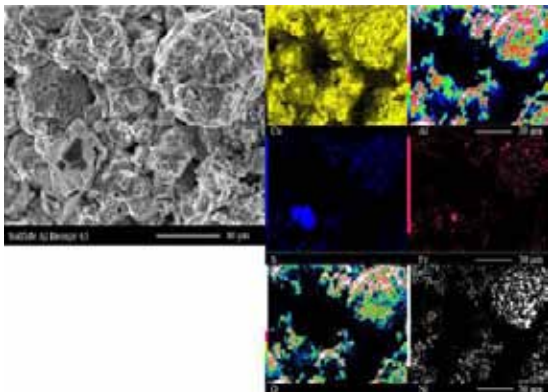


Fig.6 SEM and EDS analysis image of Sulfide Al Bronze 63 fracture surface

From the center of the SEM image, a slightly lower left, the matrix different from the surrounding fracture surface was observed that. From EDS, sulfur is detected and it was a sulfide which was mixed. SEM/EDS image of the sulfide was shown in Fig.7. By fractured surface of the sulfide, it was observed to confirm the river pattern which is characteristic of the brittle fracture surface and it was mainly aluminum sulfide. Fig.8 showed the fracture surface of Sulfide Al Bronze 25. That was not so different with the surface of Sulfide Al Bronze 63. However, sulfide observed with Sulfide Al Bronze 63 could not be confirmed.

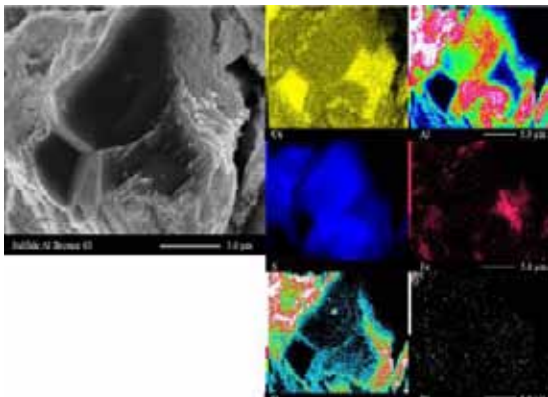


Fig.7 SEM and EDS analysis image of Sulfide Al Bronze 63 fracture surface

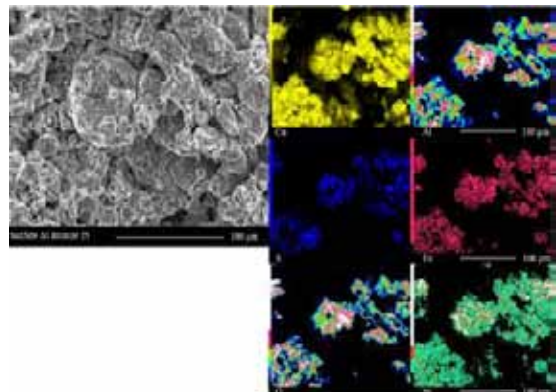


Fig.8 SEM and EDS analysis image of Sulfide Al Bronze 25 fracture surface

Fig. 9 showed SEM/EDS image showing a part of the fractured surface of Sulfide Al Bronze 25. Dimples could be observed on this fractured surface, and that small particles could be also confirmed inside. From the EDS mapping image it was possible that the particles in the dimple are sulfides. Because of the size of the sulfide and the presence within the dimple, sulfur contained in the copper nickel alloy powder were assumed.

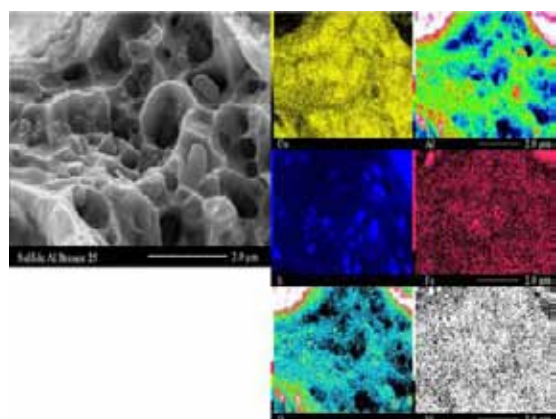


Fig.9 SEM and EDS analysis image of Sulfide Al Bronze 25 fracture surface

Relationship between friction coefficient and sliding distance and the surface temperature of each specimen was shown in Fig.10. For Al

FRICTION PROPERTIES OF SINTERED Al BRONZE CONTAINING DISPERSED SULFIDES

Bronze, near 135 m, stick-slip occurred and kept shaking up to 1000 m. The friction coefficient abruptly decreased from 198 m. The friction coefficient could not be measured around 300 m. As the test continued, the friction coefficient rapidly began to increase and eventually rose to 0.55. This rapid decrease phenomenon of friction coefficient was caused by intense self-excited vibration by stick-slip. It was considered that the friction torque could not be detected successfully. By continued as it is, the self-excited vibration surface was slightly attenuated due to peeling and improvement, so measurement of friction torque was gradually possible.

For Sulfide Al Bronze 63, running-in occurred around 200 m, after that the friction coefficient gradually decreased. Eventually it fell to 0.25.

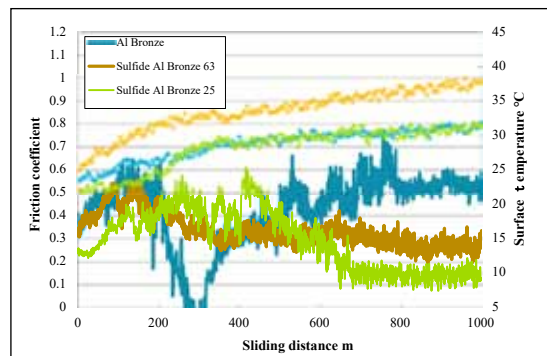


Fig.10 Friction performances under dry lubrication

For Sulfide Al Bronze 25, stick-slip had occurred from 340 m to 1000 m. Eventually it decreased to about 0.17, but it took up to 600 m until the friction coefficient decreased and stabilized.

By observing at the temperature change during friction of the S45C (carbon steel) disc, mating steel for Al Bronze and Sulfide Al Bronze 25 eventually had reached at 31.6°C, Sulfide Al Bronze 63 had heated slightly to 37.8°C. This difference was related to the presence or absence of stick-slip. Self-excited vibration by stick-slip was due to the specimen (pin) and mating material (S45C disc).

The contact with each other became continuous to intermittent. In other words, it was thought that air entered between the pin and the disc and it was cooled down.

The other reason was a thermocouple which measured the temperature of the disc is stripped from the disc surface by violent self-excited vibration.

Surface analysis of the sliding surface and not sliding surface (before test) of Sulfide Al Bronze 25 by XPS was shown in Fig.11.

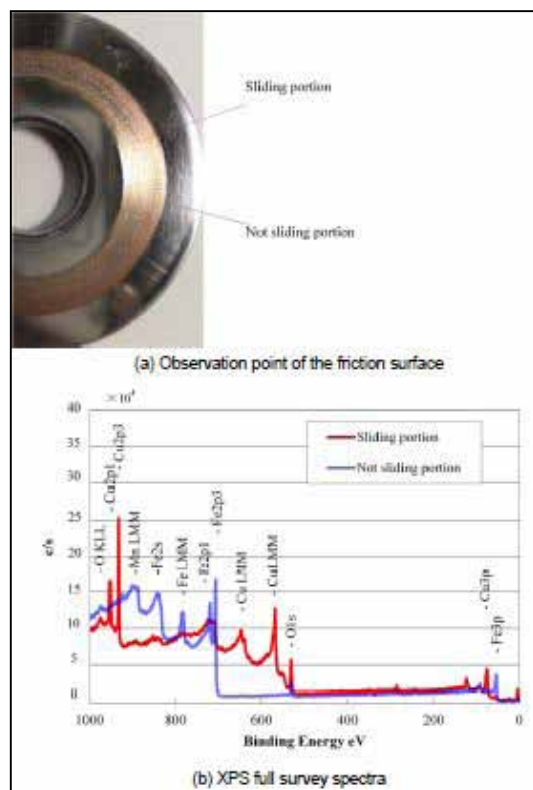


Fig.11 Surface observation by XPS

On the not sliding surface, the Fe peak appeared, whereas the peak was not observed on the sliding surface, and the Cu based peak was confirmed. It could be seen that the copper alloys

FRICTION PROPERTIES OF SINTERED Al BRONZE CONTAINING DISPERSED SULFIDES

adhered to the friction tracks. In addition, for the peak of each element on the sliding surface, shape analysis and analyzed was conducted in more detail. The results were shown in Fig.12. In Cu system, mainly CuO was observed and Cu₂O might be contained in a small amount. The peak of O was confirmed mainly by copper oxide such as Cu₂O. There was a possibility that Al₂O₃ was also included.

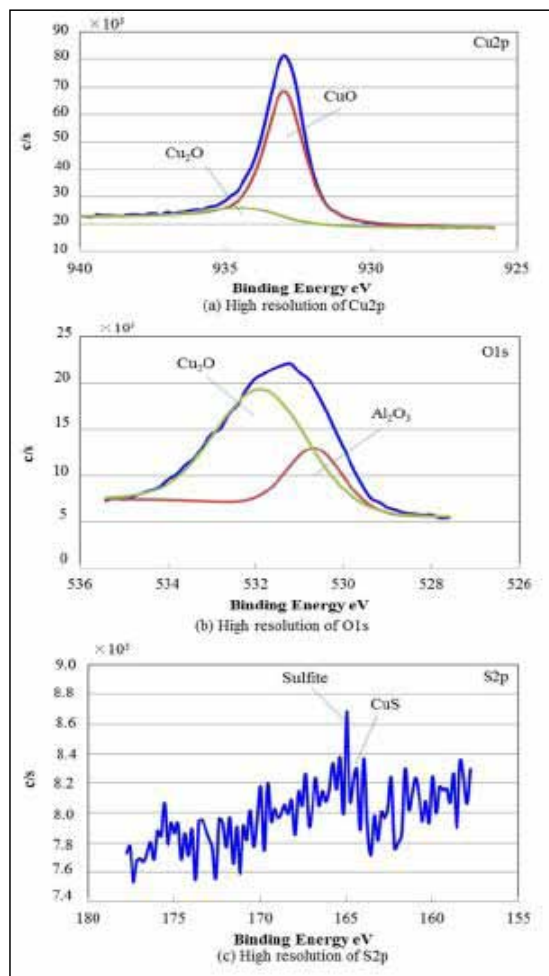


Fig.12 High resolution spectra of each element

Because S was contained in a very small amount, analyze the waveform separation was high from the binding energy value near the peak. Although it could not be analyzed, It was found, CuS, the possibility of sulfuric acid system (Sulfite) [6]. From these results, by dispersing sulfide in aluminum bronze, it was found that an oxide film derived from a sulfide was formed.

Fig. 13 showed the analysis results of the sliding surface in the depth direction. Aluminum had the higher content, not copper on the top of the surface except the oxygen. Alumina might be transferred on the surface. In addition, the aluminum content decreased as it proceeds in the depth direction in Fig.13. As the content of iron increased, it could be inferred that the transfer film was not so thick.

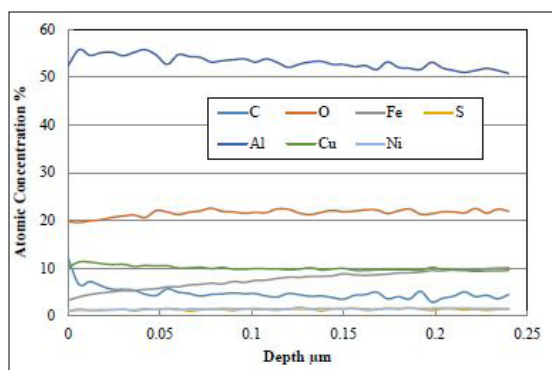


Fig.13 Depth direction analysis

3.2 Influence of sulfide content on friction characteristics

Fig.14 showed optical microscopic images of the surfaces of the test pieces of Al Bronze 2, Sulfide Al Bronze 1 and Sulfide Al Bronze 5.

Black images could be observed on the surface of each specimen, which were pores. Observed gray images as grains in the specimen were dispersed sulfides.

FRICITION PROPERTIES OF SINTERED Al BRONZE CONTAINING DISPERSED SULFIDES

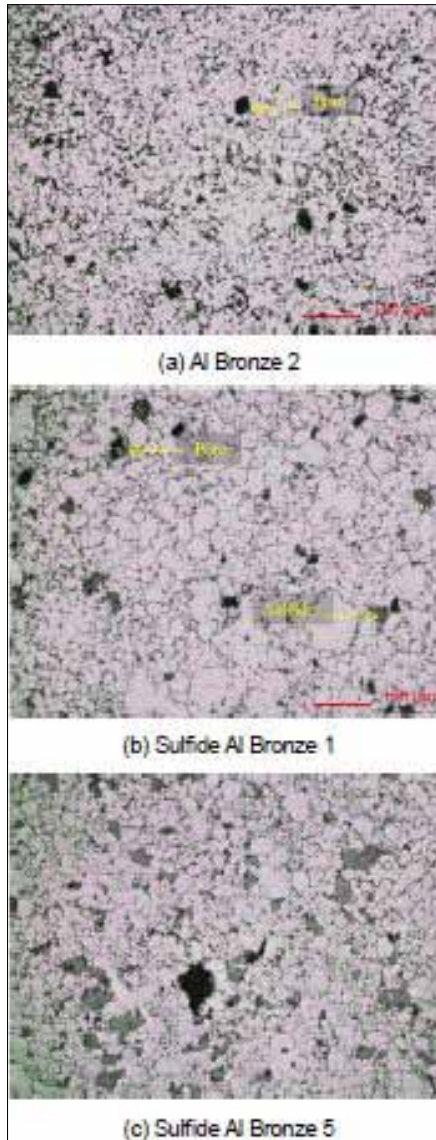


Fig.14 Optical microscope image of the specimen surface

Fig.15 showed the results of RCS and surface hardness. The plot showed the average value of RCS and surface hardness, the bars showed the maximum value and the minimum value and the number indicated by the plot was open porosity.

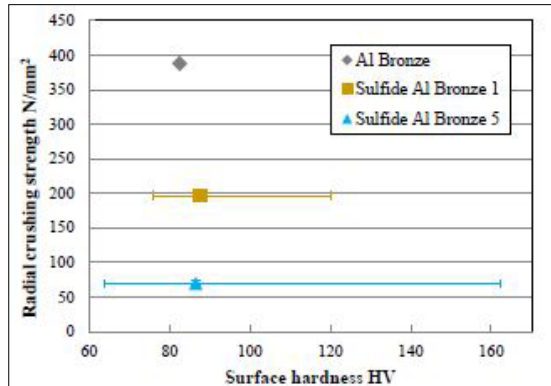


Fig.15 Relationship of the open porosity and radial crushing strength

The RCS of Al Bronze 2 was the highest at 388 N/mm². The RCS of Sulfide Al Bronze was rather inferior. It was possible that sulfide precipitated at the grain boundary and became the starting point of fracture [7]. In addition, nickel segregation occurred by mixing the copper-nickel alloy powder, the matrix did not become homogeneous, resulting the strength decreased. Sulfide Al Bronze 1 had better RCS than that of Sulfide Al Bronze 5. This was because the open porosity of Sulfide Al Bronze 1 was lower and because Al Bronze 5 contained a lot of sulfides that made strength decreased. In addition, contained sulfides had become partly sulfide aluminum as shown in Fig.16 after sintering process. There was a possibility that sulfurized corrosion occurred by this sulfides [8].

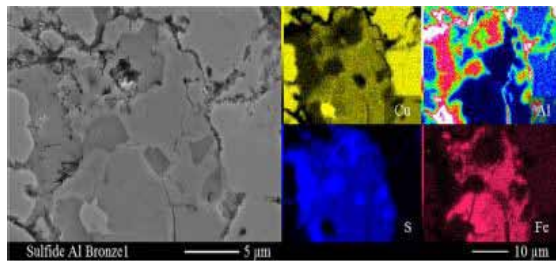


Fig.16 SEM and EDS analysis image of sulfide on specimen

FRICTION PROPERTIES OF SINTERED Al BRONZE CONTAINING DISPERSED SULFIDES

Fig.17 showed the relationship between friction coefficient, distance and load. In Al Bronze 2, a stick-slip occurred from around 109 m and finally the friction coefficient sharply increased at 748 m, so it was judged as seizing and the test was stopped. In contrast, by sulfide dispersed, it was able to continue the test up to the target distance of 1000 m. Even though the friction coefficient increased for Sulfide Al Bronze 1 at 300 m and 748m, the friction coefficient decreased and stabilized without causing stick-slip. In Sulfide Al Bronze 5, stick-slip occurred around 140 m and continued to the end. Finally, the lowest friction coefficient was obtained in this specimen. It seemed that the friction state was unstable when considering occurrence of stick-slip.

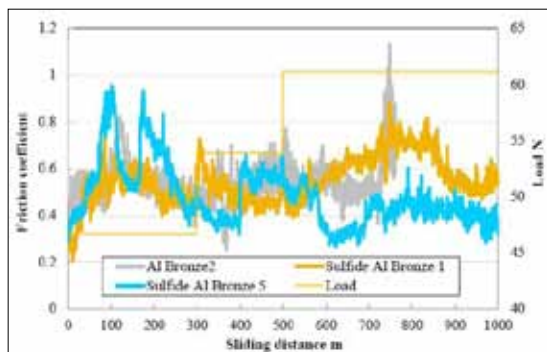


Fig.17 Friction performances under dry lubrication

Fig.18 showed SEM images of abrasion powder collected after each test. Comparing each abrasion powder, wear of Al Bronze 2 powder was the largest. This was because adhesion occurred between friction surfaces, it was torn by shear force, growing as transfer grains. Wear debris of Sulfide Al Bronze 1 were finer than Al Bronze 2. It was because of sulfide better machinability. Sulfide was dispersed in free-cutting steel to improve machinability [9]. Dispersed sulfide worked as a starting point of micro crack generation and it was thought that it became finer than the abrasion powder of Al Bronze 2. Sulfide Al Bronze 5 wear particle

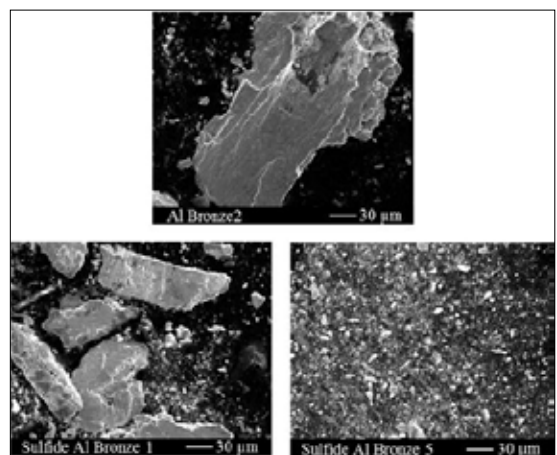


Fig.18 SEM image of wear

was finest. Because it contained a large amount of sulfide, the sulfide showed the ability of the free-cutting property. In addition, a part of bornite mixed as a sulfide might change as aluminum sulfide during a sintering process. This aluminum sulfide was very hard, and the mating material S45C (carbon steel) disc was damaged [10].

Fig.19 showed SEM/EDS images of abrasion powder of Sulfide Al Bronze 5. Iron was also detected in fine powder.

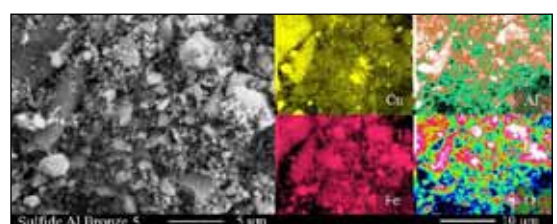


Fig.19 SEM and EDS analysis image of Sulfide Al Bronze 5 wear

SEM/EDS images of Al Bronze 2 surface after friction test in Fig. 20. Iron seemed to be stuck to the surface. It might be a evidence of stick-slip occurrence. SEM / EDS images of the surface of Sulfide Al Bronze 1 after friction test were shown in Fig 21. In this figure, it is difficult to observe iron adhesion particles on a friction

FRICITION PROPERTIES OF SINTERED Al BRONZE CONTAINING DISPERSED SULFIDES

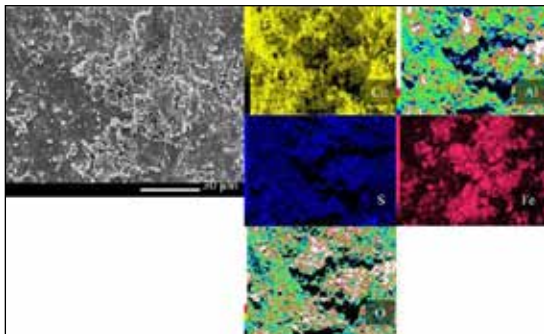


Fig.20 SEM and EDS analysis image of Al Bronze2 surface after the friction test

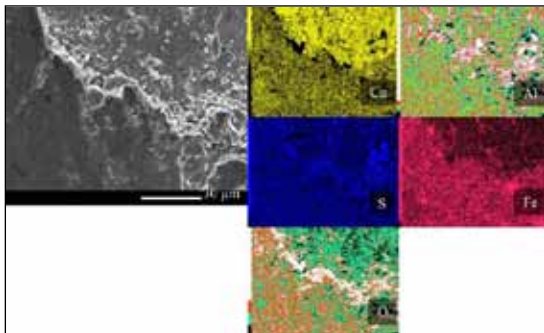


Fig.21 SEM and EDS analysis image of Sulfide Al Bronze 1 surface after the friction test

surface. On the other hand, Iron was detected entirely from the EDS element mapping image. It seemed surface partially peeled off. It was conceivable that the surface was peeled off when the transferred particles detached. There was not much observation at the peeled part, mostly it was a smooth friction surface.

Fig. 22 showed SEM/EDS image Sulfide Al Bronze 5 surface. The surface of Sulfide Al Bronze 5 was very different from other friction surfaces of specimens. It was thought that the surface was struck against the mating S45C by violent self-excited vibration. As a result, it was understood that iron was stuck on the surface from the EDS mapping image. Sulfur and aluminum were

detected at the same point. So, it was considered that it was aluminum sulfide.

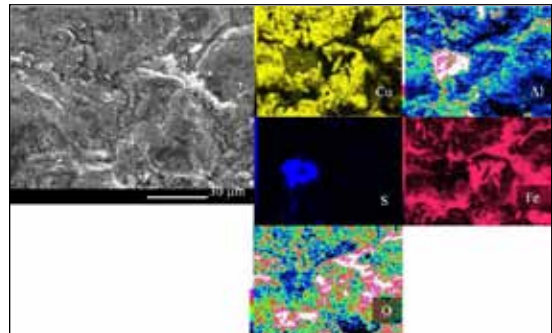


Fig.22 SEM and EDS analysis image of Sulfide Al Bronze 5 surface after the friction test

Fig.23 showed the optical microscope and SEM/EDS image of S45C (carbon steel) disc after the friction test.

It was observed that the copper alloy was adhered to the sliding mark in Al Bronze 2 test. From the optical microscopic image the sticking object seemed a thick material. It might be made results of severe wear of adhesive wear.

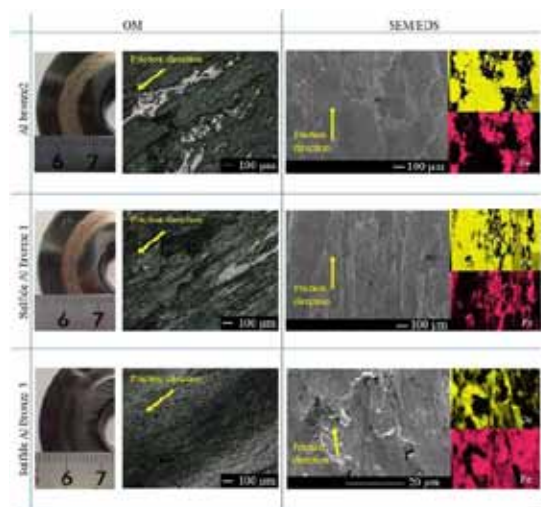


Fig.23 Optical microscope, SEM and EDS analysis image of S45C disk surface after the friction test

FRICITION PROPERTIES OF SINTERED Al BRONZE CONTAINING DISPERSED SULFIDES

Copper alloy had been also transferred to the mating disc of Sulfide Al Bronze 1. Adhesion was thin and smooth from the optical microscope image. It was mild wear of adhesion wear. It was also inferred that this leaded to high lubricity as a tribo coating.

On the sliding mark of Sulfide Al Bronze 5, almost no transfer could be confirmed, and fine scratches were attached. SEM/EDS images showed a small amount of transferred substances.

In Sulfide Al Bronze 5, the bornite contained as a sulfide became hard aluminum sulfide. It could be inferred that the film formation was inhibited. For that reason, it seemed that the friction state was not stable due to stick-slip occurring during the friction test.

3.3 Behavior of sulfide in friction under lubricant

Fig.24 showed the results of friction test under lubricant. In order to reproduce the boundary lubrication region, PAO (poly- α -olefin) which had a low viscosity was dropped on the S45C disc (about 0.014 to 0.018 g) and thinly spread.

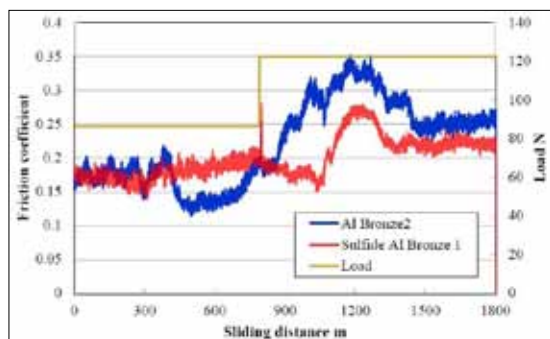


Fig.24 Friction performances under oil lubrication

Therefore, even though it was under the lubricant condition, the friction coefficient was 0.15 or more. In the test of Al Bronze 2, friction coefficient decreased to 0.14 in 370 m. It was because lubricant was supplied to the friction

surface from the open pores to the sliding grooves during the test. After that, friction coefficient gradually rose. In addition, even after the increase in load, the rise of friction coefficient had continued. At that time, sound that could be scraped off from the sliding distance 1140 m and the friction coefficient increased to 0.34. Then, the friction surface became running-in state, and the friction coefficient began to decrease. At sliding distance in 1308m, stick-slip occurred, and finally the friction coefficient calmed down to 0.25. On the other hand, in Sulfide Al Bronze 1, friction coefficient did not change greatly until the load was increased. After increasing the load, the friction coefficient decreased until sliding distance reached 1032 m. This was because oil film breakage occurred by rapidly increasing the load, and the sulfide worked as a solid lubricant. After that, the friction coefficient sharply increased to 0.27 similarly to Bronze 2, but stick-slip did not occur. The friction coefficient was reduced and stabilized to 0.22. As a result, the gap of the friction coefficient was able to be reduced by dispersing sulfide nevertheless oil film breakage.

Fig.25 showed the results of surface analysis of non-sliding (raw) surface and the sliding surfaces of Al Bronze 2 and Sulfide Al Bronze 1 by XPS. On the non-sliding surface, the peak of the Fe type appeared, whereas the Cu peak was not observed on both sliding surfaces. From the result it could be seen that the copper type

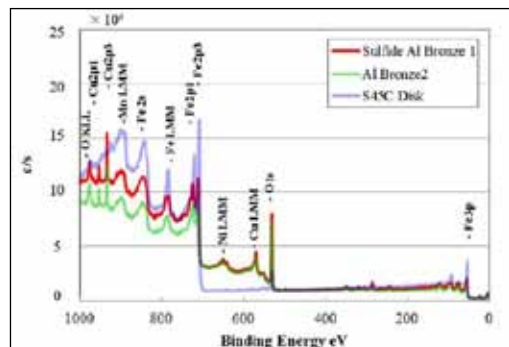


Fig.25 XPS full survey spectra

FRICTION PROPERTIES OF SINTERED AI BRONZE CONTAINING DISPERSED SULFIDES

adhered to the friction marks. Al Bronze 2 and Sulfide Al had indicate that they had the same detected peaks. Results of Sulfide Al Bronze 1 had a higher detection intensity. It seemed that a thick coating film was formed in Sulfide Al bronze 1. In addition, waveform separation analysis was performed on the peak of each element on the sliding surface, and in more detail analysis was carried out. The results were shown in Fig. 26, 27.

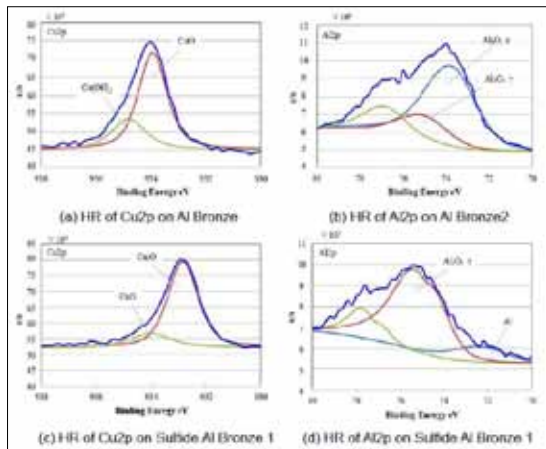


Fig.26 High resolution(HR) spectra of each specimen

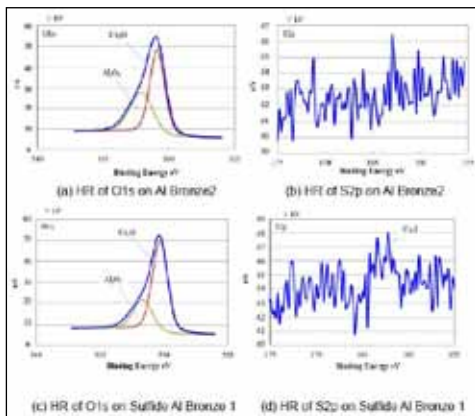


Fig.27 High resolution(HR) spectra of each specimen

On the peak of Cu, the energy peak differs with Al Bronze 2 and Sulfide Al Bronze 1. This was because the difference in chemical state,

Al Bronze 2 is mainly composed of CuO and Cu(OH)₂. In contrast, Cu₂O and CuO were detected in Sulfide Al Bronze 1. On the peak of Al, Al₂O₃ were observed in both specimens.

Al Bronze 2 had a higher detection intensity than Sulfide Al Bronze 1. It was considered that alumina had adhered to the sliding surface, and this hard adherent caused stick-slip. On the peak of O, Cu₂O and Al₂O₃ were detected in both cases. Because S content was very small, although the waveform separation was difficult, there was a possibility that Cu₂S was detected from the peak value.

In addition, the analysis results in the depth direction were shown in Fig. 28.

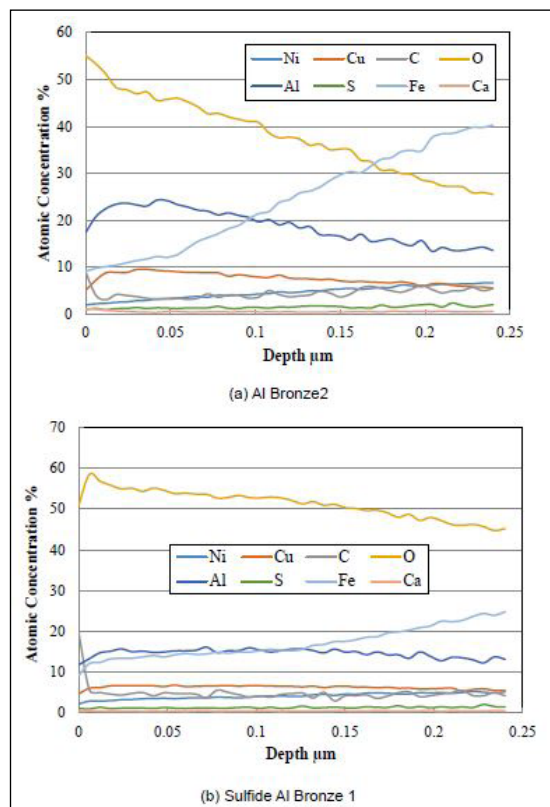


Fig.28 Depth direction analysis

FRICITION PROPERTIES OF SINTERED Al BRONZE CONTAINING DISPERSED SULFIDES

The difference between Al Bronze 2 and Sulfide Al Bronze 1 was oxygen content. Oxygen content of Al Bronze decreases from 53.3% in the depth direction, and decreased to 25.5% in 0.24 μm. In contrast, Sulfide Al Bronze 1, the oxygen content gradually decreased from the 58.5% to 45.2% in the depth direction to 0.24 μm. Sulfide Al Bronze 1 was much oxidized.

On the other hand, iron content in Al Bronze 2 increased from 9.82% to 40.2% in the depth direction. In contrast, on Sulfide Al Bronze 1, the Fe content had increased gradually from 12.1% to 24.8%. It could be said that Sulfide Al Bronze 1 formed a thicker film. From these results, oxidation films derived from sulfide made friction characteristics improved.

Conclusion

Friction properties of Sulfide Al bronze were investigated. It was clarify that the size of sulfide and contents of sulfides were affect the friction properties. Larger grain size of sulfide enable form oxide film easily, resulting superior friction property. On the other hand, it took much time to form oxide film when specimen had smaller sulfide. That made running-time longer, and stick-slip had occur.

By increasing contents of sulfide, a part of bornite that was initial sulfide in the specimen, had changed aluminum sulfide. Because aluminum sulfide was hard material, mating steel was damaged and stick-slip had occurred. Moreover, that made it difficult to form oxide film.

Under the lubricant condition, PAO and sulfide did not react and thicker film was formed on the friction surface and keep friction coefficient lower.

Acknowledgement:

This reserch was financially supported by the Kansai University Grant-in-Aid for progress of reserch in graduate course, 2017.

References

1. G.A. Baglyuk, F.I. C.Z. Shen, L.B. Wei, G. Yu, *Influence of aluminium on the mechanical and tribotechnical properties of sintered copper-based friction material*, Powder Metallurgy and Metal Ceramics, Vol. 42, No. 3-4, (2003), 210- 212.
2. H.Mitani, *Research on the sintering of mixed compacts for Aluminium-Bronze*, Journal of the Japan Society of Powder and Powder Metallurgy, Vo.20, No.1, (1973), 1-9.
3. S.Kimura, S.Masuoka, Y.Arami, F.Nishimura, J.H.Kim, S.Yonezawa, *Surface Fluorination of Aluminum-Bronze Powder Using Fluorine Gas and its Sintering Property*, Journal of the Japan Society of Powder and Powder Metallurgy, Vol.61, No.8, (2014), 403-409.
4. J. Deng, T.Cao, Z.Ding, J.Liu, J.Sun, J.Zhao, *Tribological behaviors of hotpressed Al₂O₃/TiC ceramic composites with the additions of CaF₂ solid lubricants*, Journal of the European Ceramic Society 26, (2006), 1317-1323.
5. S.Masuoka, Y.Arami, S.Nagai, *Effect of Adding Al-Ca Fluoride on Sintering Behavior of Aluminum-Bronze Powder*, Journal of the Japan Society of Powder and Powder Metallurgy, Vol. 49, No.11, (2011) .1003-1008.
6. H.Wu, J.Li, H.Yi, X.Zeng, L. Lv, T. Ren, *The tribological behavior of diestercontaining polysulfides as additives in mineral oil*, Tribology Internal, Vol.40, No.8, (2007), 1246-1252.
7. R. H. Van Stone, T. B. Cox, J. R. Low, J. A. Psioda, *Microstructural aspects of fracture by dimpled rupture*, International Metals Reviews, Vol.30 , No.4 , (1985) ,157-179.
8. P.M.Aziz, H.P.Godard, T.Nakayama, *Mechanism by which Non-Ferrous Metals Corrode in the Atmosphere*, Corrosion Engineering Digest, Vol.9, No.1, (1959) ,32-37(in Japanese).
9. K.Sakamoto, H.Yaguchi, T.Sugimura, G.Anan, A.Yoshida, T.Tsuji, *Development of PB-free Low Carbon Resulfurized Free-cutting Steels*, R&D Kobe Steel Engineering Reports, Vol.56, No.3, (2006),35-39.
10. J. Schell, P. Heilmann, D. A. Rigney, *Friction and Wear of Cu-Ni Alloys*, Wear, Vol.75 , No.2, (1982), 205-220.

FABRICATION OF A POROUS TITANIUM / HYDROXYAPATITE METAL-CERAMIC COMPOSITES VIA POWDER INJECTION MOLDING WITH SPACE HOLDER METHOD

Mohd Yusuf Zakaria, Abu Bakar Sulong, Norhamidi Muhamad, Muhammad Hussain Ismail* and Mohd Ikram Ramli

Department of Mechanical and Material Engineering, Faculty of Engineering and Built Environment,
Universiti Kebangsaan Malaysia, Selangor, Malaysia.

*Centre for Advanced Materials Research (CAMAR), Faculty of Mechanical Engineering, Universiti
Teknologi MARA, Selangor, Malaysia

Abstract: A porous Ti_6Al_4V -hydroxyapatite composite were fabricated by powder injection molding (PIM) with space holder method. Titanium and hydroxyapatite were mixed at a 9:1 ratio with the solids loading of 68 vol.% with 20 % of NaCl space holder content using a binder system consists of a low density polyethylene and a palm stearin binder at 4:6 ratio. The binders were chemically and thermally removed and the sintering process is done at 1350 °C for 5 hours under vacuum environment. Ti_6Al_4V -hydroxyapatite composite with 37.03 % of porosity is successfully produced. The combination of PIM and space holder method is a potential process for future generation of implant material at a larger scale.

Introduction

Titanium and its alloys have attracted researchers to develop a new implant material due to the fact that titanium has excellence mechanical properties, high corrosion resistance and good biocompatibility [1]. However, the mechanical properties of titanium did not match the mechanical properties of the natural bone which leads to stress shielding phenomena during the implant process [2]. These disadvantages provide a new opportunity for research in developing new generation implant materials. There are several methods that has been studied, among them are using secondary materials such as hydroxyapatite to overcome the mismatch mechanical properties of titanium to the natural bone. Hydroxyapatite is a bioactive ceramic material that possess the similar properties to the natural bone but brittle at the same time^[3,4].

Early development of titanium-hydroxyapatite begins with a coating technique which commonly involves plasma spray and electro deposition method^[5,6]. However, the coating method has

a weakness where the hydroxyapatite coating could peel off from the titanium substrate over time. Furthermore, titanium and hydroxyapatite were combine to form a composite material through powder metallurgy methods such as powder compaction and powder injection molding (PIM) [7]. In addition, the mechanical properties of the titanium can be reduced by introduction of a porous structure. There are various methods available to produce a porous structure. One of the method is using space holder method where the space holder material is added together with the titanium and then removed before the sintering process [8]. The space left by the space holder material will form a hole or void in the titanium structure [9]. The great benefit of using the space holder method is the pore characteristic can be selected based on the space holder material properties such as size and shape [10].

Therefore, this study is focusing on the combination of powder injection molding of

FABRICATION OF A POROUS TITANIUM / HYDROXYAPATITE METAL-CERAMIC COMPOSITES VIA POWDER INJECTION MOLDING WITH SPACE HOLDER METHOD

titanium-hydroxyapatite composite with the space holder method for producing the porous structure.

Methodology

The starting material consists of gas-atomized Ti_6Al_4V powder and hydroxyapatite obtained from TLS-Technik, Germany and China respectively. NaCl space holder with rectangular morphology was obtained from Sigma-Aldrich. The average size of the Ti_6Al_4V , hydroxyapatite and NaCl space holder powders are 19.54 μm , 61.95 μm , and 939.77 μm respectively. The powder is mixed with a two-component binder system consists of a low-density polyethylene, (LDPE) as the backbone binder and a palm stearin as a surfactant. The ratio of LDPE and palm stearin is kept at 4:6. Meanwhile the powders composition for titanium and hydroxyapatite are at 9:1 with 20 % of space holder content.

The feedstock was produced by mixing titanium, hydroxyapatite and NaCl powder with the binder using a Brabender mixer at a temperature of 150 $^{\circ}C$ feedstock is injected into a mold with tensile bar shape using DSM Xplorer injection machine at 160 $^{\circ}C$ and 10 Bar of pressure. The green part then immersed in water at 45 $^{\circ}C$ for 6 hours to dissolve the NaCl, follows by immersing in heptane solution at 60 deg for 6 hours. Then, the remaining binder is removed thermally in argon environment at 500 $^{\circ}C$. The brown part undergoes the sintering process using a high vacuum furnace at 1350 $^{\circ}C$ for 5 hours. The porosity of the Ti-HA composite were obtained based on the Archimedes method were the porosity is calculated based on the displaced water when submerge in distilled water using a weight balance. The surface and the cross section of the sintered samples were examined using a scanning electron microscope (SEM) model HITACHI TM 1000.

Results and Discussion

The feedstock was successfully injected without any apparent defects. Then the binders where chemically and thermally removed via a two-step debinding process to produce a brown part. Microstructural changes during all the PIM stages is shown in Figure 1 where the binders were completely removed as the void is observed arounds the particles resulting from the spaces left by the binders. The sintering process is done at high vacuum condition at 1350 $^{\circ}C$ for 5 hours. The necking process start to occur at 3 hours of holding time as seen in Figure 2 (a).

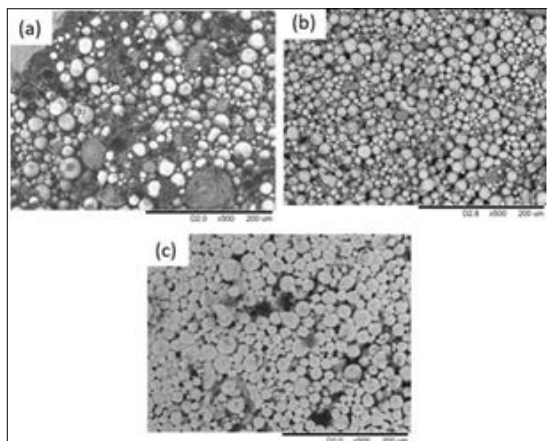


Figure 1. Microstructural changes for (a) green part, (b) brown part and (c) sintered part

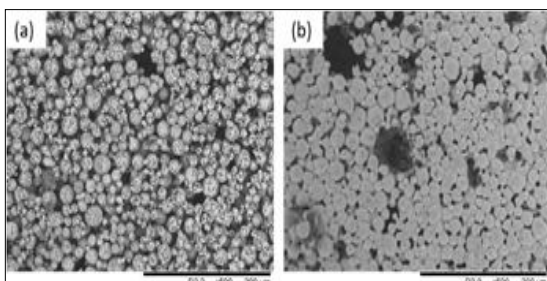


Figure 2. Sintered at 1350 $^{\circ}C$ for (a) 3 hours and (b) 5 hours.

FABRICATION OF A POROUS TITANIUM / HYDROXYAPATITE METAL-CERAMIC COMPOSITES VIA POWDER INJECTION MOLDING WITH SPACE HOLDER METHOD

The sintered Ti_6Al_4V -HA composite is successfully produced with the porosity of 37.03% and density of 3.06 g/cm^3 . The porosity value is higher than the space holder content (20%) is due to the voids left by the binders during the debinding stage. The voids left by the binders always associated with the micro pores as seen in the Figure 2 (b), meanwhile pores resulting from the space holder often bigger according to the space holder size.

4. Conclusions

A porous Ti_6Al_4V -HA composite was successfully fabricated through the powder injection molding process with the space holder method with the porosity of 37.03 %. The porosity value is higher than the space holder content due to the space left by the binders. The combination of PIM and a spce holder method has great potential in producing a porous metal-ceramic composite for the generation of implant material.

5. References

1. Pérez-Sánchez A, Yáñez A, Cuadrado A, Martel O, Nuño N. 2018. Fatigue behaviour and equivalent diameter of single Ti -6Al-4V struts fabricated by Electron Beam Melting orientated to porous lattice structures. *Materials & Design*;155:106-15.
2. Bovand D, Yousefpour M, Rasouli S, Bagherifard S, Bovand N, Tamayol A. 2015. Characterization of Ti -HA composite fabricated by mechanical alloying. *Materials & Design*;65:447-53.
3. Thian ES, Loh NH, Khor KA, Tor SB. 2002. Microstructures and mechanical properties of powder injection molded Ti -6Al-4V/HA powder. *Biomaterials*;23(14):2927-38.
4. Szczeń A, Hołyś L, Chibowski E. 2017. Synthesis of hydroxyapatite for biomedical applications. *Advances in Colloid and Interface Science*;249:321-30.
5. Lugovskoy A, Lugovskoy S. 2014. Production of hydroxyapatite layers on the plasma electrolytically oxidized surface of titanium alloys. *Materials Science and Engineering: C*;43:527-32.
6. Ozhukil Kollath V, Chen Q, Closset R, Luyten J, Traina K, Mullens S. 2013. ACvs. DCelectrophoretic deposition of hydroxyapatite on titanium. *Journal of the European Ceramic Society*;33(13-14):2715-21.
7. Arifin A, Sulong AB, Muhamad N, Syarif J, Ramli MI. 2015. Powder injection molding of HA/ Ti_6Al_4V composite using palm stearin as based binder for implant material. *Materials & Design*;65:1028-34.
8. Li B-q, Li Z-q, Lu X. 2015. Effect of sintering processing on property of porous Ti using space holder technique. *Transactions of Nonferrous Metals Society of China*;25(9):2965-73.
9. Jian X, Hao C, Guibao Q, Yang Y, Xuewei L. 2015. Investigation on relationship between porosity and spacer content of titanium foams. *Materials & Design*;88:132-7.
10. Muñoz S, Pavón J, Rodríguez-Ortiz JA, Civantos A, Allain JP, Torres Y. 2015. On the influence of space holder in the development of porous titanium implants: Mechanical, computational and biological evaluation. *Materials Characterization*;108:68-78.

PRODUCTION OF IRREGULAR POROUS Ti-6Al-4V VIA SLM

Ahmad Moloodi, Mona Abedinpour, Abolfazl Faramarzian, Ali Haerian

Iranian Academic Center for Education, Culture and Research (ACECR), Mashhad, IRAN

Sadjad University of Technology, Mashhad, IRAN

Abstract: Selective laser melting (SLM) is an additive manufacturing technique in which functional, complex parts can be created directly by selectively melting layers of powder. In this research, the complex irregular porous structure model was printed using Ti-6Al-4V alloy powders via SLM. The microstructure, shrinkage, and morphology were studied using light optical and scanning electron microscopy. EDS analysis was used to determine the chemical analysis of printed specimens. The results showed that the microstructure was the conventional martensitic phase in Ti-6Al-4V alloys and there was no evidence of pores and unexpected phases in the matrix. It also showed that the initial complex model was almost completely printed via SLM. The results of the shrinkage measurements revealed that the average linear shrinkage was about 5.8%.

Introduction

3D printing techniques are relatively new methods of rapid producing samples. 3D printing has several techniques like FDM, EBM, SLM, and DLP. Some of these techniques are only used for polymers, while other ones may be used for metals and ceramics. Selective laser melting (SLM) is one of the techniques that emerged in the late 1980s. During the SLM, a product is formed by selectively melting successive layers of powder by the interaction of a laser beam^[1].

Upon irradiation, the powder material is heated and, if sufficient power is applied, melts and forms a liquid pool. Afterward, the molten pool solidifies and cools down quickly, and the consolidated material starts to form the product. The non-irradiated material remains in the building cylinder and is used to support the subsequent layers^[2].

Compared to conventional manufacturing techniques, SLM offers a wide range of advantages, namely a lower time-to-market, a near-net-shape production without the need for expensive molds, and high material utilization

rate. Moreover, due to the additive and layer-wise production, the SLM process is capable of producing complex geometrical features that cannot be obtained using conventional production routes^[3].

Titanium alloys are widely used for implant materials due to their biocompatibility and high corrosion resistance and mechanical properties^[4]. The typical methods for producing Ti implant are machining and forming. Recently, the SLM method was used to produce Ti implant especially dental fixtures^[5]. The new studies show that the porous Ti implant can replace the solid (more rigid) one to remove the stress shielding phenomenon. Furthermore, it is more similarity of the implant with the bone structure^[6-7].

The porous implant has also the advantage of allowing the bone to grow inside the implant, thus enhancing implant fixation^[8-9].

In this study, the porous irregular structure was designed and printed via SLM with the medical grade Ti alloys. The microstructure and shrinkage as like as the porosity were investigated. The probability of the change in

chemical composition and morphology were also studied.

Experimental procedure

In this study, the first, initial model of irregular porous structure was designed using Rhino Software. The size of the model was a cube with a $20 \times 20 \times 20$ mm³ dimension (Fig.1).

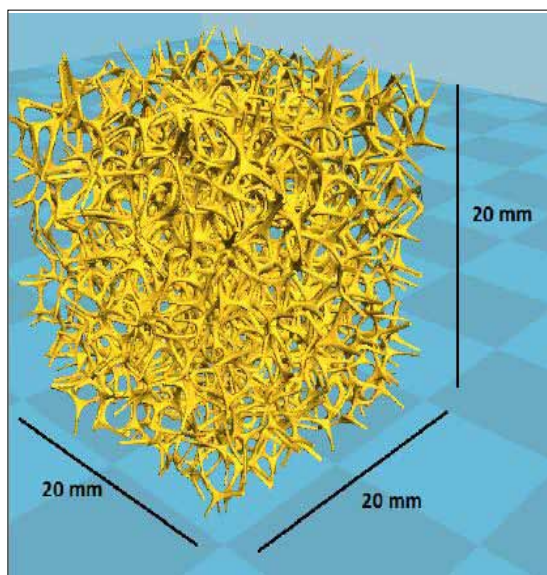


Fig.1 Initial model of the irregular porous structure

Ti6Al4V (Ti Alloys grade 5) powders were selected as an initial material in SLM. The size and purity of powders were according to ASTM F136.

A piece of the specimen was cut and mounted. Then grinding to 1200 mesh and finally polished by 0.5 μm diamond paste. After polishing and rinsing in acetone and ethanol, samples were etched with a solution consisting of Oxalic acid saturated in 100 mL H₂O+2.5 mL HF. Optical and scanning electron microscopy were used to investigate the morphology and microstructure of the sample. The probability of presence of micropores in the microstructure and the

quality of powder sintering via SLM as like as the chemical composition of produced sample were also studied. The porosity of samples was measured using equation 1 [10].

$$\text{Porosity\%} = \frac{\text{Density}_{\text{theory}} - \text{Density}_{\text{experimental}}}{\text{Density}_{\text{theory}}} \times 100 \text{ eq. 1[10]}$$

Fig. 2 shows the length of pores and cross-section in initial model. According to these figures, the average size of the cell walls and pores were 532.66 μm and 1.475mm, respectively. In order to determine the linear shrinkage, the diameter of the cross-section of cell walls in the initial 3D model (Fig. 2) and produced samples were measured. The linear shrinkage was calculated according to equation 2 [11]:

$$\text{Length Shrinkage} = \frac{D_1 - D_2}{D_1} \times 100 \quad \text{eq.2[11]}$$

where D₁ is the diameter of the cross-section of cell walls in the initial 3D model (Fig. 2), and D₂ is the diameter of the cross-section of cell walls in produced samples.

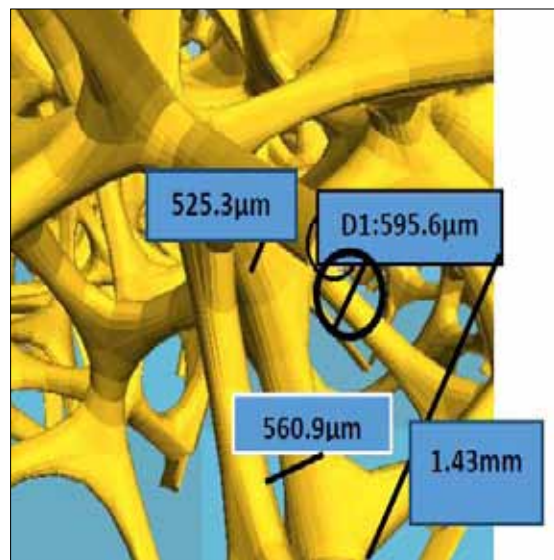


Fig. 2 The diameter of cross-section cell walls and pores in initial model

Results and Discussion

1. Microstructures and morphologies

Fig. 3 shows the printed sample via SLM. As can be seen, the dimensions and morphology of printed samples are like the initial model (Fig. 1). It means that the initial complicated model can be completely printed by the accuracy of the SLM. The stereographic images show that the cross-sectional of the cells wall convert from triangle to circle [12].

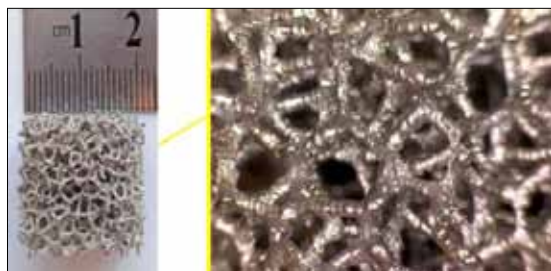


Fig.3 the printed sample and stereograph image

Figure 4 shows the SEM image of cross-section and surface of cell walls. As it can be seen, the homogenous morphology was printed and there is no sign of any remaining powders after SLM. It is also shown that there are a small number of natural pores on the surface and cross section which are usual in the SLM products [24,13].



Fig. 4. (a) SEM image of the cross-section of the cell wall, (b) surface of cell walls, (c) SEM image of some usual natural pores

The EDS analysis results (Fig.5) illustrated that main alloying elements of Ti6Al4V Alloys were remained after SLM 3D printing and also there is no sign of any impurities [14],[15].

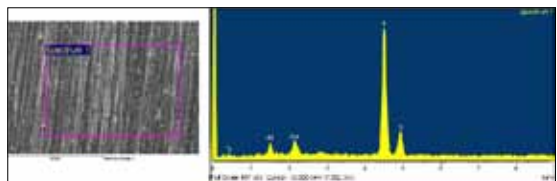
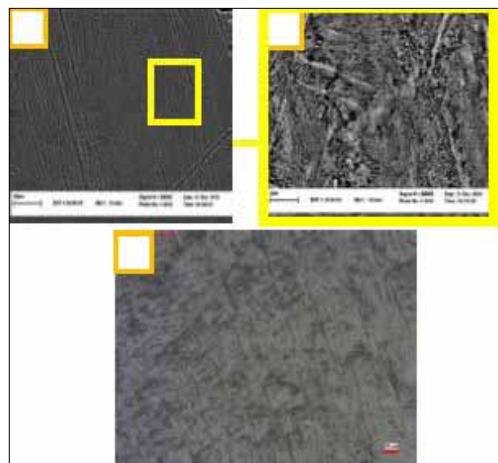


Fig. 5 The results of EDS analysis

Figure 6 shows a microstructure of the specimen. The microstructure consisted of $\alpha+\beta$ phases and the martensitic microstructure appeared. As can be seen in fig. 6, α phase with the Widmanstatten pattern, is brightened to the needle state, and the β phase is seen in darker colors [2,13,16-18].



*Fig. 6 The microstructure of specimen (a,b) SEM image
(c) OM image*

2. The length shrinkage

Figure 7 shows the size of the cross section of cell walls and pores after printing. The mean diameter of cross section was 501.77 μm . Considering Eq.2 and the average diameter of the cross section in the initial model (fig.2), the linear shrinkage of the specimen is 5.8%. Generally, all metals have some shrinkage during solidification from liquid phase. The percentage of this shrinkage is very important to determine the final dimension of products. As the initial powders in SLM melt during the process, the shrinkage is usual during solidification [4,12,19].

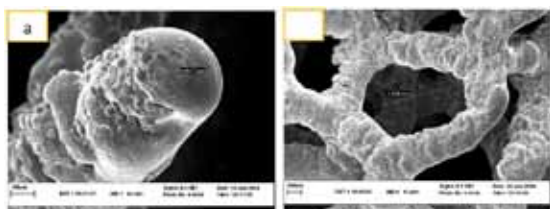


Fig. 7 Diameter of (a)cross section cell walls and (b) pores in the produced sample

Conclusion

In this research, the probability of producing Ti6Al4V alloy via SLM was investigated. The results can be summarized as follows:

1. The SLM method can print the alloy very close to the initial model and the complication of pores and cell walls can be reproduced.
2. The microstructure of cross-section shows that the minimum micro defect occurred during printing.
3. The usual martensitic structure for Ti6Al4V with $\alpha+\beta$ phase distribution was observed in the entire sample.
4. The diameter measurement of the cross-section shows that the 5.8% linear shrinkage has occurred during printing.
5. The EDS analysis showed that the initial chemical composition did not change and there is no sign of oxidation.

Reference

1. Z. Chen et al., "3D printing of ceramics: A review," *J. Eur. Ceram. Soc.*, 2018.
2. E. Sallica-Leva, A. L. Jardini, and J. B. Fogagnolo, "Microstructure and mechanical behavior of porous Ti-6Al-4V parts obtained by selective laser melting," *J. Mech. Behav. Biomed. Mater.*, vol. 26, pp. 98–108, 2013.
3. Z. Linxi, Y. Quanzhan, Z. Guirong, Z. Fangxin, S. Gang, and Y. Bo, "Additive manufacturing technologies of porous metal implants," vol. 11, no. 4, 2014.
4. L. Yuan, S. Ding, and C. Wen, "Additive manufacturing technology for porous metal implant applications and triple minimal surface structures: A review," *Bioact. Mater.*, vol. 4, no. 1, pp. 56–70, 2019.
5. Z. J. Wally, A. M. Haque, A. Feteira, F. Claeysen, R. Goodall, and G. C. Reilly, "Selective laser melting processed Ti6Al4V lattices with graded porosities for dental applications," *J. Mech. Behav. Biomed. Mater.*, vol. 90, pp. 20–29, 2019.
6. L. Mullen, R. C. Stamp, W. K. Brooks, E. Jones, and C. J. Sutcliffe, "Selective Laser Melting: A Regular Unit Cell Approach for the Manufacture of Porous , Titanium , Bone In-Growth Constructs , Suitable for Orthopedic Applications," pp. 325–334, 2008.
7. A. Cheng, A. Humayun, D. J. Cohen, B. D. Boyan, and Z. Schwartz, "Additively manufactured 3D porous Ti-6Al-4V constructs mimic trabecular bone structure and regulate osteoblast proliferation, differentiation and local factor production in a porosity and surface roughness dependent manner," *Biofabrication*, vol. 6, no. 4, 2014.
8. X. Bin Su, Y. Q. Yang, P. Yu, and J. F. Sun, "Development of porous medical implant scaffolds via laser additive manufacturing," *Trans. Nonferrous Met. Soc. China (English Ed.)*, vol. 22, no. SUPPL. 1, pp. s181–s187, 2012.
9. S. Tunchel, A. Blay, R. Kolerman, E. Mijiritsky, and J. A. Shibli, "3D Printing/Additive Manufacturing Single Titanium Dental Implants: A Prospective Multicenter Study with 3 Years of Follow-Up," *Int. J. Dent.*, vol. 2016, 2016.
10. B. Ferrar, L. Mullen, E. Jones, R. Stamp, and C. J. Sutcliffe, "Gas flow effects on selective laser melting (SLM) manufacturing performance," *J. Mater. Process. Technol.*, vol. 212, no. 2, pp. 355–364, 2012.
11. M. S. Ahmad, B. T. H. T. Baharudin, Z. Leman, N. Ismail, and S. Sulaiman, "Thermal parameter affects on the part built using 3D printer projet SD 3000," *15th Int. Conf. Adv. Mater. Process. Technol. AMPT 2012*, vol. 773–774, pp. 833–841, 2014.
12. J. Parthasarathy, B. Starly, S. Raman, and A. Christensen, "Mechanical evaluation of porous titanium (Ti6Al4V) structures with electron beam

- melting (EBM)," J. Mech. Behav. Biomed. Mater., vol. 3, no. 3, pp. 249–259, 2010.*
13. L. Thijs, F. Verhaeghe, T. Craeghs, J. Van Humbeeck, and J. P. Kruth, "A study of the microstructural evolution during selective laser melting of Ti-6Al-4V," *Acta Mater.*, vol. 58, no. 9, pp. 3303–3312, 2010.
 14. J. Elizabeth Biemond, T. S. Eufrásio, G. Hannink, N. Verdonschot, and P. Buma, "Assessment of bone ingrowth potential of biomimetic hydroxyapatite and brushite coated porous E-beam structures," *J. Mater. Sci. Mater. Med.*, vol. 22, no. 4, pp. 917–925, 2011.
 15. A. Basalah, "Additive Manufacturing of Porous Titanium Structures for Use in Orthopaedic Implants," 2015.
 16. L. E. Murr et al., "Microstructures and mechanical properties of electron beam-rapid manufactured Ti-6Al-4V biomedical prototypes compared to wrought Ti-6Al-4V," *Mater. Charact.*, vol. 60, no. 2, pp. 96–105, 2009.
 17. I. Yadroitsev, P. Krakhmalev, and I. Yadroitseva, "Selective laser melting of Ti6Al4V alloy for biomedical applications: Temperature monitoring and microstructural evolution," *J. Alloys Compd.*, vol. 583, pp. 404–409, 2014.
 18. A. Paula, M. Del, D. F. Scotini, and K. F. De Souza, "a Importância Da Escrituração Contábil Regular Nas Micro E Pequenas Empresas 1 Introdução," vol. 243, pp. 32–45, 1998.
 19. X. Y. Cheng et al., "Compression deformation behavior of Ti-6Al-4V alloy with cellular structures fabricated by electron beam melting," *J. Mech. Behav. Biomed. Mater.*, vol. 16, no. 1, pp. 153–162, 2012.

FORMATION OF DENSE MoSi₂ COATING ON NIOBIUM ALLOY C-103 FOR OXIDATION PROTECTION

R.V. Krishnarao and G. Madhusudhan Reddy

Defence Metallurgical Research Laboratory, Kanchanbagh, Hyderabad, India

Abstract: MoSi₂ is an attractive coating material for long term high temperature protection of C/C, Graphite, and Mo. Several techniques including air plasma coating (APS) of Mo followed by heat treatment and siliconisation, spark plasma sintering (SPS), D-gun spraying of Mo followed by co deposition of Si and Al were developed to prepare Mo-Si coatings on Nb base alloys. Due to big pores and cracks in the coating long term applications at high temperatures are limited. Obtaining a dense MoSi₂ coating on Nb base alloy substrate is still not clear. In this work a dense and thick MoSi₂ coating has been formed on C-103 substrate by tungsten inert gas welding (TIG) technique. Using filler rods prepared from MoSi₂ sintered at 1350°C with 30 – 50 vol. % of clay binder, cladding of C-103 alloy by TIG was studied. The absence of clay phase in the TIG coated MoSi₂ suggests that the clay phase was evaporated due to high arc temperature. Formation of about 2μm thick NbSi₂ layer was observed at the interface between C-103 and MoSi₂ coating. The coating mainly consists of Mo₅Si₃ in the matrix of MoSi₂. The coated C-103 was not oxidized after heat treatment at 1550°C in air for 1h.

Introduction

The Nb base alloy C-103 with attractive properties of low density, high melting point, low rate of sublimation and good strength at elevated temperatures is a potential material for advanced high-temperature aerospace applications. But it suffers from rapid degradation due to the formation of non-protective oxide scale of Nb above 900°C. Addition of alloying elements (Cr, Al, Hf and B) or surface coatings (Nb-aluminides and Nb-silicides) have been developed for oxidation protection. MoSi₂ is an attractive coating material for long term high temperature protection of C/C, Graphite, and Mo. Several techniques were developed for the preparation of Mo-Si coating on the surface of Nb/Nb base alloy. Mo(Si, Al)₂ and Mo₅(Si, Al)₃ coating was developed by air plasma coating (APS) of Mo-Si-Al on NbSS/Nb₅Si₃ composites [1]. MoSi₂ coating on the pure Nb by slurry method was reported by Xiao et al [2]. But the long term application at high temperature was limited due to the pores and cracks in coating. MoSi₂ coating on the pure Nb by Spark plasma sintering (SPS) was reported by Yan et al [3]. The SPS method is limited to the substrates with regular or simple shapes. A dense Mo layer on the Nb

substrate will improve the quality of subsequent siliconizing layer. APS of Mo followed by heat treatment and siliconisation^[4], and D-gun spraying of Mo followed by co deposition of Si and Al^[5] were also reported. But simple method of formation of dense MoSi₂ on Nb base alloy substrate is still not developed. In this work a dense MoSi₂ coating has been formed on C-103 substrate by tungsten inert gas welding (TIG). The C-103 sample with cladded MoSi₂ was tested for oxidation at 1550°C.

Experimental

The MoSi₂ powder of 99.8% purity with average particle size <5μm was supplied by LTC (Chemical) Inc, Chestnut Ridge, New York USA. China clay in 30 - 50 vol. % was added to it and mixing of powders was done for 8 h in a polythene bottle with alumina balls. A water solution with 2-4 wt.% polyvinyl alcohol (PVA) binder was added and blended for 1 h. After slurry coating the C-103 composite coupons of 10mm X 10mm X 3mm are dried in an oven at 373 K for 2 h. The dried slurry coated samples are placed in separate graphite crucibles with minimum contact with grafol sheet pre-coated with BN water solution to avoid reaction of

FORMATION OF DENSE MoSi₂ COATING ON NIOBIUM ALLOY C-103 FOR OXIDATION PROTECTION

the coatings with crucible. The crucibles were placed in the resistance heating furnace (ASTRO, USA, Model 1000-3060-FP20). The furnace was initially evacuated to a moderate vacuum (5×10^{-2} torr) before inletting the argon at 1 atm. Temperature was monitored with a radiation pyrometer Model 939A3 of Honeywell. Heating rate employed was $\sim 15^\circ\text{C min}^{-1}$. The formation of coating was carried out at 1350°C / 1 h. Similarly, a 60 mm dia. compact of MoSi₂ + 30 vol. % clay was pressed in a steel die and sintered at 1350°C / 1 h. Filler rods of size 50mm X 5mm X 2mm for TIG were cut from the sintered composite. Alternately 1800 grade MoSi₂ heating element rods were also used as filler. TIG machine of ESAB make, Model TIG 300A, Kolkata, India was used. The C-103 coupons were laid on a steel platform. A welding current of 90–120 A was employed. After welding the argon flow was continued till the sample was cooled to a temperature less than 800°C . Similarly the TIG coating was performed on all the sides of the C-103 sample. Isothermal oxidation was carried out for 1 h at 1550°C in air. The specimens taken in alumina crucibles are placed on the furnace hearth and directly introduced into the hot zone of the furnace. After holding for 1 h minutes at oxidation temperature the furnace hearth was lowered and specimens in alumina crucible are allowed to cool down to room temperature. The surface morphology and cross sections of polished samples were analyzed for microstructure with a scanning electron microscope SEM EVO 18 of Carl Zeiss Germany equipped with EDAX, AMETEK.

Results and discussion

After heat treatment in furnace at 1350°C the coatings were not continuous and partly non adherent. Only TIG cladded coatings of MoSi₂ are dense and firmly bonded to C-103 samples. The typical C-103 sample uncoated and after cladding with MoSi₂ by TIG are shown in Fig. 1. The C-103 sample is fully covered on all sides with dense MoSi₂ (Fig. 1 (b)). The SEM analysis of polished cross section of MoSi₂ cladded

sample revealed that the interface between the base alloy and coating is continuous and free from voids and cracks (Fig. 1 (c)). The coating is mainly MoSi₂, the dark phase in which Mo₅Si₃ the light phase is distributed at the interface. The precipitation of Mo₅Si₃ occurred due to the reaction of Nb in C-103 with Si of MoSi₂ to form NbSi₂. At high magnification the formation of 2 μm thick layer of NbSi₂ grey phase between C-103 white phase and coating (Fig. 1 (d)).

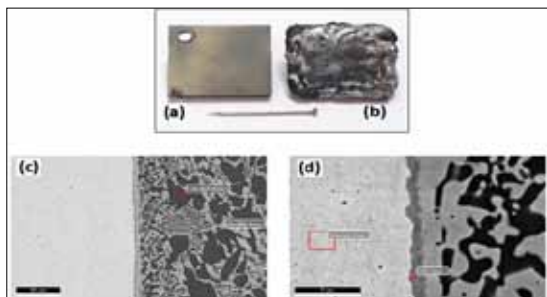


Fig. 1. Typical C-103 composite sample (a) before and (b) after cladding with MoSi₂ by TIG. (c) SEM image of polished cross section of the coated C-103 (White phase), dark phase - MoSi₂, and light phase - Mo₅Si₃. (d) same as in (c) at high magnification showing the 2 μm thick NbSi₂ (grey) layer between C-103 and coating.

The formation of dense and thick MoSi₂ coating was possible due the high arc temperature involved in TIG process. Since the filler material (MoSi₂ + 30 vol % clay) is molten under high arc temperature its wettability and flowability on C-103 alloy is possible. But no phase related to clay is visible in the coating. This could be due to the evaporation of clay material under high arc temperature of about 3000°C . The coated C-103 sample after isothermal oxidation in air at 1550°C for 1 h was unaffected due to the protection of MoSi₂ coating. However, the coating (MoSi₂) was reacted at points of contact with the alumina crucible (Fig. 2 (a)). The cross section of the coated and oxidized sample shows that the C-103 is intact even after exposure to a high temperature of 1550°C for 1 h (Fig. 2 (b)).

FORMATION OF DENSE MoSi₂ COATING ON NIOBIUM ALLOY C-103 FOR OXIDATION PROTECTION

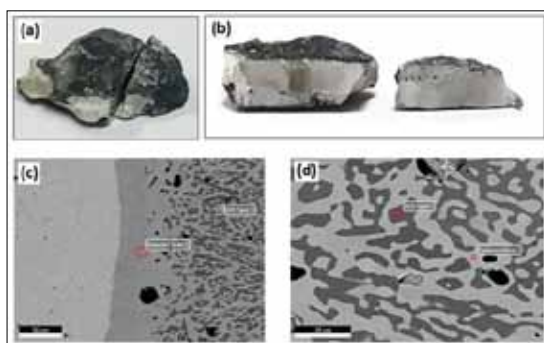


Fig. 2. Cladded C-103 composite sample (a) after oxidation at 1550°C for 1 h and (b) cross section of the oxidized sample in (a). (c) disappearance of NbSi₂ layer and formation of Nb₅Si₃ at the interface. (d) Nb identified in Mo₅Si₃ and MoSi₂ phases in coating.

The MoSi₂ coating was also well protected with the formation of glass layer on the surface. The SEM analysis of the cross section revealed that the NbSi₂ layer disappeared and Nb diffused into the coating area. The light phase near the interface is identified as Nb₅Si₃ (Fig. 2 (c)). Nb is also identified in the Mo₅Si₃ and MoSi₂ in coating (Fig. 2 (d)). This is a clear evidence for diffusion of Nb and its reaction with Si in the coating.

Conclusions

Dense and thick MoSi₂ coating has been formed on C-103 substrate by tungsten inert gas welding (TIG) technique. (MoSi₂ + clay) composite has been used for the preparation of filler rods for TIG. The MoSi₂ coating formed by TIG has been found to protect the C-103 alloy from oxidation at 1550°C for 1h. The clay phase was found to evaporate due to high arc temperature involved in TIG. Formation of about 2μm thick NbSi₂ layer was observed at the interface between C-103 and MoSi₂ coating. NB was found to diffuse into coating and react with Si in the coating.

Acknowledgements

Authors acknowledge the financial support from the Defence Research and Development

Organization, Ministry of Defence, Govt. of India, New Delhi, in order to carry out the present study under project DMR-295. They are grateful to the Director, DMRL, Hyderabad, for his constant encouragement. The Authors acknowledge the support of ACG, XRD and SEM groups of DMRL.

6. References

1. D.Z. Yao, W.Y. Gong, and C.G. Zhou, *Development and Oxidation Resistance of Air Plasma Sprayed Mo-Si-Al Coating on an Nb₅Nb₅Si₃ In Situ Composite Corros. Sci.*, 2010, 52(8), p 2603-2611.
2. L.R. Xiao, D.Q. Yi, L. Yin, and Z.G. Cai, *Morphology and Structure of High Temperature MoSi₂ Coating on Niobium*, *Trans. Nonferrous Met. Soc. China*, 2005, 15(1), p 18-22.
3. J.H. Yan, Y. Wang, L.F. Liu, and Y.M. Wang, *Oxidation and Interdiffusion Behavior of Niobium Substrate Coated MoSi₂ Coating Prepared by Spark Plasma Sintering*, *Appl. Surf. Sci.*, 2014, 320, p 791-797.
4. JianHui Yan, Yi Wang, LongFei Liu, Yueming Wang, and Fang Chen, *Preparation of Protective MoSi₂ Coating on Niobium Substrate*, *Journal of Thermal Spray Technology Volume 24(6) August 2015 – 109*.

INVESTIGATION ON THE EFFECT OF TIN ADDITION ON FOAMING BEHAVIOUR OF Al₇SiMg PRODUCED BY POWDER ROUTE

Manas Hardikar, R.S.S Srivaishnav, Aniket Sakalley, and Sasikumar. S

Department of Mechanical Engineering, SRM Institute of Science and Technology,
Kattankulathur, Tamil Nadu, India

Abstract: The major drawback in producing aluminium foams using powder route is the mismatch between the decomposition temperature of the gas releasing agent and the pure Al or Al alloy, which leads to crack like pore formation and hydrogen loss before foaming begins. Tin can be introduced in the powder mixture to reduce the cracking issues. In this work, foaming precursors were made by cold compaction using 100 Tonne hydraulic press followed by heating in the electric furnace at 730–750°C for 12 minutes. The precursor containing elemental powders of Aluminium, 7% Silicon, 1% Magnesium with varying amount of Tin (0, 1, 3 and 5) was mixed by tumbling mixer. The materials were characterized using XRD, TG-DSC, particle size analyser and SEM techniques. It was found that tin has played a key role in TiH₂ decomposition and modification of liquid Al's surface tension. It was concluded that use of tin proved to be a beneficial addition up to 3 wt.% as the pore structures became more uniform compared to precursors without tin. But, the problem of pore coalescence was noticed in the precursors with 5wt.% Sn.

Introduction

Closed cell Al foams are formed during powder compact melting technique. This technique describes about mixing of the metal powders with the blowing agent (1wt% TiH₂ is generally used) and get compacted to obtain high densified precursors. Generally, these densified precursors get heated in the furnace above the melting point of metal and foaming starts from the decomposition temperature of TiH₂ which releases H₂ gas. When the viscosity of melt and internal gas pressure, which produced by H₂ gas comes to equilibrium then gas starts creating bubbles in melt which leads to formation of pore structure in metal foams. When the surface tension of metal is low that it could not handle the gas pressure then foam collapse takes place. These metal foams are naturally high mechanical energy absorbers, good acoustic, well insulated to thermal properties and can also exhibit high stiffness to weight ratio. These characteristics are much more interesting to the automotive industry in safety and environmental concerns by introducing lighter, safer and greener vehicles

by replacing heavy parts with metal foams which have high stiffness to weight ratio, reduces fuel consumption and it can prevent injuries to the passengers in the event of accident due to its high mechanical energy absorbing capacity.

The difficulties faced during pure aluminium foaming is pore coalescence, foam collapse and metal drainage. These are caused due to the lack of stability during the foaming. To rectify this problem, Sn is added to the composition. In Al-Sn phase diagram, the Sn starts melting at 232°C and when it is slowly increases to 580°C, the small amount of solid Al gets dissolved in liquid Sn and when it crosses 580°C, the amount of Al dissolved in liquid Sn increases. The addition of Sn (1 to 5wt%) leads to decrease in the liquidus temperature of Al-Sn and helps to retain more amount of H₂ gas generated by TiH₂. By retaining more amount of H₂ leads to formation of a greater number of pores and the foaming stability occurs by decreasing the surface tension of Al layer by the Sn addition. The main difficulty faced in foaming is the mismatch temperature in decomposition of

INVESTIGATION ON THE EFFECT OF TIN ADDITION ON FOAMING BEHAVIOUR OF Al7SiMg PRODUCED BY POWDER ROUTE

TiH₂ and melting point of Aluminium which leads to crack like pore formation. To overcome it, the mismatch temperature gets reduced by decreasing the melting point of aluminium and increasing decomposition temperature of TiH₂ by heat treatment. For reducing the melting point of aluminium and to control foaming behaviour, we added Si and Mg as an alloying element. The presence of Si helps in reducing the melting point of Aluminium and improves the viscosity in metal. The eutectic temperature in Al-Si phase diagram is at 12.6wt% Si. To avoid eutectic point, Si generally varies at 7-9wt% in the composition. The presence of Mg in foaming leads to formation of oxide skin such as MgO or MgAl₂O₄ which impedes foam growth, but it helps in preventing the pore coalescence and metal drainage. The Mg also interacts with Sn and forms the intermetallic phase Mg₂Sn which is found along dendrite boundary in the cell wall. We use less amount of Mg which varies from 0.5 to 1wt% because it reduces the foaming expansion and interaction with Sn which leads to decrease in the effect of Sn in foaming process. The second step in reducing the mismatch temperature is by heat treatment of TiH₂ to increase its decomposition temperature. But with the presence of Sn in the composition, the dehydrogenation of TiH₂ can be done without heat treatment because Sn helps in gradual decomposition of TiH₂ in the following way.

In dehydrogenation of TiH₂, there is a formation of thin, solid TiAl₃ layer which is accelerated by liquid Sn. The layer stops the H₂ gas from releasing and pressure builds up inside the layer by increasing the temperature that leads to the continuous rupture of TiAl₃ layer which helps in the gradual decomposition of TiH₂. The healing of TiAl₃ layer takes place by the presence of Sn as it accelerates the formation of TiAl₃ layer again and the particles grow until the end of the reaction. The decomposition of TiH₂ in the absence of Sn leads to slow formation of TiAl₃ layer and high pressure builds up due to

increase in temperature which leads to sudden rupture of TiAl₃ layer and a massive amount of H₂ gas releasing at once, which may lead to foam collapse. By this, we come to know that Sn plays an important role in foaming behaviour and foaming stability. Our work was to investigate the foaming behaviour in Al7SiMg by the addition of Sn in varying amounts and its effect overall in the process.

Experimental Procedure

A. Materials

Pure Aluminium, Magnesium, Silicon, Tin and Titanium Hydride powders of size 30-50, 150, 100, 44 and 40 μm and 98, 99, 99.8 and 98% purity respectively used in the experiment were bought from commercial industries as shown in Table 1.

Table 1. Materials Specifications

POWDER	PURITY (%)	PARTICLE SIZE (μm)	SUPPLIER
Aluminium	99.7	30-50	Sun Ark Aluminium Industries (P) Limited, India
Magnesium	98	<150	SD Fine Chemicals, India
Silicon	99	<100	SD Fine Chemicals, India
Tin	99.8	44	Sigma Aldrich, India
TiH ₂ (as received)	98	40	Sigma Aldrich, India

B. Preparation of sample

The powders were conventionally mixed using a tumbler mixer for obtaining uniform distribution. The mixer consists of the tumbler with the lid being attached to the shaft of a 150 HP motor with a voltage regulator. The RPM of the motor can be varied with the varying input voltage. The mixing was done for 26-30 minutes with the voltage in the range between 65-70 volts and maintaining the RPM in the range of 120-140. For effective mixing, 20% of the total volume of the container was filled. Steel balls

INVESTIGATION ON THE EFFECT OF TIN ADDITION ON FOAMING BEHAVIOUR OF Al7SiMg PRODUCED BY POWDER ROUTE

were used to grind the powders and the ball to powder ratio was 5:1 by comparing the mass of the balls to that of the powder mass. Process is illustrated in Figure 1.

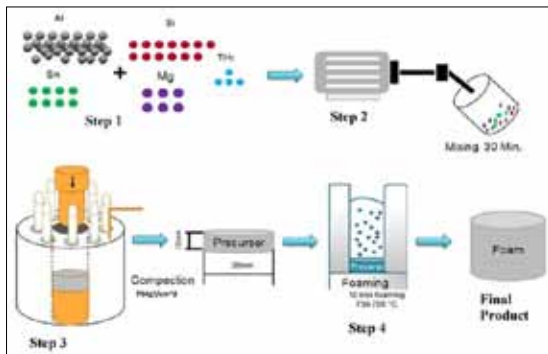


Figure 1: Schematic layout of Process methodology for production of metal foams by powder route.

C. Compaction

Uniaxial die and punch were specially designed and manufactured for the compaction process. The prepared composition was placed in the die and punched to form compacts at the room temperature. Santec Automatic hydraulic press was used for a holding time of 1 minute under the load of 100 tonne at 70-75kg/cm². A mixture of molykote powder and kerosene was used as a lubricant, applied as a thin film inside the walls of the die to ensure smooth movement of the punch and easy removal of the compacts after the process was done. To ensure proper compaction and elimination of porosity, the concept of holding time was introduced.

The precursors produced were 36mm in diameter and 11mm in height. The diameter is constant due to same diameter of the die but the height of the same has been calculated based on the rule of the mixture equation. Specific weights/mass of elemental powders are shown in Table 2.

ρ_{Al} be the specific weight of the iron powder (base powder),

w_{Al} be the weight percentage of the iron powder,

$\rho_1, \rho_2, \rho_3 \dots$ be the specific weights of additives and impurities,

$w_1, w_2, w_3 \dots$ be the weight percentages of additives and impurities.

$$d_M = 100 / (w_{Al}/\rho_{Al} + w_1/\rho_1 + w_2/\rho_2 + w_3/\rho_3 + \dots)$$

Table 2.
The table contains the specific weights of the elemental powders, i.e. Aluminium, Silicon, Tin, Magnesium, and Titanium Hydride.

Metal	Specific Weight (g/cm ³)
Aluminium	2.7
Silicon	2.3
Tin	7.3
Magnesium	1.73
Titanium Hydride	3.76

The table contains the total mass of the powder samples along with the theoretical densities for each composition.

SAMPLE CODE	COMPOSITION	TOTAL POWDER MASS (g)	THEORETICAL DENSITY (g/cm ³)
A ₍₁₎	Al-7Si-1Mg + 1 TiH ₂	26.059	2.612
A ₍₂₎	Al-7Si-1Mg + 1 TiH ₂	26.065	2.612
B ₍₁₎	Al-7Si-1Mg-1Sn + 1 TiH ₂	26.152	2.6521
B ₍₂₎	Al-7Si-1Mg-1Sn + 1 TiH ₂	26.003	2.6521
C ₍₁₎	Al-7Si-1Mg-3Sn + 1 TiH ₂	26.672	2.71
C ₍₂₎	Al-7Si-1Mg-3Sn + 1 TiH ₂	26.682	2.71
D ₍₁₎	Al-7Si-1Mg-5Sn + 1 TiH ₂	26.491	2.748
D ₍₂₎	Al-7Si-1Mg-5Sn + 1 TiH ₂	26.536	2.748

The table presents the mass of the precursors after compaction, along with their height, actual density and calculated porosity.

SAMPLE CODE	COMPOSITION	AFTER COLD COMPACTION			
		Compact Mass (g)	Compact Height (cm)	Actual Density (g/cm ³)	Porosity (%)
A ₍₁₎	Al-7Si-1Mg + 1 TiH ₂	25.98	1.12	2.41	7.73
A ₍₂₎	Al-7Si-1Mg + 1 TiH ₂	25.834	1.10	2.441	6.546
B ₍₁₎	Al-7Si-1Mg-1Sn + 1 TiH ₂	26.061	1.12	2.418	8.827
B ₍₂₎	Al-7Si-1Mg-1Sn + 1 TiH ₂	25.961	1.1	2.453	7.507
C ₍₁₎	Al-7Si-1Mg-3Sn + 1 TiH ₂	26.669	1.12	2.474	8.708
C ₍₂₎	Al-7Si-1Mg-3Sn + 1 TiH ₂	26.674	1.10	2.520	7.011
D ₍₁₎	Al-7Si-1Mg-5Sn + 1 TiH ₂	26.474	1.11	2.478	9.825
D ₍₂₎	Al-7Si-1Mg-5Sn + 1 TiH ₂	26.717	1.12	2.479	9.788

D. Foaming Process

This part of process is the final stage where foaming of the precursors was done by placing them in a mold, into a furnace and kept at a desired temperature. The furnace utilised for this process is Swan Equipment Stir Casting furnace with maximum temperature achievability of 1000°C.

The decomposition temperature of the TiH_2 decides the foaming temperature, which was determined by DSC (NETZSCH STA 449F3) testing facility in IIT Madras. The foaming temperature was kept at 725°C but the furnace temperature varies between the range of 730-750°C. The time for foaming was kept constant for all foams i.e. 12 minutes.

The crucible used to contain the precursor, is made of mild steel and took 15 minutes to reach foaming temperature then 12 minutes for the foaming temperature to stabilise. A clearance of 1mm was kept between the mold and precursor. To ensure that compressed air cannot pass through to damage the foam, the mold was sealed off completely. The mold was carefully removed from the furnace after foaming and air cooled using compressed air of 3-4 bars. The air-cooled foam is then removed from the mold and cut using automatic wet abrasive cutting machine to study the morphology of the pores.

E. Characterization

SEM (Scanning Electron Microscopy) with EDS (Energy Dispersive Spectroscopy) was performed to get a closer look at the particles and to study their shape, size and composition. XRD (X-Ray Diffraction) test was done to check the number of constituent present in the mixture by comparing the peaks (phases) which later helped in determining the decomposition temperature of the matrix.

Results and Discussion

A. Thermal property of the foaming agent

Thermogravimetry - Differential Scanning Calorimetry test was performed to determine

the thermal property of the foaming agent and results obtained below in the figure indicates that the decomposition of blowing agent starts at 208°C while the decomposition continues till 627.8°C, the point of maximum decomposition. This shows that the hydrogen is released at this point hence to ensure complete decomposition of titanium hydride we set 725°C as our foaming temperature in the furnace in Figure 2.

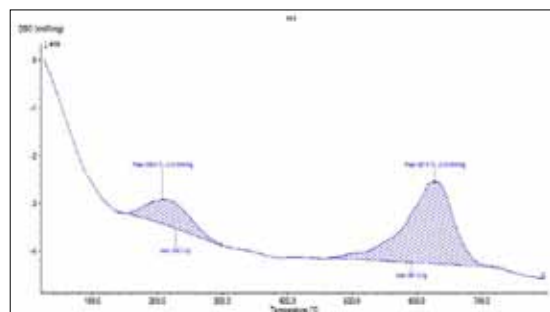


Figure 2: The decomposition peaks of TiH_2 (as received) obtained from TG-DSC graph which shows the maximum decomposition occurring at a temperature of 627.8°C

B. Study of Microstructure

In order to understand and study the microstructure of foaming element, FESEM (Field Emission Scanning Electron Microscopy) test was performed and result obtained is shown in the figures below. Figure 3A shows the microscopical image of Tin at the magnification of 5000x. The shape of the particle so obtained is spherical. The average size of all the particles is 13.5299 μm . Figure 3B shows the image of pure aluminium at the magnification of 2500x and the shape is irregular and spherical. 3C and 3D show the image of Silicon and Titanium Hydride with the magnification of 2500x and 1000x respectively. The results of FESEM were used to set up the mixing procedure, speed (120-140 rpm) and time (30 minutes) along with the compaction pressure (70kgf/cm²). It also helped us to check whether the provided sample is satisfactory or not and to determine the decomposition temperature of the particles. SEM images of samples are shown in Figure 3 and 4.

INVESTIGATION ON THE EFFECT OF TIN ADDITION ON FOAMING BEHAVIOUR OF Al7SiMg PRODUCED BY POWDER ROUTE

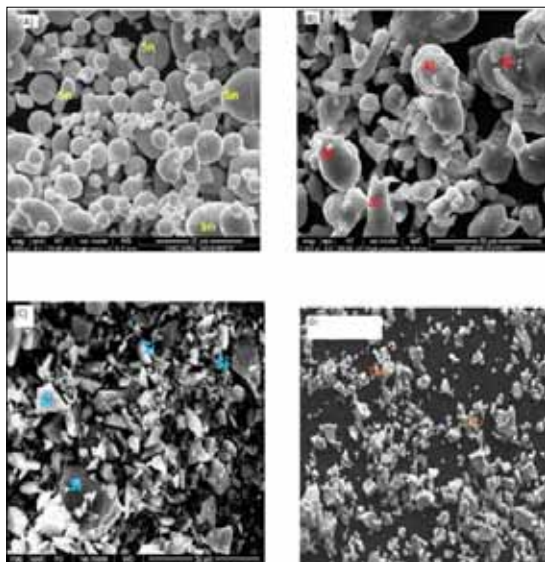


Figure 3: SEM images of (A) spherical shaped Tin particles magnified at 5000x, (B) irregular shaped Aluminium particles magnified at 2500x (C) Granular shaped Silicon powder magnified at 25000x (D) Irregular shaped Titanium Hydride magnified at 1000x

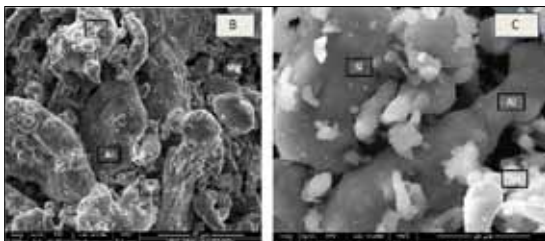


Figure 4: SEM images of different samples (B: Al-7Si-1Mg-1Sn-1TiH₂ and C: Al-7Si-1Mg-3Sn-1TiH₂) indicating the elements Al, Si, Mg, Sn, TiH₂ magnifications 2000x and 5000x.

Figure 5 depicts voids in the compacts. To obtain the image, first the precursor is cut in two halves using Wire EDM and then polished using 400, 600, 800 and 1000 grade obtained in the emery sheets to get a fine finish. After getting a fine finish, the precursor is observed under the microscope and black marks seen in the figure below are the porosities present in it.

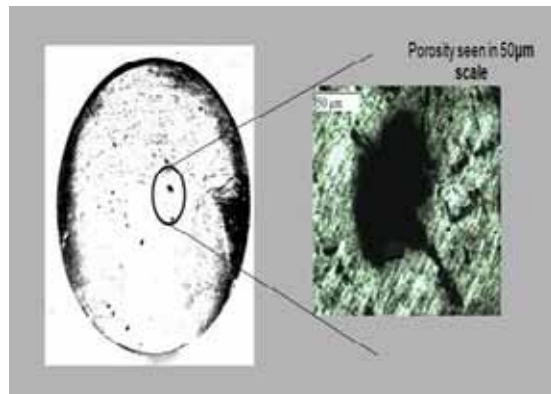


Figure 5: The optical image of a precursor, indicating the presence of voids.

C. Phase analysis

The different phases of elements were identified by recognising the peaks of certain phases using XRD (X-Ray Diffraction). Figure 6 and Figure 7 shows the result obtained by XRD testing of Aluminium and Titanium Hydride respectively and represents the various phases present in the respective powders. The peaks are then compared with the peaks of the standard image to find whether the provided sample is pure or not which also help us to ensure the decomposition temperature of the elements.

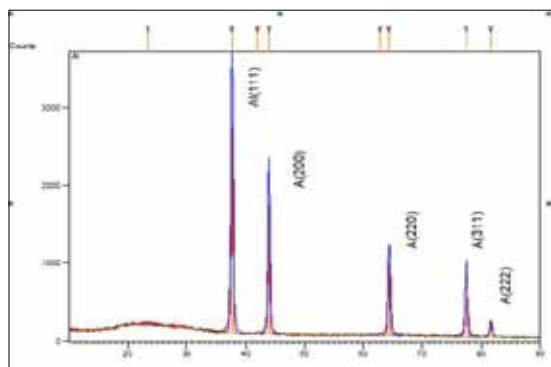


Figure 6: XRD analysis of Aluminium indicating the various peaks of elemen

INVESTIGATION ON THE EFFECT OF TIN ADDITION ON FOAMING BEHAVIOUR OF Al7SiMg PRODUCED BY POWDER ROUTE

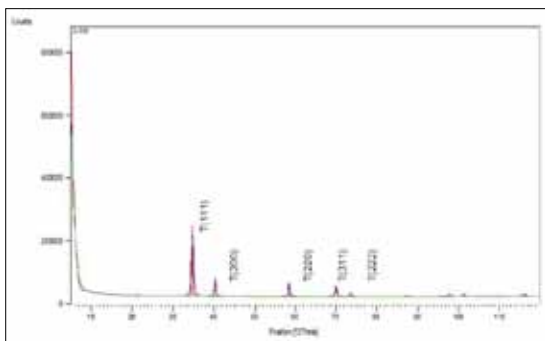


Figure 7: XRD analysis of TiH_2 as received powder indicating various peaks of element.

XRD analysis of various samples is shown in Figure 8.

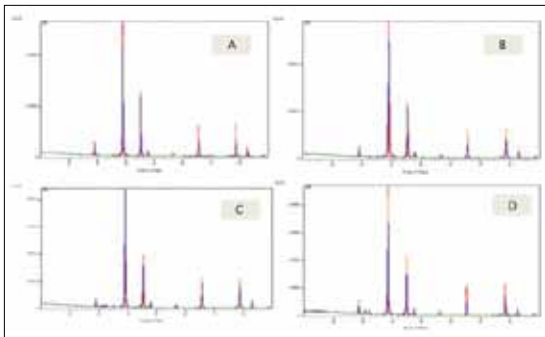


Figure 8: XRD Analysis of various samples (A: Al-7Si-1Mg-1 TiH_2 , B: Al-7Si-1Mg-1Sn-1 TiH_2 , C: Al-7Si-1Mg-3Sn-1 TiH_2 , D: Al-7Si-1Mg-5Sn-1 TiH_2) confirming the constituents of different compositions

D. Particle Size Analyzer

The size of the particles was determined by particle size analysis. This process makes use of laser diffraction by measuring the angular variation in intensity of light scattered as a laser beam passes through the particulate sample. The result is given below in the figure shows the percentage of the particles passing through channel which is used to find the size of the particle. It shows the particle size analysis is of Titanium Hydride which is $12.32\mu\text{m}$. By finding the size of the particles we were able to set the mixing procedure with its speed and time as shown in Figure 9.

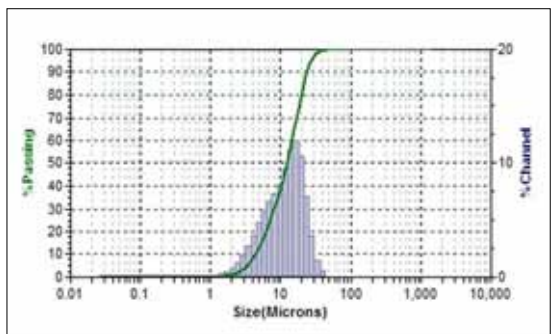


Figure 9: In this image, the particle size analysis of Titanium Hydride is shown. As per D_{50} standard the size of the particle is $12.32\mu\text{m}$.

E. Elemental Analysis

The elemental analysis of the particles is done by EDS (Energy Dispersive Spectroscopy). The figure depicts the EDS of Al-7Si-Mg-1 TiH_2 , which shows the presence of Aluminium, Silicon, Magnesium and Titanium. It detects even the smallest of impurity present in the sample and plays an important role in determining the foaming temperature as the presence of every element in the composition has its effect on foaming temperature. In this case the decomposition temperature of Titanium Hydride is 627°C and the melting temperature of Aluminium is 660°C hence 725°C as our foaming temperature as shown in Figures 10 & 11.

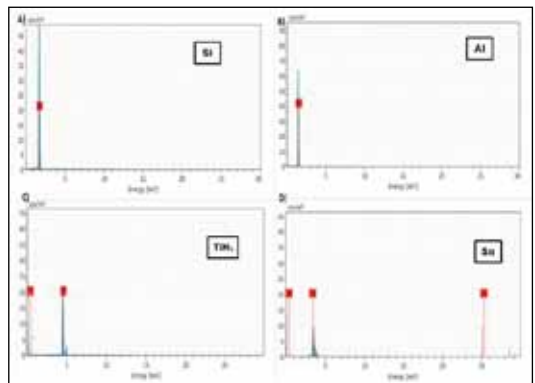


Figure 10: EDS analysis elemental samples of powders (A)-Si, (B)- Al, (C)- TiH_2 , (D)-Sn

INVESTIGATION ON THE EFFECT OF TIN ADDITION ON FOAMING BEHAVIOUR OF Al7SiMg PRODUCED BY POWDER ROUTE

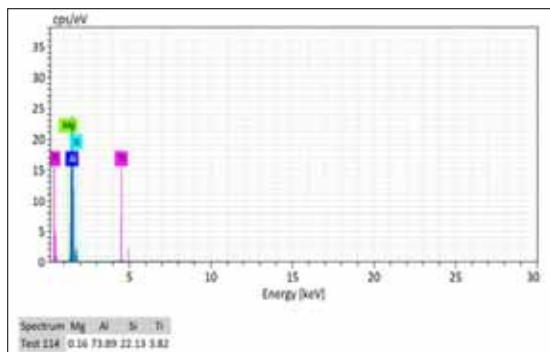


Figure 11: EDS of Al-7Si-1Mg 1 TiH_2 confirming the presence of all the element of the composition.

F. Determination of porosity, linear expansion coefficient and relative density

Since the precursor and mold has the same diameter the expansion will occur in only the direction of height. After foaming, the samples were removed from the furnace and rapidly cooled in the air to solidify. The mass and geometry were used to calculate the density of the precursors and foams. Hence, relative density of precursors and foams (ρ_R), linear expansion (α_{LE}) and porosity of foams (P) were calculated using the following equations:

$$\rho_R = (\rho_1 / \rho_2) * 100\%$$

$$\alpha = (h_1 / h_2 - 1) * 100\%$$

$$P = 1 - (d_f / d_m)$$

Where

ρ_1 and ρ_2 are densities of precursor or foam and bulk aluminium, respectively;

h_1 and h_2 are heights of foam and precursor, respectively. In porosity calculation d_f and d_m are the densities of foam and density of precursor. It is noteworthy that, for the calculations of the linear expansion of foam, as the expansion occurred in an uneven manner, the top surface was not entirely flat. Therefore, the height measurements were taken from multiple sides and the final heights used in the calculation were the average of multiple readings.

Table 3. The table refers to the calculated values of porosity, linear expansion and relative density of the foams.

SAMPLE NUMBER	POROSITY (%)	LINEAR EXPANSION (%)	RELATIVE DENSITY (%)
A ₍₁₎	39.499	82.589	62.06
B ₍₁₎	17.46	80.357	83.54
C ₍₂₎	42.287	110.09	62.06
D ₍₂₎	23.49	185.35	77.59

Conclusions

The maximum expansion of the foam is observed in sample D (185.35%). This has occurred because of improper tightening of foaming mould due to which air might have escaped in the mould during cooling. This results in a hollow gap at the bottom of the foam. The maximum porosity is achieved in sample C (42.287) where some pores are seen uniform whereas many others are damaged due to coalescence. Compaction pressure was in the range of 70-75 kgf/cm² to avoid porosity in the precursors. However, the porosities could still be seen after cutting the precursor using image analyser. These pores could have been avoided using a hot die compaction method. In hot die compaction, tin would have sintered the matrix, reducing the amounts of pores.

It was found that tin has played a key role in TiH_2 dissociation, and modification of liquid Al's surface tension.

Pore structures are more uniform as the percentage of Tin is increased. But at 5% Sn the pores are not seen due to coalescence amongst the pores. So the maximum 3% of Sn is required to make proper Al foams.

References

1. Lydia Y. Aguirre Perales, *On the stabilization of Aluminum foams by Tin additions and in situ intermetallic formation*, McGill University, August 2014

INVESTIGATION ON THE EFFECT OF TIN ADDITION ON FOAMING BEHAVIOUR OF Al7SiMg PRODUCED BY POWDER ROUTE

2. Isabel Duarte and Monica Oliveira, *Aluminium Alloy Foams: Production and Properties, Portugal, March 2012*
3. L Wang, Z S Hua, J Ma & G C Yao (2011) Effects of Mg addition on foam stability of Al foams made by powder metallurgy route, *Powder Metallurgy*, 54:3, 385-388
4. Behzad Nayebi, Characteristics of dynamically formed oxide films in Aluminium-Calcium foamable alloys, *Journal of Alloys and Compounds* 655(2016) 433e441
5. Xiangyang Zhou, Xiquan Liu, Jie Li, and Hongzhuan Liu, Novel foaming agent used in preparation process of Aluminium foams, *Journal of University of Science and Technology*, December 2008

DESIGN, FABRICATION AND APPLICATION OF IN-HOUSE, ON-LINE GREEN-DEBURRING MACHINE

Jash Vora, Harish Chaudhari

Speciality Sintered Products Pvt. Ltd. Shirwal, Maharashtra, India

Abstract : As much as the powder in Powder Metallurgy is crucial, it's presence on green, formed parts as burrs, in however low the percentage, is least appreciated. The Company's constant effort towards minimizing burr on green, formed parts, had created the necessity to conceptualize, design, fabricate, analyze and commission an in-house deburring machine that can be easily transported and utilized on any of the forming presses. The focus of this paper is mainly on achieving the goal of a pocket-friendly, easy in construction machine that is now on shop-floor deburring entire machine output and thus saved 280 man hours. Deployment of the mentioned machine also eliminated double banking of formed parts and reduced the lead time per part by 12 hours which increased the productivity. In addition to this, the machine saved labour charges spent towards buffering each part by hand.

Introduction

In the modern days of 21st Century, it is surprising that we still are dealing with a problem as small as burrs. These little things have cost millions to OEMs and other PM Companies in the form of dimensional distortion, die marks, tool damage, and production losses in general^[1]. As a result of these consequences, there arises the question of removal of burrs from the products. This paper focuses on one such method of removing burrs from green parts- Green Deburring. It was the first time that it was attempted and implemented on the shop floor of a growing PM company in the form of green deburring in the month of August 2018. Deburring of larger workpieces by mechanical methods can generally be effective and not so expensive^[2]. The experimental part aims at finding the right combination of belt speed, brush type and speed, and brush engagement in order to achieve burr-free parts that are acceptable to meet client quality standards. As an addition to this, the process completely eliminated double banking of the formed parts and increased the productivity of the plant. The analysis of this experiment is so done by putting test batches through entire production process and test for flicker as a measuring parameter for effective working of the machine. Additionally, the analysis included finding out production schedules, logs and deducing how did the manual deburring and

machine deburring differ time-wise to find out the banking time and the lead time between forming and sintering processes.

Working Model

The model that was designed, fabricated and installed in-house had simplistic ideas and easy-to-maintain principles which include a flipping mechanism, which uses the part's inertia, in order to brush the parts from both the sides. Primarily, the machine includes 4 main features as shown in Figure 1:-

- A. Conveyor Belt
- B. Brushing Stations
- C. Flipping Mechanism
- D. Electrical Control Panel

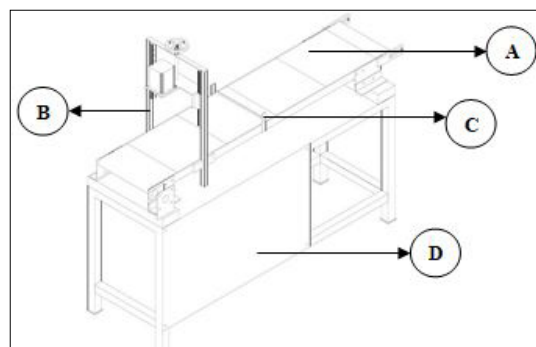


Figure 1: Partial AutoCAD 3D Sketch of Green Deburring Machine

A. Conveyor Belt

The function of conveyor belt is to transport the parts from forming press to one brushing station and then to the next. The conveyor length was so calculated to be 1500mm to include spacers for parts to slide from forming press to the conveyor without any interference between 2 consecutive parts as well as to match the forming cycle time (~8s). Conveyor belt type was also carefully selected to be a canvas belt that transmits magnetic field to hold the parts while undergoing brushing.

B. Brushing Station

The brushing stations are designed keeping in mind the bandwidth of the part height that can be brushed on this machine. With adjustable rail-and-guideblock assembly, user has it easy to raise and lower the brush as required. Due to relatively low requirement of rotational speed (<1440rpm), stepper motors have been installed over a cross plate which is bolted to the guide block. The rail is in turn bolted to a rectangular frame that is consequently bolted to the main conveyor-belt bed frame. This construction restricts any vibrations that may disrupt the functioning of the machine. In order to adhere the part onto the moving conveyor, a permanent magnet has been fixed onto the conveyor bed frame.

C. Flipping Mechanism

Firstly, flipping is required in order to brush the other side of the parts to avoid warpage issues whilst sinter-hardening the components. The mechanism that has been adopted is quintessentially the usage of physics. This mechanism plainly comprises of a loose elastic strip tied across the conveyor and of cable-tie strips glued onto the conveyor at fixed distance. The moving part, after coming into contact with the strip, stretches the elastic and uses its' kinetic energy to increase the potential energy of the elastic. Once the part is blocked on the cable-tie strip on the conveyor, this potential energy of the elastic, when goes over the part's inertial

force, cause to flip the component. Owing to the high density of the part and the flexibility of the conveyor belt, the part is free of any damage, dent, crack and breakage. Thus, physics is the driving force behind carrying out the flipping of components (Refer Figure 2(a)-2(d)).

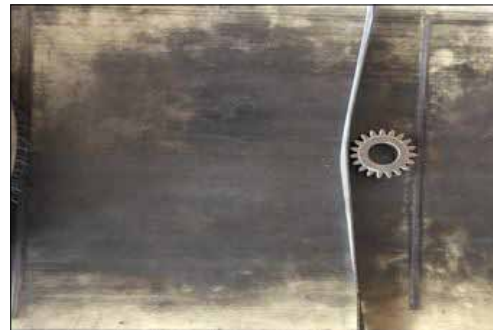


Figure 2 (a): Initiation of Increase in Elastic Strip's Potential Energy

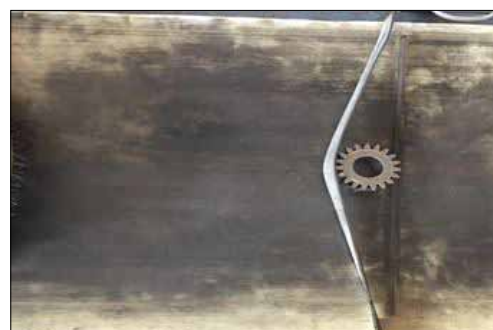


Figure 2(b): Potential Energy of Elastic Strip Greater than Inertial Force and Weight of Part

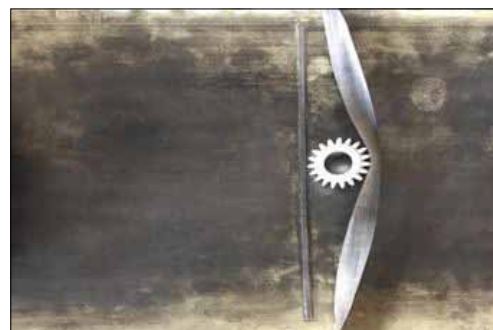


Figure 2(c): Decreasing Potential Energy of Elastic Strip after Flipping the Part



Figure 2(d): Release of Part; Ready for 2nd Side Deburring

D. Electrical Control Panel

The control panel is evidently the engine of this machine. The high output machine has relatively a basic control panel comprising of bare minimum parts as listed below:-

1. Programmable Logic Controller(PLC)
2. Stepper Motor Drives
3. Power Supply Switches
4. Transformer
5. Switch-Mode Power Supply(SMPS)

Experiment Setup

Experiment batch specifications are given in Table 1. This experiment/trial is focused on deburr the parts on-line, eliminating double banking of green parts, reducing the lead time of finished product, reducing cost of manufacturing the product and to increase the quality of the product. The setup used in this experiment is decided on the basis of actual production on the press machine with an aim to synchronize the conveyor belt speed with that of part production rate. Another crucial part of the machine set-up was to arrange the brush at a height that is 1-1.5 mm below the top surface of the part. Setting of brush is an important aspect because higher engagement leads to higher torque requirement on the brushing motor and might lead to overheating of the motor or just jam the motor or, more importantly, may alter the dimension of

the soft, formed part. On the contrary, lower the engagement, lesser would be the friction and cutting action between brush and the burr on parts. Brush speed setup was made keeping in mind the effectiveness of burr removal. Slower brush speeds would induce a lesser cutting action and higher speeds will cause skirting of bristles (Figure 3) and reduce the overall brushing effectiveness.



Figure 3: Picture Showing Skirting of Brush Rotating at 425 rpm

Table1: Experiment Batch Specifications.

Batch #	Brush Specification	Convey or Belt Speed	Brush Rotational Speed	Qty .
1a	Ø250 mm, 320 SiC Grit Size, 1" Trim Length	2800 mm/min	325	50
1b	Ø250 mm, 320 SiC Grit Size, 1" Trim Length	2800 mm/min	350	50
1c	Ø250 mm, 320 SiC Grit Size, 1" Trim Length	2800 mm/min	375	50
1d	Ø250 mm, 320 SiC Grit Size, 1" Trim Length	2800 mm/min	400	50
2a	Ø250 mm, 320 SiC Grit Size, 1" Trim Length	2800 mm/min	325	50
2b	Ø250 mm, 320 SiC Grit Size, 1" Trim Length	2800 mm/min	350	50
2c	Ø250 mm, 320 SiC Grit Size, 1" Trim Length	2800 mm/min	375	50
2d	Ø250 mm, 320 SiC Grit Size, 1" Trim Length	2800 mm/min	400	50

DESIGN, FABRICATION AND APPLICATION OF IN-HOUSE, ON-LINE GREEN-DEBURRING MACHINE

Taking into consideration the deburring machines currently available, Silicon Carbide abrasive filament brushes of 2 grit sizes were shortlisted for the experiment- 240 and 320. As recommended by the company manufacturing SiC brushes, the maximum effective speed of the brushes is 325-350 rpm. Consequently, 4 speeds- 325, 350, 375 and 400 rpm- were selected to conduct trials. Thus, the experiment contained 4 batches; each of 50 parts. Such batches were repeated for the two different kinds of brushes. The brushed parts were then made to follow the exact manufacturing process as regular parts to study and compare the effectiveness of the new brushing machine. The Process Flow Diagram (PFD) is shown in Figure 4.

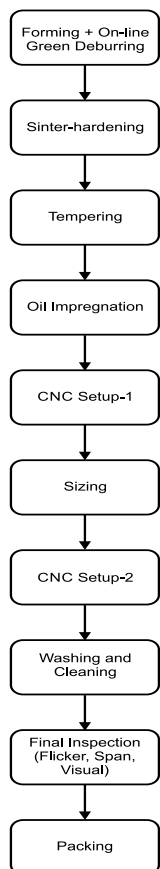


Figure 4: Process Flow Diagram of SSPL Part

The measurement of effectiveness of this machine is the number of parts tested under flicker-testing machine and marked as okay. Data were collected for each part and the trend of flicker test results are plotted for each part. Reasons other than burr for rejection in flicker testing machine are also pointed out in further segment.

Results and Conclusions

As mentioned earlier in Table 1, the 8 batches in total were made to conduct the trials. The results of this trial are categorized in 3 of the following segments:-

1. Timing
2. Quality
3. Cost

1. Timing

Timing is an important factor to consider while evaluating the performance of the machine. Not only the cycle time of deburring parts is crucial but also the time that it helps in cutting back on the manufacturing process. Before the deployment of this machine on the floor, the compacted parts were stored and scheduled to be hand deburred which increased the storage requirement and had irregular schedules to hand-deburr them. It was noted from the production logs that it consumed nearly 12-14 hours or even more to complete the manual deburring process and yet again, had to wait to be released for sinter-hardening process. However, after deployment of the machine on the shop floor, hand deburring process was completely eliminated thus saving the company a considerable amount of time taken to deburr 1000+ parts by hand at an average speed of 3 parts per minute and cut down the extra 12-14 hours taken to hand-deburr the components. When the deburring machine was connected to the forming machine, in spite of increasing the complete forming cycle time by approximately 30s, it added a completely new process with

DESIGN, FABRICATION AND APPLICATION OF IN-HOUSE, ON-LINE GREEN-DEBURRING MACHINE

increased effectiveness and reduced cost. Mentioning of rate of brushing, this machine has a running capacity of upto 60 parts per minute; that is, it can withstand forming loads of upto 7 machines per minute.

2. Quality

Towards the end of all physical processes, trial parts were put to test on the flicker and DFCE testing machine. It was observed that as the speed increases, the number of parts rejected in the flicker test decreases and a maximum acceptance increased from 66% to 86% as illustrated in Figures 5 to 13. The trend ahead was such that as the brush rotation speed goes beyond the recommended speed, the rejection increased and the acceptance percentage went down to 64%; which in turn supports the theory suggested in the experiment setup section. This trend was observed in both the types of brushes indicating that the average value of flicker goes on decreasing to a lowest of $9.04\mu\text{m}$. Following series of graphs exemplify the theory clearly. As a part of conclusion, batch number 1c and 2b showed the highest acceptance percentage with respect to flicker test- about 85%. This brings us to a conclusion that the ideal range of brush is 350rpm-375rpm with the belt speed at 2800mm/min and 1.5mm engagement with parts.

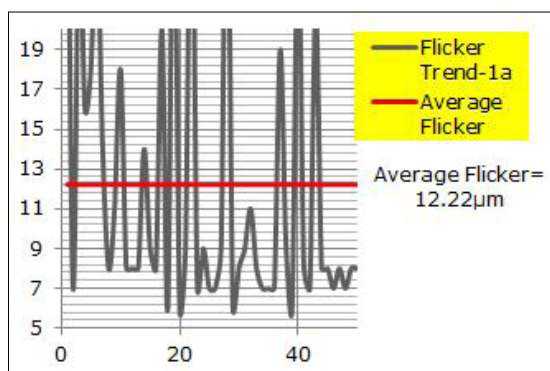


Figure 5: Flicker Trend of batch 1a

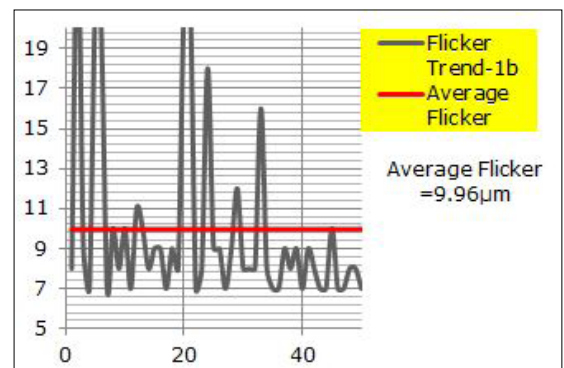


Figure 6: Flicker Trend of Batch 1b

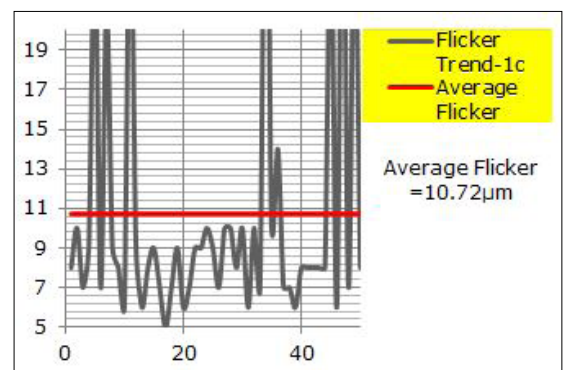


Figure 7: Flicker Trend of Batch 1c

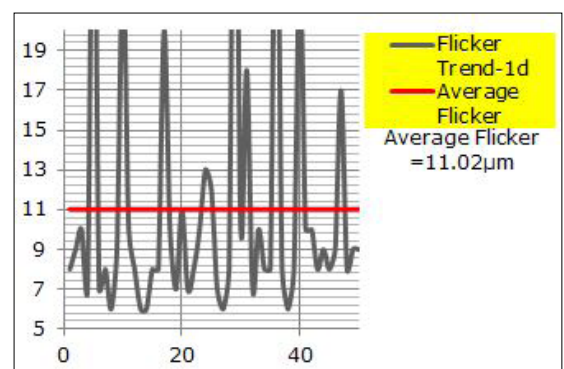


Figure 8: Flicker Trend of Batch 1d

DESIGN, FABRICATION AND APPLICATION OF IN-HOUSE, ON-LINE GREEN-DEBURRING MACHINE

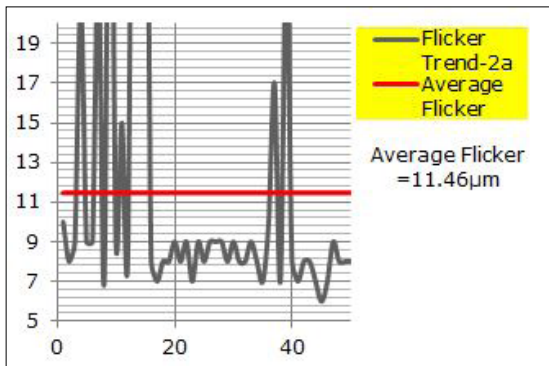


Figure 9: Flicker Trend of Batch 2a

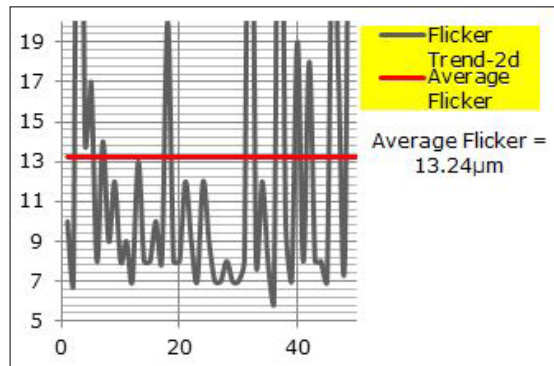


Figure 12: Flicker Trend of Batch 2d

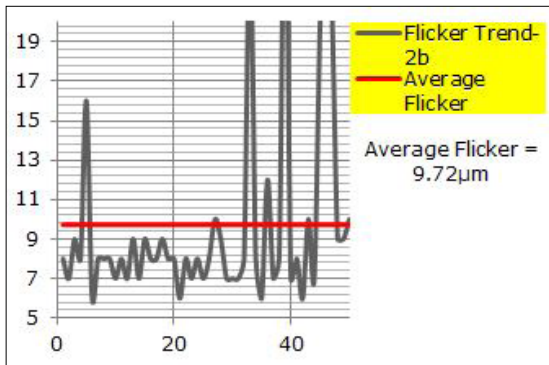


Figure 10: Flicker Trend of Batch 2b

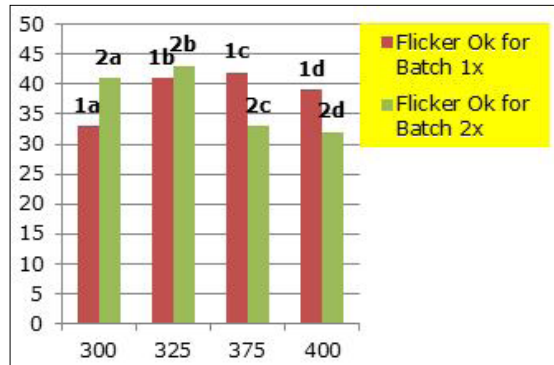


Figure 13: Number of Parts (Out of 50) Accepted in Flicker Test

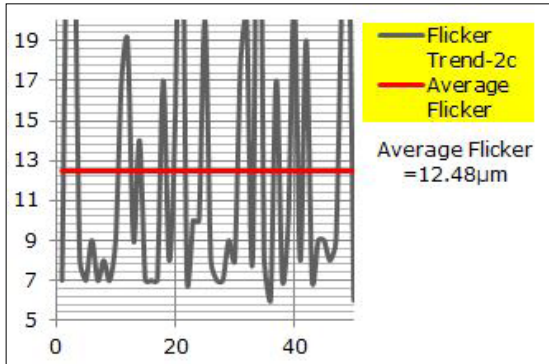


Figure 11: Flicker Trend of Batch 2c

3. Cost

The crucial point of the entire project is the cost. Most of the thought process directs towards saving cost and cutting down the manufacturing cost of the finished product. After this machine was attached on the compaction machine, the cost of extra labour was totally eliminated and that, in turn, cut the cost by 5% and increased productivity by 280 man hours. As opposed to other machines available in the market, this machine has a total cost of just about 25%. Addressing the question of maintenance, the most time-consuming activity would be changing of brushes after wear out. But, even that, it was

recorded that after brushing 200 parts under a particular brush, the wear-out percentage was observed to be only 2.5% for 240 grit size brush and a mere 1% for 320 grit size brush. In other words, theoretically, the 240 grit size brush can debur nearly 18,000 parts and 15,000 parts for 320 grit size brush before requiring a change.

Recommendation for Future Work

It is a clear indication from the earlier parts that there is a considerable scope of improvement in this project. Not 100% parts were accepted from the flicker test majorly due to cleanliness issue. Streamlining the processes and planning one action immediately after the other will reduce the chances of dirt and dust settling onto the parts due to banking between processes. Another synchronization that can be achieved is between the sintering furnace belt and the forming machine through this conveyor belt through an automated material handling system. This scope of the machine is already executed and is being tested at SSPL to eliminate handling of green parts from the 800T press machine to a fully loaded 10-zone sintering furnace. This is the first time that such an attempt has been made on such an extensive scale in India. Furthermore, a flipping mechanism is also installed and is in trial mode to flip the green parts to attain a burr-free part on both the sides. Following series of pictures display the new material handling system in testing stage Figures 14 to 17.



Figure 14: Deployment of Deburring Machine On-Line for SSPL Part



Figure 15: Initiation of Part Flipping



Figure 16: Completion of Part Flipping



Figure 17: Transfer of Parts onto Sintering Furnace Loading Belt with Pusher Mechanism

Acknowledgements

The authors wish to thank the entire team of Speciality Sintered Products Pvt. Ltd., especially, Mr. Niranjan Narkhede to encourage us to push the boundaries and provide the technical support to make this experiment a possibility. Also, they wish to thank the entire Production Department to welcome this additional unit with great appreciation.

DESIGN, FABRICATION AND APPLICATION OF IN-HOUSE, ON-LINE GREEN-DEBURRING MACHINE

Reference

1. Dornfeld, David, 2004, "Strategies for Minimization and Prevention of Burr Formation", Consortium on Deburring and Edge Finishing, University of California, Berkeley
2. Gillespie, L.K.: Deburring and Edge Finishing Handbook (1999) SME, USA

MACHINABILITY OF LOW-ALLOYED PM STEELS

Walter Xu, Ulf Engström, Marcus Persson*

Höganäs (China) Co., Ltd, *Höganäs Sweden AB

Abstract : Though powder metallurgy offers near net-shape manufacturing capability, many components often require surface-finish machining to reach final shape due to particular geometries and finer tolerances. To achieve the best possible machining economics, different demands on the machinability are required as various types of PM materials and manufacturing processes. Drilling and turning are the most common in PM, in which machinability additives are often added and give a positive impact on tool wear and tool life. Since PM technology allows many different alternatives of machinability additives, there is large room for continuous improvement on the market. This paper evaluated the machinability of as-sintered steels manufactured from different commercial low-alloyed iron powder grades and machining additives. The influence of powder grades, machining additives, cutting parameters and tool materials in both drilling and turning are described.

Introduction

PM is a well-established production technology of large series of complex components to very close tolerances. Many PM components require some type of machining operation to reach final shape, e.g. shapes impossible to create with the compaction exclusively, or due to demands for even higher tolerances, e.g. roundness of holes. PM materials are often considered to be difficult to machine, especially compared to conventional standard steels. However, by choosing a suitable combination of tool material and tool geometry together with optimized cutting data and machining additives, it is in many cases possible to achieve a productivity level of machining PM parts similar to that of standard steels.

Machinability Experiments

Mixes based on three different base powders were made to show how different microstructures affect machinability, both with and without addition of machinability additives. Table 1 is showing the different base powders and Table 2 the mix compositions.

Table 1. PM Base Powders

Base Powder	Composition
AHC100.29	Water atomized pure iron powder
Distaloy AE	Iron powder, diffusion alloyed with 1.5%Cu, 4%Ni and 0.5%Mo
Astaloy® CrM	Water atomized iron powder pre -alloyed with 3%Cr and 0.5%Mo

Table 2. Mix Composition

Powder Mix	Abbreviation
AHC100.29 + 2% Cu + 0.8% Graphite + 0.6% Lube E	AHC
AHC100.29 + 2% Cu + 0.8% Graphite + 0.6% Lube E + 0.3% MnS	AHC-S
AHC100.29 + 2% Cu + 0.8% Graphite + 0.6% Lube E + 0.15% MnM	AHC-M
Distaloy AE + 0.5% Graphite + 0.6% Lube E	AE
Distaloy AE + 0.5% Graphite + 0.6% Lube E + 0.3% MnS	AE-S
Distaloy AE + 0.5% Graphite + 0.6% Lube E + 0.15% MnM	AE-M
Astaloy CrM + 0.55% Graphite + 0.8% Lube E	CRM
Astaloy CrM + 0.55% Graphite + 0.8% Lube E + 0.3% MnS	CRM-S
Astaloy CrM + 0.55% Graphite + 0.8% Lube E + 0.15% MnM	CRM-M

The above powder mixes were compacted into drilling test specimens Ø80 x 28 mm and turning test specimens Ø64/35 x 30 mm with green density of 7.0 g/cm³.

AHC100.29 and Distaloy AE specimens were sintered for 30 minutes at 1120°C in 90/10 (N₂/H₂) atmosphere. Astaloy CrM specimens were sinter hardened for 30 minutes at 1120°C in 90/10 (N₂/H₂) atmosphere. Cooling rate of sinter hardening was 1.5°C/second and directly after the specimens were tempered at 200°C in air for 60 minutes.

The drilling and turning machinability tests were performed in a CNC lathe as illustrated in Figures 1 to 3. The drilling machinability criterion was to drill as many holes as possible before total drill failure – complete breakage or extreme heat release. The turning machinability criterion was to turn a total distance that corresponding to a predefined flank wear (V_b) at a chosen cutting speed with certain time.

MACHINABILITY OF LOW-ALLOYED PM STEELS

Results

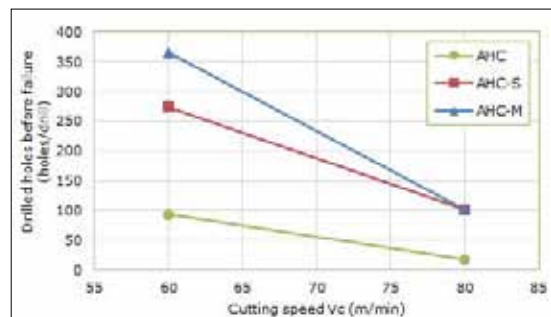


Figure 1: Drilling machinability of as-sintered AHC100.29 with or without additives
Drilling parameters: Dormer A002, $f=0.06$ mm/rev, $ap = 9.6$ mm (blind), dry

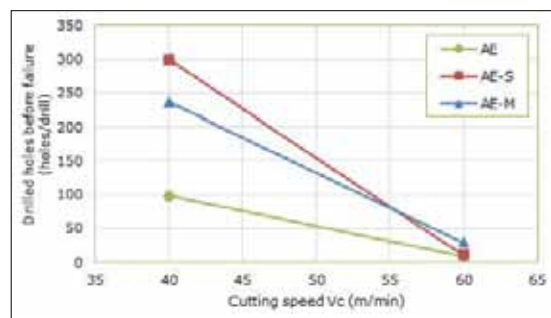


Figure 2: Drilling machinability of as-sintered Distaloy AE with or without additives
Drilling parameters: Dormer A002, $f=0.06$ mm/rev, $ap = 9.6$ mm (blind), dry

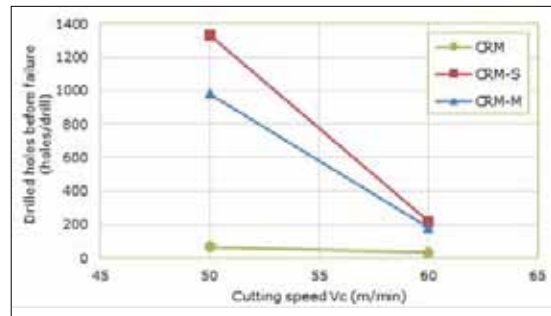


Figure 3: Drilling machinability of sinter-hardened Astalloy CrM with or without additives
Drilling parameters: Dormer R002, $f=0.06$ mm/rev, $ap = 9.6$ mm (blind), dry

The result of turning machinability will be shown in presentation.

Conclusions

The machinability enhancing additive MnS works overall very well to improve machinability of sintered PM steels ranging from low hardness structures to extremely difficult sinter hardened materials in both drilling and turning operations. The machinability improvement obtained by the new additive MnM is comparable to MnS both for drilling and turning operations but it has greater impact on machinability of Fe-Cu-C and diffusion alloyed materials. With the new additive the amount can be reduced a half without losing the machinability.

Keywords: Machinability, Turning, Drilling, Additives, PM steels

RECONSTRUCTION OF THE ALVEOLAR BONE USING BONE AUGMENTATION WITH SELECTIVE LASER MELTING TITANIUM MESH SHEET

Hiroyuki Nakano, Ayano Ogura and Takaaki Ueno

Department of Dentistry and Oral Surgery, Division of Medicine for Function and Morphology of Sensory Organs, Osaka Medical College, Takatsuki-city Osaka, Japan

Abstract : With the increasingly widespread use of dental implants, bone augmentation for high-grade alveolar bone resorption is being implemented using a variety of methods. Adequate structural base of osseous tissue is necessary for supporting dental implant. Bone augmentation is needed to make the space before the embedding, if there are insufficient bone volumes in the alveolar bone. Bone augmentation method using space-making device is used to create space in the defect area, and the bone is augmented using autologous bone or artificial bone material such as hydroxyapatite or calcium phosphate. Commonly used materials for conventional artificial space-making device include absorbent material such as collagen, and mesh-like, thin, flat titanium (Ti) that is manually adapted to fit the shape of the bone defect. However, adapting a flat titanium mesh sheet to complex bone defect areas comprising curved and flat surfaces requires a large amount of effort. In an attempt to simplify this process, we have been using a selective laser melting (SLM) Ti protocol to adapt the titanium mesh sheet to bone defects. Use of SLM to modify the Ti mesh sheet enables accurate shaping of the sheet to morphologically complex alveolar bone defects, which both shortens surgery duration and enables accurate augmentation of the bone form. The aim of this report was to present the clinical feasibility of bone augmentation using SLM Ti mesh sheet.

Materials and Methods

Material simulation

Preoperative surgical simulation was implemented based on the number of implants and the embedding angle of the dental implants, as determined using BioNa® three-dimensional image analysis software (Wada Precision Dental Laboratories Co. Ltd., Osaka, Japan) and Digital Imaging and Communications in Medicine (DICOM) data obtained from computed tomography (CT). The bone shape and volume required at the implant embedding site were calculated based on this simulation, and the Ti mesh sheet was designed on a computer. The simulated Ti mesh sheet was then converted into data in a Standard Triangulated Language format. The mesh sheet was placed into a metal laminate molding apparatus, and the molding position was determined within the modeling range by the onboard internal software and metal additive manufacturing machine EOSINT M 270 (EOS GmbH Electro Optical Systems, Krailling,

Germany). Pure Ti powder was scattered onto the shaping sheet and moved with a laser light, following the two-dimensional data for each layer with respect to the molding position and modeling shape; only the powder irradiated by the laser light was selectively melted and coagulated into a 30- μm -thick layer. This process was repeated to fabricate Ti mesh sheet 0.3 mm in thickness shaped to the simulated design (Fig. 1).

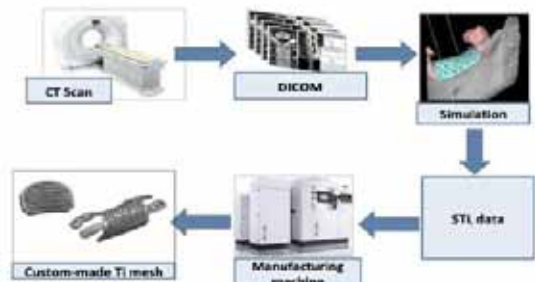


Fig. 1

RECONSTRUCTION OF THE ALVEOLAR BONE USING BONE AUGMENTATION WITH SELECTIVE LASER MELTING TITANIUM MESH SHEET

Case Reports

The patient was a 50-year-old female who had lost her maxillary central incisors and surrounding alveolar bone through trauma to the anterior maxilla. The design simulation was created from the preoperative CT images, and a 0.3-mm-thick porous Ti mesh sheet was fabricated according to the method detailed above. An incision was made in the gingival periosteum, and the mucoperiosteum flap was reflected to reveal the bone defect (Fig. 2A). There was bone loss in both the vertical and buccal directions corresponding to the defect seen on the preoperative CT scan (Fig. 2B). The SLM Ti mesh sheet was trial-fitted to the defect, and there was sufficient agreement (Figs. 2C, D). The dental implant (Bränemark System® MKIII Groovy RP 3.75×13mm, Nobel Biocare, Zurich, Switzerland) was embedded into the remaining alveolar bone, and artificial bone13 (Bio-Oss®; Geistlich Pharma, Wolhusen, Switzerland) was infiltrated into the space between the residual bone and the fixed SLM Ti mesh sheet using a 1.0- × 6.0-mm micro-screw (KLS Martin Group, Tuttlingen, Germany). The mucoperiosteum was then sutured

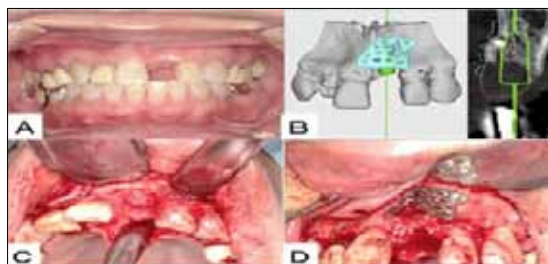


Fig. 2

Postoperatively, the mucous membrane was healthy. Six months after surgery, clinical examination of the patient revealed that the mucosa remained healthy and that the bone condition was sufficient (Figs. 3A, B); bone morphology under the Ti mesh sheet was confirmed on CT images (Figs. 3C, D). After

considering the situation, we decided that retraction of the gingiva to remove the SLM Ti mesh sheet would influence mucosal volume, so the SLM Ti mesh sheet was left embedded to maintain aesthetic appearance. The patient is currently free of any gingival malformations.

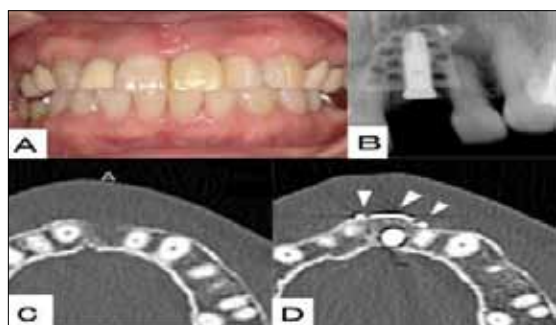


Fig. 3

Discussion

Bone augmentation is a method aimed at increasing bone mass through use of artificial bone or an autologous bone graft to compensate for the bone defect at sites where implants cannot be inserted due to vertical or horizontal bone resorption of the jaw bone. The three-dimensional space-making device was secured over the empty spaces in the compensated artificial or autologous bone grafts. The device can be categorized into two categories: absorbent sheet and nonabsorbent sheet; comparisons have shown that nonabsorbent sheet composed of metals such as Ti are superior to absorbent sheet composed of collagen because of their ability to retain their three-dimensional morphology. However, the task of applying and adapting a nonabsorbent metallic sheet to a wound depends on the operator's skill and experience; lack of experience may slow down the process and lead to extended duration of the procedure. Use of SLM titanium mesh may help solve operator issues related to conventional Ti meshes sheet.

RECONSTRUCTION OF THE ALVEOLAR BONE USING BONE AUGMENTATION WITH SELECTIVE LASER MELTING TITANIUM MESH SHEET

In the case report, SLM of the Ti mesh sheet resulted in dramatically superior form fitting of the alveolar bone defect area. The SLM Ti mesh sheet fit well to the surrounding tissue immediately after implantation, and there was a complete absence of postoperative inflammation. In conventional surgery with Ti mesh, multiple pins are required to fix it in place. In contrast, we found that the SLM Ti mesh sheet was extremely stable after being passively fitted to the alveolar bone, and only one pin was required to fully fix the mesh in place. Sumida et al. reported that the average number of screws used to maintain the space-making device was 1.31 for the custom-made Ti mesh sheet group and 3.23 for a conventional Ti mesh sheet group; this difference was statistically significant. The stiffness of the Ti mesh sheet may result in mechanical irritation of the mucosal flaps, with a subsequent risk of flap rupture. When designing the Ti mesh sheet onscreen from the CT scan data, it is necessary to also envision the placement of the mucosal incision and sutures. If the Ti mesh sheet is too large, there is a risk that the mucosal flap may rupture at the weak points of the mucosa, such as the suture line; therefore, if the mucosal flap is expected to be thin, it is necessary to design the implant to ensure that the mucosal suture line does not sit directly above the Ti mesh sheet. Furthermore, in conventional surgery, cutting, trimming, and bending of the conventional Ti mesh sheet can result in sharp edges, which may cause mucosal rupture. With our SLM Ti mesh sheet method, there was no need for intraoperative manipulation of the Ti mesh sheet; thus, the SLM Ti mesh sheet may be associated with less risk of mucosal rupture than is conventional Ti mesh sheet.

Recently, computer - assisted technologies (computer-aided design / computer - aided manufacturing) using CT images have made remarkable advances and have also contributed to developments in the fields of maxillofacial

reconstruction¹⁸ and dental implants. With the three-dimensional model construction device EOSINT M 270, the pure titanium powder layer (which is paved on the molding table) is sintered and melted using a laser beam. A pure titanium structure of any complex shape can be molded by adding a 30- μm layer in the direction of the vertical axis each time a layer is sintered and melted throughout the additive manufacturing process. However, a slight dimensional error is likely to occur between the original data in the computer and the Ti mesh sheet generated using layered manufacturing. According to a report published by Otawa et al., dimension errors found in the vertical direction (namely in the lamination direction) are believed to be greater than those found in the horizontal axis direction, but the average error is 139 μm , and poses no issue when used for bone augmentation.

Customarily, the Ti mesh sheet used for bone augmentation in dental implants is removed after the bone augmentation is complete. However, removal of the mesh may create problems, such as reduction in gingival volume, removal of bone when a large amount of bone has been added to the Ti mesh sheet, and/or creation of a larger incision to remove the Ti mesh sheet. Considering the high degree of Ti biocompatibility, Ti mesh sheet could also be an option for deployment as a type of artificial bone embedded in the body after it has been used for space creation in bone regeneration. Given that Ti artificial knee joints and Ti brain artery clips are embedded in the body, expanding the use of Ti mesh from supplementary use as a bone defect space creation sheet to free-form artificial bone material embedded in the body is a logical next step. In a number of cases, Ti mesh sheet has been left embedded in the body (with consent from the patient) and has served to retain the aesthetic appearance of the gingiva surrounding the front teeth. We are, therefore, investigating the application of laminate-molded

RECONSTRUCTION OF THE ALVEOLAR BONE USING BONE AUGMENTATION WITH SELECTIVE LASER MELTING TITANIUM MESH SHEET

Ti mesh sheet as embedded artificial bone in a wide range of mandibular and maxillary bone defects. Bone regeneration from residual bone can be expected when there is a comparatively small area of bone loss. However, when there is significant bone loss, concurrent use of artificial or autologous bone is essential. Ti has a high degree of biological affinity and, although bone synostosis occurs when it is in direct contact with bone, adequate bone formation cannot be expected if there is a gap between the Ti and the bone. Various treatments have been proposed and applied in clinical practice to increase the bone-binding capability of the Ti surface when in direct contact with bone.

THE STUDY OF DEMAGNETIZATION EFFECT ON C-TYPE ANISOTROPIC HARD FERRITE MAGNET SIMULATION

Chih-Liang Chien, C.S. Liu, Kun-Keng Liu, Chi-Ping Lee and Chun-Chung Shao

Superrite Electronics Co., Ltd, Si-Tung Rd., San Hsia Dist., New Taipei City, Taiwan, R.O.C

Abstract : C-type anisotropic hard ferrite magnet (Hereinafter referred to briefly as C-type magnet) is widely used in motor industrial because of its low cost, high safety and high thermal stability. However, if the magnet is demagnetized in the motor, it would cause fatal effect on the performance of the motor. Therefore, how to avoid the demagnetization of the C-type magnet in the motor becomes an important issue. Demagnetization is related with magnet distinctive characteristics, motor operation temperature, and magnetic field generated by motor coil. Magnet characteristics such as shape, orientation, hysteresis curve are the factors which would affect demagnetization. This study focused on the distinctive characteristics of C-type magnet.

Due to complex shape and special orientation, demagnetization of C-type magnet is different from simple geometry magnet. There are some graphing methods that can evaluate whether a magnet would be demagnetized in certain condition. But it can only deal with simple geometry and parallel orientation. C-type magnet can't be specifically analyzed. This study used magnetic circuit simulation software (JMAG) based on finite element analysis methods and the Maxwell's equation. It can identify the demagnetization factors of a C-type magnet, calculate magnetic field and operating point of every element to simulate the demagnetization process. A demagnetization experiment was conducted to prove the simulation results. And a good agreement was found between the simulation and experiment.

In this study, we found the key factors to prevent a C-type magnet from demagnetization and a better method to predict magnetic field changed after demagnetization.

Methodology

The magnet used in this study was a C-type structure with the dimension on the width and height are both 16.6 mm, outer and inner diameter are 11.3 mm and 7.75mm respectively. The maximum and minimum thickness of the C-type magnet are 3.55 mm and 5.23 mm respectively (Fig.1.), and the orientation was radial. The temperature of this study was a constant at 20°C. The material hysteresis curve was referred to a Japanese hard ferrite company. The Br and iHc of this hysteresis curve are 0.395 Tesla and 239 kA/m respectively. A reverse magnetic field was generated by a coil with the dimension on the height 125 mm, outer and inner diameter are 150 mm and 80 mm respectively (Fig.2.). The C-type magnet was positioned in the middle of the coil by a fixture. When the power was applied, different reverse magnetic field 80 kA/m (about 1 kOe), 120 kA/m (about 1.5 kOe), 160 kA/m (about 2 kOe) would be generated respectively.

The C-type magnet would be demagnetized each time when the reverse magnetic field was generated (Fig.3.).



Fig. 1

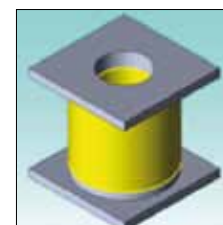


Fig. 2

THE STUDY OF DEMAGNETIZATION EFFECT ON C-TYPE ANISOTROPIC HARD FERRITE MAGNET SIMULATION

Three current pulses as showed in Fig. 4. would generated reverse magnetic field as follow:

1. 80 kA/m
2. 120 kA/m
3. 160 kA/m

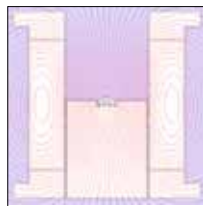


Fig. 3

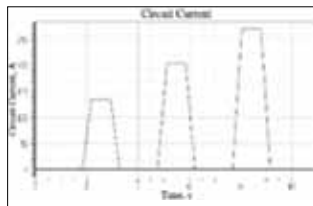
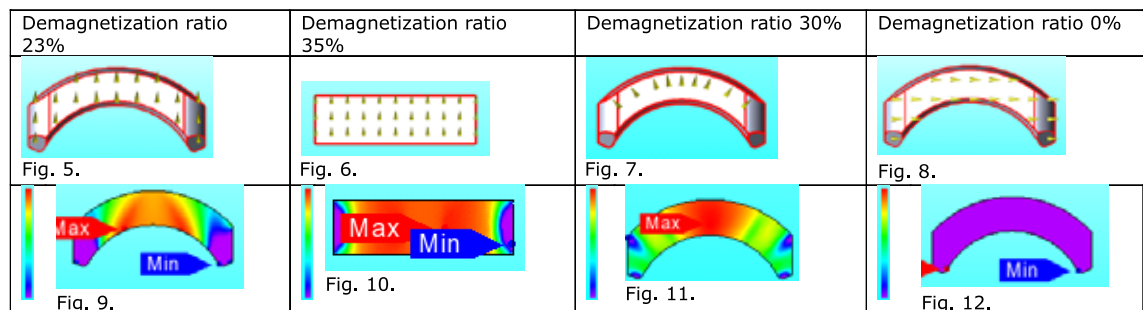


Fig. 4

Results and Discussions

Condition 1. Set orientation as a constant (vertical): After demagnetized by 160 kA/m, the average demagnetization ratio of C-type magnet and the square magnet 16.6*16.6*5.23 mm are 23% (Fig.5&9.) and 35% (Fig.6&10.) respectively. It indicated a C-type shape was more difficult to be demagnetized than a square shape.

Condition 2. Set magnet geometry as a constant: After demagnetized by 160 kA/m, the average demagnetization ratio of vertical, radial and parallel orientation are 23%, 30% (Fig.7&11.) and 0% (Fig.8&12.) respectively. It indicated parallel and vertical orientation was more difficult to be demagnetized than the radial.



Select a left point from inner radius			Select a left point from outer radius				
Fig. 13.			Fig. 14.				
Original value	B (T)	Demagnetization ratio	Table 1.	Original value	B (T)	Demagnetization ratio	Table 2.
After 160 kA/m	0.09 0	15%		After 160 kA/m	0.11 3	23%	
Select a middle point from inner radius			Select a middle point from outer radius				
Fig. 15.			Fig. 16.				
Original value	B (T)	Demagnetization ratio	Table 3.	Original value	B (T)	Demagnetization ratio	Table 4.
After 160 kA/m	0.08 8	60%		After 160 kA/m	0.03 5	71%	

THE STUDY OF DEMAGNETIZATION EFFECT ON C-TYPE ANISOTROPIC HARD FERRITE MAGNET SIMULATION

Condition 3. After compared the demagnetization of different shape and orientation. The following were the comparison between different part of a magnet. The typical orientation of C-type magnet is radial. So set C-type shape and orientation(radial) as constants, after demagnetized by 160 kA/m, the demagnetization ratio on the middle and left point of inner diameter are 60% and 15% respectively. After demagnetized by 160 kA/m, the demagnetization ratio on the middle and left point of outer diameter are 71% and 23% respectively. It indicated that the side portion was more difficult to be demagnetized than middle portion. And the middle portion of inner diameter was more difficult to be demagnetized than the outer.

The results of the study indicated

In condition 1. When orientation was a constant, the C-type magnet was more difficult to be demagnetized than the square magnet. The reason was that the flux density vector of the C-type magnet became radial due to the curvature of the magnet (Fig. 18.), thus changing the vertical vector of reverse magnetic field (Fig. 19.). Comparing to a square magnet (Fig. 20&21.), there was less reverse magnetic field can be applied on both sides of the magnet.

In condition 2. Set the shape as a constant, the horizontal orientation was more difficult to be demagnetized than the radial (see Fig. 17.). The reason was that the C-type magnet has hexagonal crystal lattice. In

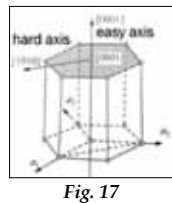
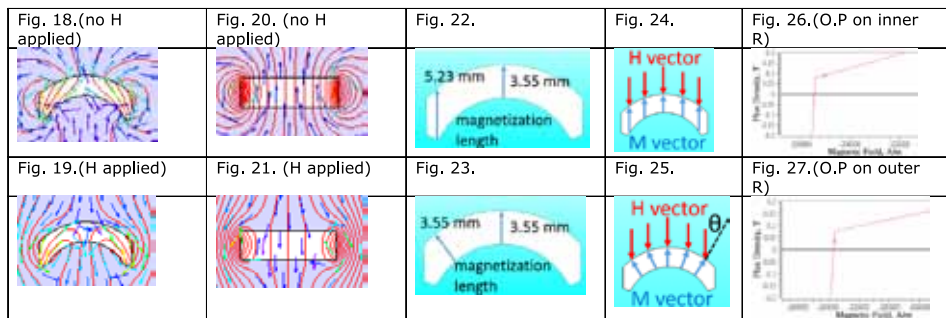


Fig. 17

this case the moments were aligned along the unique axis 0001 which was the easy direction to magnetize while the 1010 axis in the base plane was the hard axis. The bigger angle between easy axis and reverse magnetic field, the harder a C-type magnet would be demagnetized.

In condition 3. Set shape as a constant, the vertical orientation was more difficult to be demagnetized than the radial orientation. The reason was that the C-type magnets were much thicker on both sides than the middle. So magnetization length of vertical orientation was greater than the radial (Fig. 22&23.). That's why vertical orientation magnet was more difficult to be magnetized. In this case, although the angle of easy axis and reverse magnetic field in radial orientation magnet was greater than the vertical one. But the factor of magnetization length played a more important role than the angle factor (Fig. 24&25.).

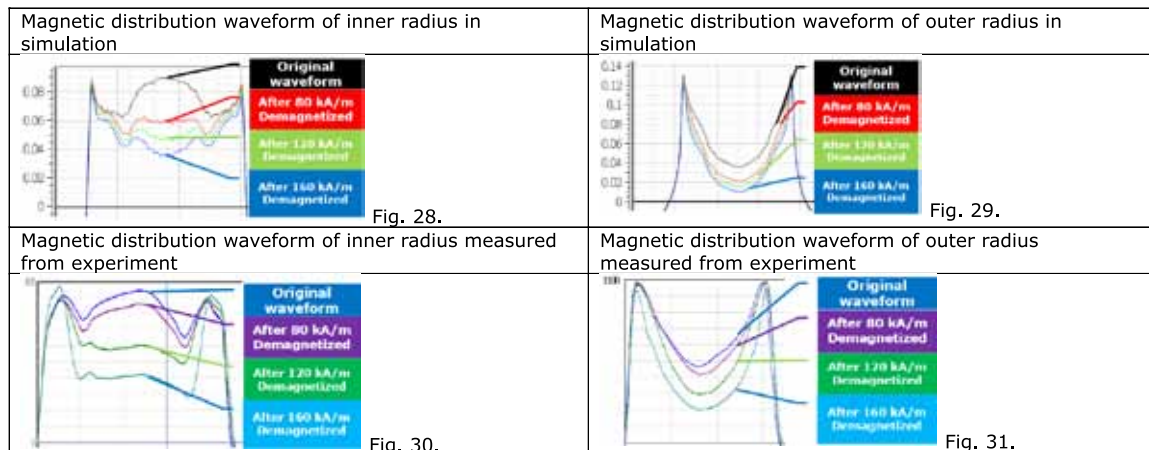
In condition 4. On the same radial orientation magnet, both sides were more difficult to be demagnetized than the middle. The reason was that, as mentioned in condition 1, the flux vector of the C-type magnet changed the vertical vector of reverse magnetic field so the reverse magnetic field on both sides were smaller than the middle. As regard to the point on inner diameter was more difficult to be demagnetized than the outer. The reason was that the operating point (O.P) of the inner radius was still above the knee point (Fig. 26.), but the operating point of the outer radius exceeded the knee point(Fig.27.). As long as the operating point exceeded the knee point, the magnet was very likely to be demagnetized.



THE STUDY OF DEMAGNETIZATION EFFECT ON C-TYPE ANISOTROPIC HARD FERRITE MAGNET SIMULATION

After a C-type magnet was demagnetized by reverse magnetic field from 80 kA/m to 160 kA/m. The middle part would be severely demagnetized. According to the magnetic distribution chart, it was seen that the waveform collapsed from the middle and became an

M-wave. Fig. 28. & 29. were the magnetic distribution of inner and outer radius by simulation and Fig. 30. & 31. were magnetic distribution by experiment. *A good agreement was found with simulation and experiment.*



The demagnetization factors affecting the C-type anisotropy hard ferrite magnet were described as follow: 1. Flux density vector.2. The angle of the easy magnetization axis and reverse magnetic field.3. The magnetization length.4. The operating point. These factors were clearly defined in this study. The effect of these factors on the demagnetization results have been calculated accurately in this simulation. In the past, it was hard to analyze the demagnetization effect on the C-type anisotropic hard ferrite magnet. Industrial usually relies on an approximate evaluation and empirical formula to confirm whether the magnet would be demagnetized. The finite element analysis methods can be used to calculate the demagnetization of each point of the magnet. Parameter of each factors can be adjusted by changing the shape or orientation of the magnet to reduce demagnetization in simulation. It can be used to optimize a C-type magnet.

References:

1. David Jiles , *Introduction to magnetism and magnetic materials*, (1991), CHAPMAN AND HALL
2. Tsung-Shune Chin, *Handbook of magnetic technologies eng*, (2002), Taiwan Association for Magnetic Technology
3. Jyh-Shen Tsay & Y.D.Yao., *Magnetic technology and application*, (2017),National Taiwan Normal University Press
4. JSOL Corporation, *120 - Thermal Demagnetization Analysis of an SPM Motor*, (2009),JSOL Corporation
5. Zimin.Wang, *Hard ferrite magnet production technology*, (2015),Science Press
6. LIAO, WEN-PO, *Introduction to NdFeB Magnet characteristics and application*, (2018)